THE UNIVERSITY OF HULL

Finite Element Analysis of Idealised Cardiovascular Stents: Understanding the
Influence of Artery Material Models on Stent Stress Distribution

being a Thesis submitted for the Degree of

Master of Science

in the University of Hull

by

Frances Pauline O'Keeffe

September 2020

Abstract

Stent fracture (SF) is thought to be a major contributor to in-stent restenosis and other adverse clinical events. It has been linked to angulated vessels and bifurcations, where there is often a hinge-motion movement throughout the cardiac cycle. Finite element (FE) analysis of stented arteries can be utilised to assess stent stresses and predict the likelihood of SF.

An idealised tubular stent model was initially created and validated for use as a design-independent representation of stent devices. The stent model was idealised to a cylindrical tube to eliminate the device artifacts and ensure the resulting stent stress analysis was not distorted by highly localised areas of higher stress. The idealised model was based on the 3-point-bend test of a cardiovascular stent, and the FE model created to represent the mechanical behaviour of the device.

Human arteries have previously been represented using a variety of mathematical models ranging from simple linear isotropic models to more complex hyperelastic models. As there has been little comparative work to qualify the necessity of using the more complex constitutive models for analysis of stresses in the stent, this study employed a variety of mathematical models used to represent human arteries to allow direct comparison of the sensitivity of model variation. The idealised stent model was used to represent an angulated stented vessel undergoing hinge-motion bending. Six different artery models from the literature were used to define the artery in the FE model and the resulting stent stresses were assessed.

The results of the sensitivity study were varied and indicated little sensitivity to the artery model in terms of the stress distribution pattens, however the maximum stress values were more diverse. Overall, the likely location of SF was determined to be on the

inside of the hinge-point of the stented bifurcation lesion. The model was determined

to be useful as a comparative model to assess different stents devices and materials for

those most likely to fracture.

Contents

Table of Figures

Table of Tables

1 Introduction

Coronary heart disease (CHD) is responsible for about 20% of all deaths in men and about 17% of deaths in women (NICOR, 2013). It is characterised by an accumulation of lipid deposits in arterial lumens, resulting in the narrowing of blood vessels thus restricting the blood supply to the heart. Left untreated, CHD may result in myocardial infarction or ischaemic stroke. Percutaneous coronary intervention (PCI) is increasingly being used to treat the stenosed vessels. This involves the deployment of a balloon or stent with the aim of increasing the structural integrity of the lumen.

Success of PCI is difficult to evaluate due to the nature of the treatment and an intervention failure is often only observed post-mortem. The major causes of PCI failure include vascular injury during treatment and stent fracture (SF) both during deployment and throughout the lifetime of the stent. Both have been linked to restenosis and stent thrombosis. SF may also negate the effect of increased lumen structural integrity. The success of PCI therefore, is strongly linked to arterial injury at the PCI site.

In order to quantify the true success of PCI, therefore, finite element (FE) analysis can be carried out to evaluate the implantation technique and the mechanical response of both the stent and vessel after deployment. Stent-artery interactions have been investigated extensively, although almost exclusively focusing on the level of vascular injury incurred during deployment (Liang et al., 2005; Hajiali et al., 2014; Shang, 2014). In short, much of the published work involving stent-artery interactions is thorough in its approach to calculating vascular stress, but lacking in consideration to the stent itself. The stresses undergone by the stent and how this might relate to SF and the potential for PCI failure later in its lifetime is little understood.

As many as 15-20% of PCIs are carried out at bifurcation sites (Waksman and Bonello, 2008). Such interventions pose more of a challenge during the procedure, but also during the lifetime of the stent. The bending stresses placed on the stent throughout each cardiac cycle for the lifetime of the stent may cause fatigue and increase the likelihood of SF.

The aim of this project is to investigate the effects artery properties on stent stresses. A combination of mechanical testing and FE analysis is used to achieve this.

The background information relevant to the study is documented in Chapter 2 and a review of relevant published work has been carried out in Chapter3. Aims and objectives are outlined in chapter 4. The development of an idealised, design independent stent model for use in stress analysis simulations is discussed in chapter 5. The reasons for the use of an idealised model in chapter 6 is discussed, and the model construction and is described. The validation process is described and the model's intended use in subsequent chapters is briefly explained. Chapter 6 covers a study of the sensitivity of the stent in the idealised model to the way in which the arterial tissue is modelled in FE. The development of the model based on the results from chapter 5 is explained and a variety of material models are then studied for sensitivity to the stresses in the stent. Chapters 7, 8 and 9 are cover the limitations of this study, conclusions and future work respectively and the references and appendices can be found at the end of the report.

2 Background

2.1 Introduction

This section provides a summary of the background information to provide context for this study. It briefly comprises the anatomy of the cardiovascular system, the development of atherosclerosis and its treatment and an overview of cardiovascular stents.

2.2 The Cardiovascular System

The cardiovascular system encompasses the heart and a complex network of blood vessels, both of which are vital in the transportation and dispersion of blood throughout the body. The myocardium behaves as a mechanical pump, facilitating the distribution of blood throughout the multifaceted closed network of arteries and veins, which carry the blood away from, and toward the heart respectively. Figure 2-1 shows the vascular anatomy in the heart. Capillaries are the smallest of the blood vessels, which connect the two larger types of conduits and allow the exchange of oxygen, nutrients and waste products (Drake et al., 2010).

2.2.1 Coronary Arteries

Artery walls are composed of three layers; the tunica intima, tunica media and tunica adventitia, and are defined by the internal elastic lamina and external elastic lamina that separate them. The intima is the innermost section and consists of a layer of endothelial cells on the luminal surface, embedded in an extracellular matrix (Greindling and Alexander, 1998). The intima can be further broken down into the proteoglycan layer, in which is an abundance of proteoglycans, smooth muscle cells and macrophages (Dean and Kelly, 2000), and the musculoelastic layer, which is composed of elastic fibres and copious smooth muscle cells. The intima does not play an important role in blood vessel
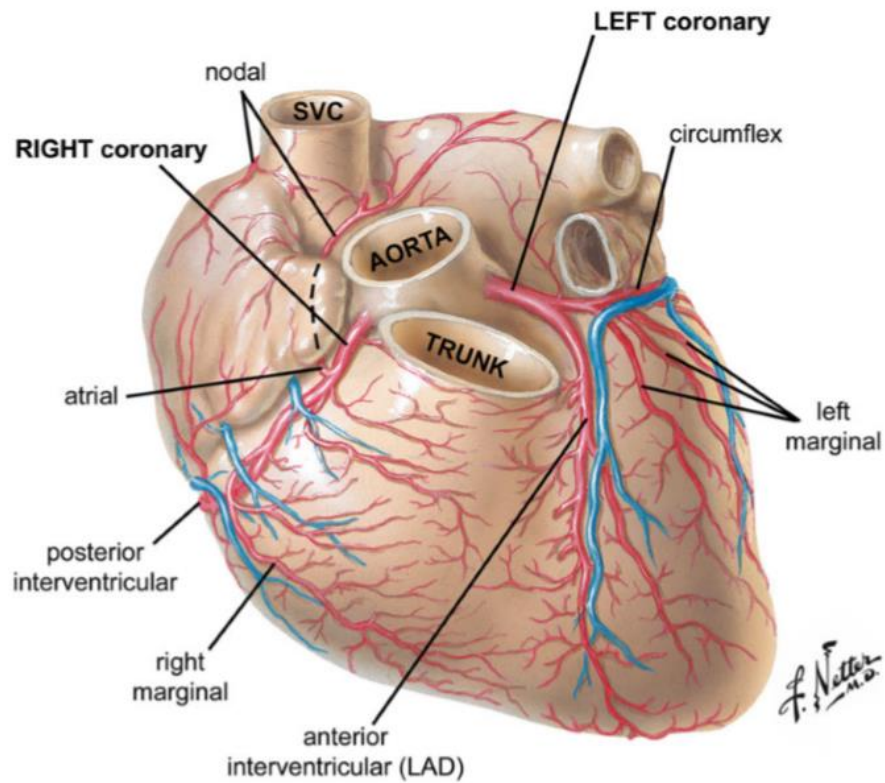
Figure 2-1: Coronary vascular anatomy (Weinhaus, 2015)

mechanics but is critical in the haemodynamics of the blood. As the endothelial cells are in direct contact with the blood, they are subjected to great variations in stress and strain as the blood is pulsated through the vessel network.

The tunica media represents the majority of the blood vessel wall. It is the muscular section of vessel walls, thus is responsible for maintaining its structural integrity and offering the necessary mechanical strength. The section is made up of layers of smooth muscle cells, elastic tissue and collagen fibrils (Canfield and Dobrin, 2006; Dean and Kelly, 2000).

The outermost section of the vessel wall is the adventitia, which consists of loose connective tissue designed to anchor itself to the surrounding organs.

2.3 Atherosclerosis

Atherosclerosis is the most common form of arteriosclerosis. Atherosclerotic lesions are characterised as an accumulation of lipid tissue and calcium deposits in the arterial lumen that reduce the size of the blood vessel, thus reducing the ease with which the blood flows through the body. As can be seen in Figure 2-2, atherosclerotic lesions begin with fatty streaks that build up over time to form the calcified plaque that may lead to plaque rupture.
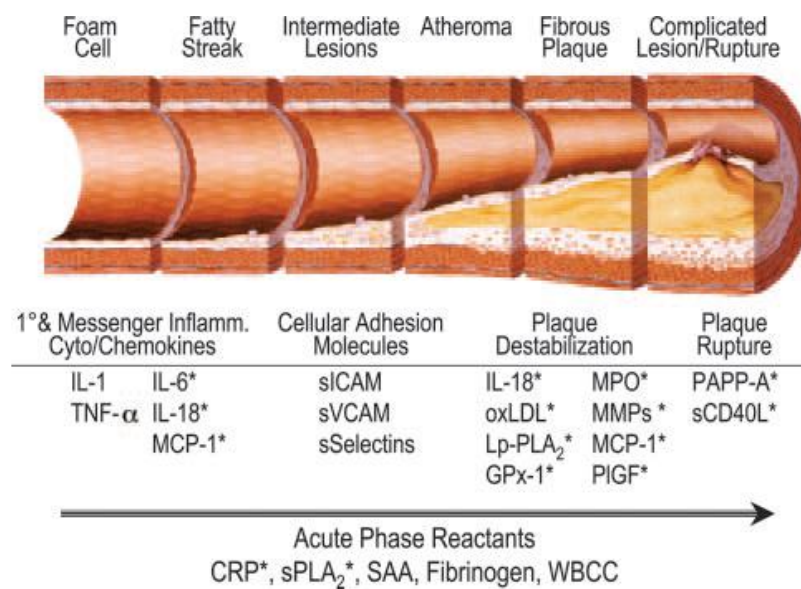
Figure 2-2: Progression of atherosclerosis (Koenig and Khuseyinova, 2006)

Progressive stenosis by calcified plaque can be perilous. Narrowing of a coronary artery to the point of compete obstruction will arrest blood flow. Also, plaque rupture may initiate thrombus formation. Both of these outcomes may result in complete or incomplete obstruction of the blood supply to the heart and may result in myocardial infarction.

Atherosclerotic lesions may develop at any location in the body, however when located in the coronary arteries they can lead to coronary heart disease (CHD), for which the rates of mortality are very high (Table 2-1).

Table 2-1: CHD mortality figures 2015-2018 (British Heart Foundation, 2020)

	Total number of deaths caused by CHD in the UK by year (% of total deaths by all causes in parentheses)			
	2015	**2016**	**2017**	**2018**
Men	41,959	40,297	40,974	40,395
Women	27,826	25,779	25,367	23,737
Total	69,785 (11.6%)	66,076 (11.1%)	66,341 (10.9%)	64,132 (10.4%)

2.3.1 Treatment

There are two interventional procedures that can be used to treat the diseased lesions: percutaneous coronary intervention (PCI) or coronary artery bypass graft (CABG). CABG is the more invasive of the two treatment options, whilst PCI is the non-surgical alternative. CABG is a surgical procedure that involves replacing the diseased blood vessel with an unaffected vessel from another part of the body, usually the chest or leg, which allows the blood to bypass the atherosclerotic lesion. Conversely, percutaneous

treatments involve accessing the stenosed artery through a small incision in the groin or arm and re-dilating the vessel with a balloon catheter with or without a stent. PCI is considerably less costly both in monetary and resource terms, but also in terms of recovery time for the patient.

PCI procedures are increasingly being carried out in the treatment of CHD. With the level of surgical risks for the minimally invasive procedure far outperforming that of traditional CABGs, the number of PCIs carried out in the UK in 2013 was 92,589, which corresponds to a rate of 1,444 per million population (pmp) (NICOR, 2013), significantly surpassing the number of CABGs. The number of PCI procedures represents 80% of all intervention for the treatment of CHD, with the remaining 20% of patients being treated with CABG. Clinical outcomes are thought to be positive, however the difficulty associated with accurately quantifying the success of PCI before clinical symptoms recur necessitates the use of computer modelling to reproduce the procedure.

In PCI, a balloon catheter is inserted into the femoral artery or major artery in the arm and, guided by the use of x-ray imaging, fed through the blood vessels to the site of the lesion. Once in place, the balloon is inflated with the aim of opening the artery leaving an unobstructed lumen through which blood can flow freely (Figure 2-3). After initial redilation, a crimped stent is positioned around a second balloon guide wire before inflation. The act of inflating the balloon in the stenosed artery decrimps the stent into its expanded state, plastically deforming the struts thus ensuring that it remains in place as the balloon is deflated and removed (Figure 2-3). As stent designs have progressed, self-expanding stents have also come onto the market. Unlike balloon-expanding stents, such devices are manufactured at full diameter, crimped onto the catheter, and constrained until in the desired location (Duerig and Wholey, 2002).
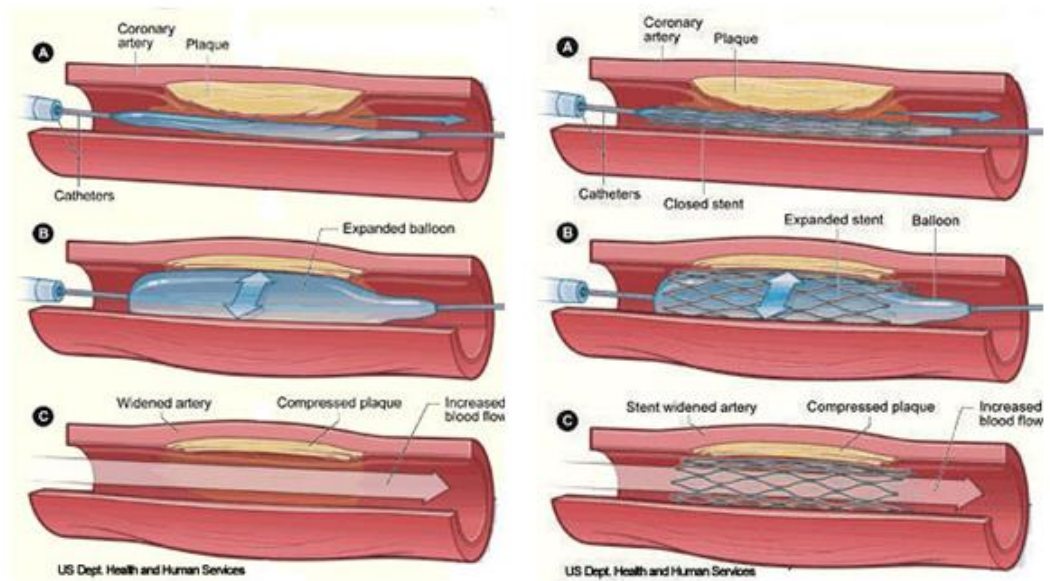
Figure 2-3: Percutaneous coronary intervention; balloon angioplasty (left) and angioplasty with stent (right). (McDougall, 2006)

Stenting is a technique that is now well-established and is used in up to 85% of all PCI procedures (Thierry et al., 2004).

2.4 Stents

A stent is a small, cylindrical wire mesh, which may be deployed into atherosclerosis-affected vascular lumens in order to re-establish the structural integrity of the inner wall of the vessel and ease constriction in the area through which the blood can flow. The aim is to reduce the amount of blockage in the vessel caused by the plaque. As stenting is not a cure for atherosclerosis, restenosis can be a problem. For this reason, drug-eluting stents (DES) are becoming widely available.

2.4.1 Types of Stents

Stents have been classified in many different ways, usually by their clinical use. Stoeckel, et al. (2002), however, proposed a design pyramid with which incorporates the different design and engineering characteristics of stents, as shown in Figure 2-4.

Using the classification method shown in Figure 2-4, the first important factor to note is the material used and whether the stent is designed to be balloon expandable or self-expanding. Once that has been established, the design can be classified by the form of the original material, how it is fabricated, the geometry of the stent and any additions or coatings.
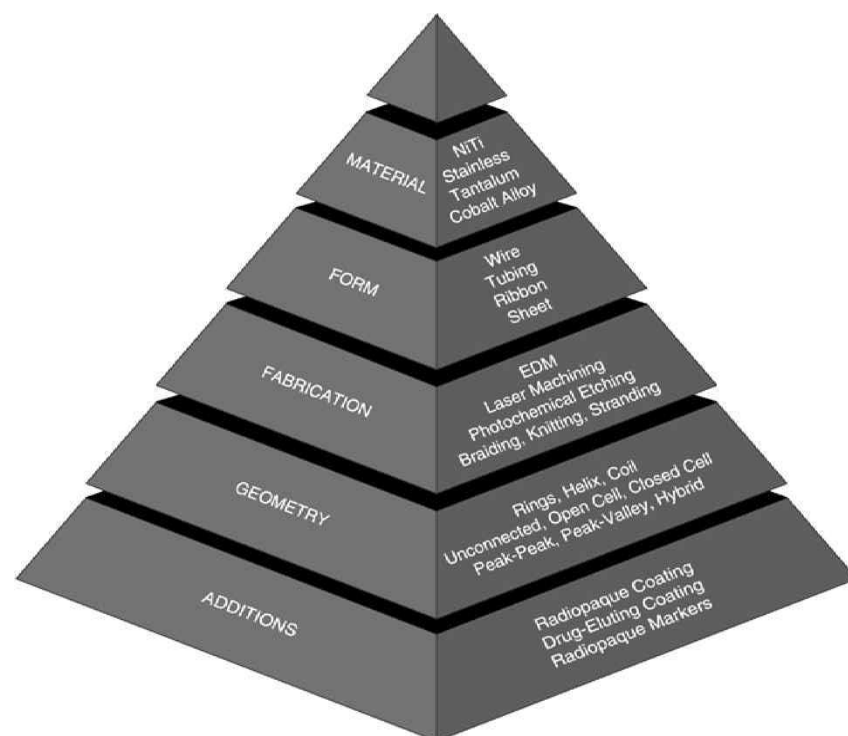
Figure 2-4: Stent design pyramid (Stoeckel, et al., 2002)

2.4.1.1 Materials

Choice of material depends on the material properties and the deployment method for the stent. Stents should be biocompatible, corrosion resistant, flexible, elastic,

radiopaque, and have a uniform radial strength. For this reason, the most commonly used materials for stents are 316L stainless steel, nitinol, tantalum, and cobalt-chromium-based alloys (Thierry et al., 2004).

2.4.1.2 Form

Stents may be fabricated from a flat sheet of material, wire, or tubing. The original form dictates entirely the way in which the device will be fabricated, and there have been a number of studies looking at the material properties of the metals currently in use in their different forms and how this will impact the performance of the final product.

2.4.1.3 Fabrication Method

The fabrication method is dependent on the raw form of the material chosen. Wire can be easily manipulated into stents using various methods including coiling (Figure 2-5) or braiding (Figure 2-6) and then welding where necessary to form a closed-cell structure (Figure 2-7).

Alternatively, in the case of stents fabricated from tubing, as are the vast majority of the devices (Stoeckel et al., 2002), intricate laser cutting is utilised to create the mesh design. Importantly, laser cutting produces a heat-affected zone that must be removed, thus electropolishing is used to treat the surfaces. Devices created from material in its sheet-metal form may be manufactured in the same way and rolled into a cylindrical configuration following cutting.

Figure 2-5: Nitinol ribbon coil stent (Stoeckel et al., 2002)
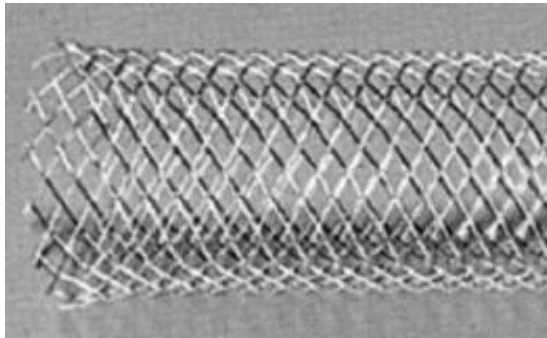
Figure 2-6: Braided cobalt alloy wire stent (Stoeckel et al., 2002)
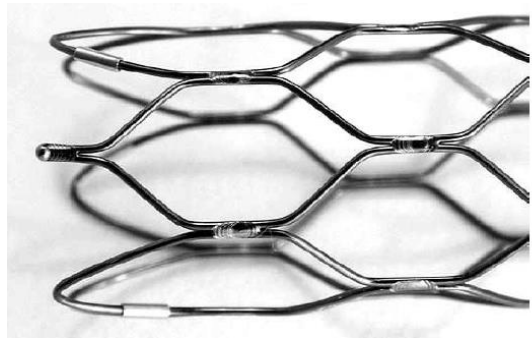
Figure 2-7: Nitinol wire stent, welded to form a closed-cell structure (Stoeckel et al., 2002)

2.4.2 Geometry

2.4.2.1 Coil

The coil design stents (Figure 2-5) are very flexible but have limited expansion potential.

2.4.2.2 Woven

Woven stents include a variety of designs, all of which are created from one or more strands of wire that are knitted or woven together without any need for welding. The strength of such stents is often highly dependent on the axial fixation at its ends and they are usually designed to be self-expanding (Stoeckel et al., 2002).

2.4.2.3 Closed Cell

Closed cell designs describe stents in which all of the inflection points are connected. This may mean that the internal peaks of simple wire stents have been welded together

as in Figure 2-7 or, in the case of tubular laser cut devices, the pattern has been designed to have closed cells. Such stents have a more uniform surface and offer greater structural integrity than open cell designs. Closed cell tubular stents tend to be relatively rigid when compared to other such stents, thus are less suitable for placement in curved vessels or bifurcations.

2.4.2.4 Open Cell

Stents that have a less uniform design and include internal inflection points that are not bridged are called open cell. Such devices are created from wire with internal peak-to-peak or peak-to-valley connections welded intermittently to connect the scaffold, but also to allow the device to have a great deal of flexibility. The open cells, however, sacrifice some of the strength of closed cell designs.

2.4.2.5 Additions

At the bottom of the stent classification pyramid are any coatings that may be added to the bare metal. As stenting became a more popular method than PCI and research into stenting techniques and restenosis became more common, the discovery of the high rate of occurrence of restenosis led to the development of drug-eluting stents (DES). It was intended to coat the bare metal stent (BMS) with a polymer that would disperse over time an immunosuppressant such as everolimus, sirolimus and zotarolimus to prevent the occurrence of restenosis in the lumen. The drug used would act to prevent the growth of the lesion any further, in addition to the structural advantages of the stent. The DES, therefore, were expected to be more effective than BMS.

2.4.3   Complications with Stenting

There are many problems that can arise following a PCI procedure. Restenosis is the major obstacle in the long-term success of stents.

Restenosis is defined as the renarrowing of a blood vessel after treatment to reduce initial blockage. Recurrence of stenosis after treatment by PCI is called in-stent restenosis (ISR) and affects up to a quarter of patients (Gage and Wagner, 2003). This often means that further treatment will be necessary to re-open the vessel. The mechanisms of restenosis are not completely understood, however it is thought that it begins as a response to tissue damage in the vessel, caused by the implantation of the stent (Simard et al., 2014; Gage and Wagner, 2003).

2.5 Bifurcation Stenting

A bifurcation is the division of a blood vessel into two branches. As a result of the differences in blood flow, turbulence and shear stress at such sites, they are commonly affected by atherosclerotic plaque build-up. Due to the prevalence of atherosclerosis, 15% to 20% of all interventional procedures are reported to be at bifurcations (Waksman and Bonello, 2008). Interventions at such divisions present more of a challenge than traditional, straight vessel interventions, thus have a lower procedural success rate and a higher rate of restenosis (Iakovou et al., 2005).

2.5.1 Classification of Bifurcations

Bifurcations have been classified in several different ways according to their plaque burden or angulation. The classification defined by Lefèvre et al. (2000) can be seen in Figure 2-8 and Figure 2-9 below. Although the many classification methods are useful guidelines, it is pointed out by Iakovou et al. (2005) that such categorization is limited as each bifurcation is different and should be approached accordingly.

The most frequently used lesion categorisation is based on the location of the plaque, although the first factor that must be determined is the angulation of the side branch from the main branch. 70° has been labelled the critical angle by Lefèvre et al. (2000),

below which the bifurcation is classed as Y-shaped and above which it is considered T-shaped (Figure 2-8). Location of the plaque is also important when considering stenting techniques. Type 1 lesions are defined as 'true' bifurcation lesions, in which both the main branch and the ostium of the side branch are affected (Figure 2-9). Type 2 lesions involve only the main branch at the site of the bifurcation and not the ostium of the side branch (Figure 2-9).

Type 3 lesions include only the main branch proximal to the bifurcation (Figure 2-9). Type 4 lesions are located at only the ostium of each branch of the bifurcation, whilst type 4A and 4B involve only the ostium of the main branch and side branch respectively (Figure 2-9).
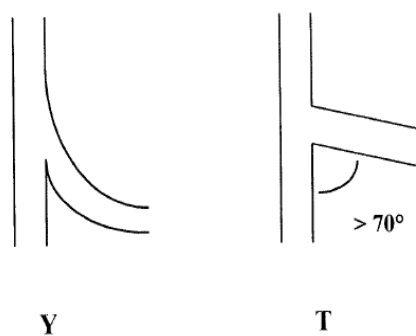
Figure 2-8: Classification of bifurcation lesions according to angulation (Lefèvre et al., 2000)
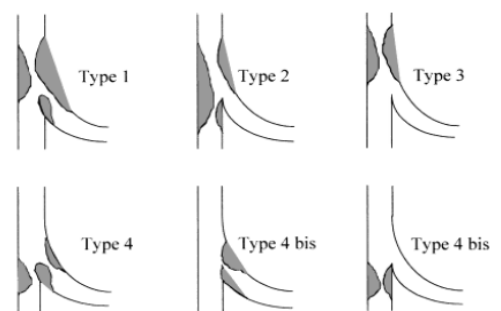
Figure 2-9: Classification of bifurcation lesions according to morphology (Lefèvre et al., 2000)

2.5.2 Bifurcation Stenting Techniques

Several techniques for stenting bifurcations have been developed, some of which use more than one stent. In all stenting techniques, the first decision to be made is whether the vessel requires pre-dilation in either the main branch (MB) or side branch (SB).

The most common approach when treating bifurcations is the one-stent technique, which involves the implantation of just one stent in the MB of the vessel at the site of

the bifurcation lesion. Although there is the possibility of the 'snow-plough' effect – the occlusion of the SB due to plaque shift when stenting the MB at high pressures – there has been little proven advantage to an additional stent deployed in the SB (Pan et al., 1999; Al Suwaidi et al., 2000; Yamashita et al., 2000). Despite this, there are several two-stent techniques available.

The V stenting technique, the method for which is shown in Figure 2-10, involves the dilation of two stents in the two branches of the bifurcation. The V technique consists of the same delivery as the simultaneous kissing stents technique (Figure 2-11), the only difference being the length of extension of the stent into the main branch from the SBs. There is no overlap of stents in the V stenting technique, whilst the kissing stents usually have a 5 mm or more overlap in the MB. This overlap acts as an obstruction to the blood flow, however it does provide access to both branches.

The crush technique (Figure 2-14) involves placing two stents in the MB and SB, and deploying that in the SB first. The stent in the MB is not deployed until the balloon and wire of the first are removed, at which point it is expanded, crushing the protruding mesh into the vessel wall. It is necessary to re-dilate both stents after initial deployment open the obstructed side branch. This technique offers excellent coverage of the ostium of the side branch and immediate patency of both branches, however it is a laborious process due to the need to re-expand both stents.

The T-stenting technique consists of deploying an initial stent in the ostium of the SB, before then dilating a stent into the MB. This method requires both vessel branches to be dilated prior to stenting. The T-stenting technique may lead to incomplete coverage of the ostium of the SB (Iakovou et al., 2005), but is less laborious than the crush technique (Figure 2-15).

The culottes technique (Figure 2-12) uses two stents and lead to full coverage of the bifurcation lesion. After dilation of both branches, one stent is deployed into the main branch. Another balloon in then inflated in the SB, crossing through the stent in the MB. This leaves behind a larger hole at the ostium of the SB. A second stent is then deployed through the MB, providing a proximal overlap, and into the SB. It is necessary to then re-inflate both branches. Such a technique is advantageous as it is suitable for all angles of bifurcations, and offers very good coverage of the SB ostium (Iakovou et al., 2005). Similarly to the crush technique, however, the culottes is very time-consuming.

The Y technique involves initial pre-dilation of both branches, before deployment of two stents in the ostia of each branch. A third stent can then be positioned up to the branching, and then dilated in the MB (Figure 2-13). This technique is not ideal as it does not offer full coverage of the ostium, but is necessary when unobstructed access to both branches is required.

Step 1:
Both branches are wired and dilated.

Step 2:
a) Two parallel stents are positioned covering both branches.
b) The stents are inflated alternately.

Step 3:
Final kissing balloon inflation using the same pressure for both balloons.

Step 1:
Both branches are wired and dilated.

Step 2:
a) Position two parallel stents covering both branches and extending into the MB.
b) Inflate the first and then the second stent.

Step 3:
Cross Section
Final kissing balloon inflation using same pressure for both balloons.

Figure 2-10: V stenting technique (Iakovou et al., 2005)
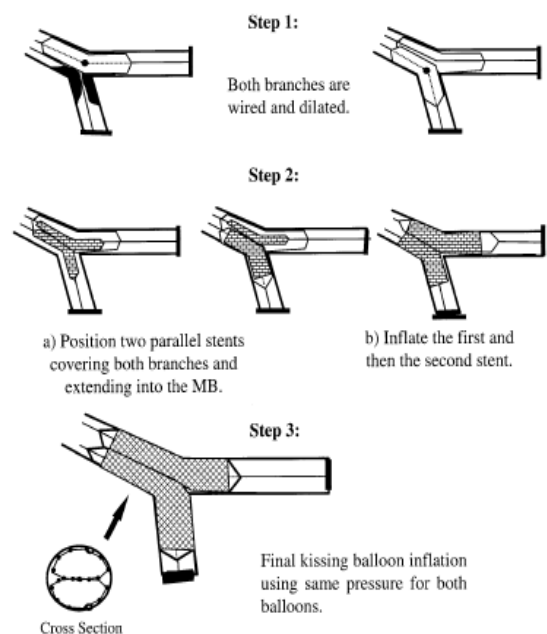
Figure 2-11: Simultaneous kissing stenting technique (Iakovou et al., 2005)
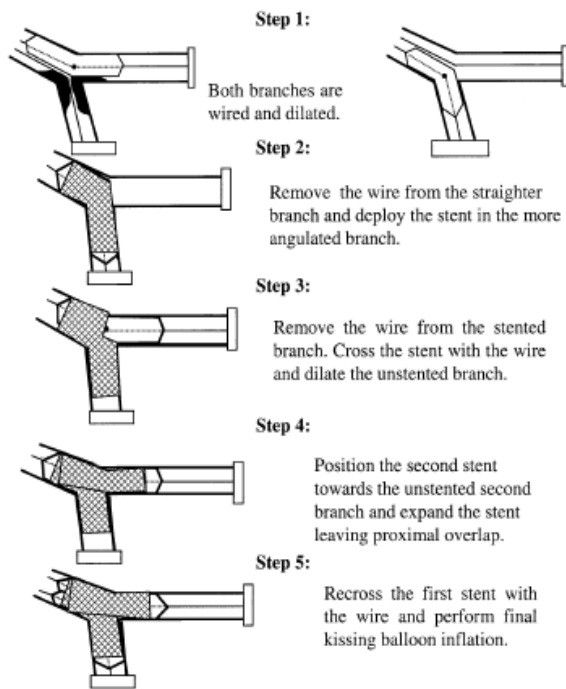
Figure 2-12: The culottes stenting technique (Iakovou et al., 2005)
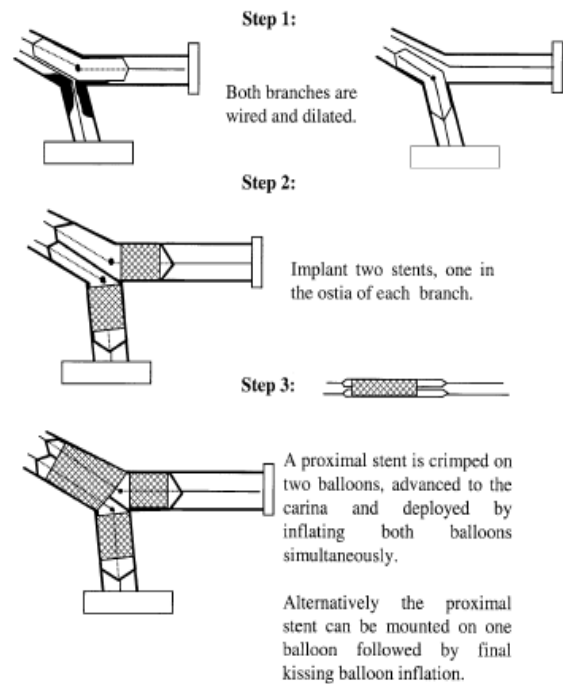
Figure 2-13: The Y stenting technique (Iakovou et al., 2005
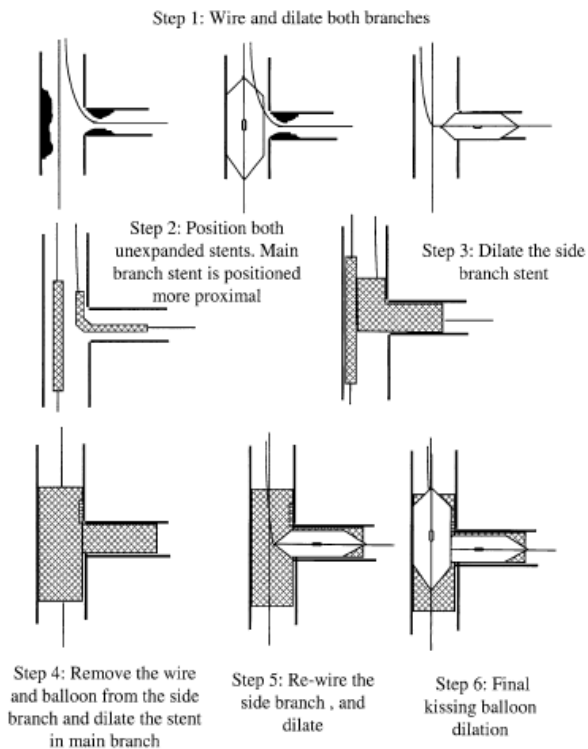
Figure 2-14: The crush technique (Iakovou et al., 2005)
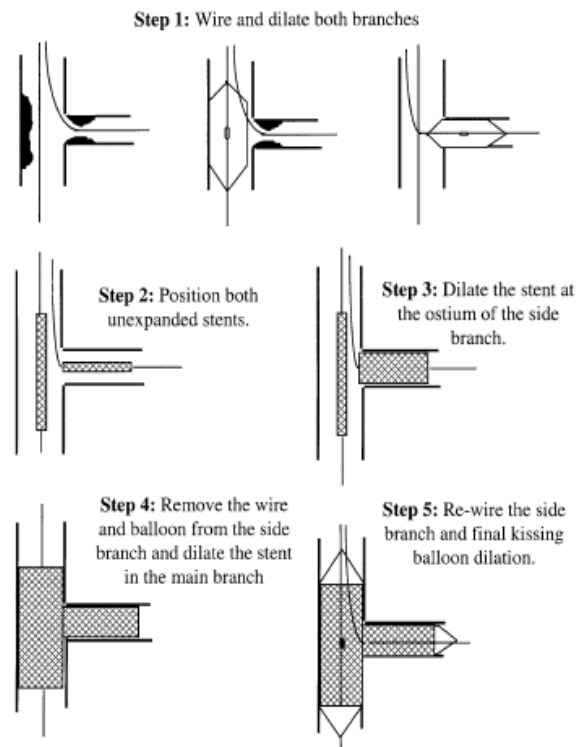
Figure 2-15: The T-stenting technique (Iakovou et al., 2005)

3 Literature Review

3.1 Introduction

This section covers a thorough review of available literature on the subjects of SF, atherosclerotic plaque and the experimental and computational analysis methods for investigating the phenomena.

3.2 Stent Fracture

3.2.1 Classification of Stent Fracture

SFs can be classified in a variety of ways including the number of stent struts affected and the type of displacement (if any). Fractures can range from consisting of a single strut fracture to multiple strut fractures resulting in complete disconnection of sections of the stent. Several attempts have been made in the literature to categorize such fractures (Table 3-1).

3.2.2 Prevalence of Stent Fracture

SF is not always clinically apparent; thus, the true prevalence is not known. Diagnosis requires the use of coronary angiography, fluoroscopy or intravascular ultrasound (IVUS). As the SF is often asymptomatic, the number of reported incidents may be significantly influenced by the percentage of patients who undergo routine follow-up procedures, and often goes unnoticed in patients without clinical symptoms. In addition, the variability in the reported number of occurrences are affected by the differences in definition between studies.

Many studies make a distinction between the type of SF occurring. The classifications of SF shown in Table 3-1 are all very similar, however whilst it is also common to consider any fracture in the stent to fall under the category of SF, some studies discriminate

between single-strut fractures and SF (Popma et al., 2009; Shaikh et al., 2008). This inconsistency means that the actual number SF occurrences may in fact vary significantly from that which has been reported, depending on the preferred definition. Furthermore, this discrepancy will also affect the reported prevalence of SF.

There have been a number of studies carried out that investigated SF *in vivo* (Sianos et al., 2004; Scheinert et al., 2005; Kang et al., 2007, 2009; Lee, M.S. et al., 2007; Pelton et al., 2008; Higashiura et al., 2009; Lee et al., 2009; Nakazawa et al., 2009; Manola et al., 2010; Daneault et al., 2014). The earliest of such fractures to be reported occurred immediately after implantation (Lee et al., 2015), whilst many reported incidents have occurred after several years (Lousinha et al., 2011; Khanna et al., 2012).

The incidence of fracture has been shown to vary significantly, ranging from 1.5% (Lee et al., 2009) after DES implantation at a follow-up coronary angiography, to the considerably dissimilar rate of incidence of 29% of the 177 lesions seen by Nakazawa et al. (2009) in a study aimed at discovering the true occurrence of SF in DES. This study, however, was cadaveric hence less reliant on *in vivo* detection techniques. SF appears to be even more prevalent in self-expanding Nitinol stents, with occurrences of up to 50% after one year (Pelton et al., 2008). The incidence of SF had also been shown to be more prominent in complicated lesions such as bifurcations and those with severe levels of tortuosity, angulation and calcification (Kan et al., 2016).

Table 3-1: Definitions of different classification methods of stent fracture

Classification Type	Popma et al. (2009), Doi et al. (2009)	Scheinert et al. (2005), Lee et al. (2007)	Allie et al.(2004, cited by Popma et al., 2009)	Rocha-Singh et al. (2007)	Nakazawa et al. (2009)
1	Single-strut fracture	Minor (single strut fracture)	Single-strut fracture only	Single-strut fracture	Single-strut fracture
2	Incomplete transverse stent fracture	Moderate (fracture of >1 strut)	Multiple single-stent fractures occurring at different sites	Multiple single-strut fractures	2 or more strut fractures without deformation
3	Complete transverse stent fracture without displacement	Severe (Complete separation of strut segments)	Multiple single-stent fractures resulting in complete transverse linear fracture but without stent displacement	Complete transverse stent fracture with preserved alignment	2 or more strut fractures with deformation
4	Complete transverse stent fracture with displacement of 2 stent fragments		Complete transverse linear fracture with stent displacement	Complete transverse stent fracture with mal-alignment	Multiple strut fractures with acquired transection but without gap
5				Complete stent fracture in a trans-axial spiral configuration	Multiple strut fractures with acquired transection with gap in the stent body

Two cases of SF were reported by Lee et al. (2015), both involving zotarolimus-eluting stents (ZES). In the first, a 62 year old male patient had undergone stent implantation in the right coronary artery (RCA). A follow-up angiogram six hours after the procedure revealed a complete linear transverse fracture of the stent. The second case involved a long lesion in a 75 year old male, which required two overlapping stents to be inserted. During the angiography at the end of the procedure, fracture was found near the overlap of one of the stents.

Lee et al. (2007) observed 2728 patients who underwent drug-eluting stent implantation. Of those, fractures were reported in 10 patients (0.4%), none of which were detectable on implantation. The median time before fracture was detected was 226 days. Analysis revealed that 4 patients had excessive tortuosity, and 5 cases involved overlapping stents.

Another study by Scheinert et al. (2005) on the prevalence of SFs after femoropopliteal stenting found fractures in 24.5% of the 261 implanted stents. 48.4% of the fractured stents were classified as minor, 26.6% were classified as moderate and 25% were classified as severe (Table 3-1). Higashiura et al. (2009) reported a 3.6% rate of incidence of SF following iliac artery stenting of 305 deployed stents. These results, however, came from two different types of self-expanding stents (elgiloy, n=83 and nitinol, n=222). All of the 11 fractured stents were nitinol; giving an incidence rate of 5% for the nitinol stents and a 0% rate for the elgiloy. This may be an indication of the impact that the material choice has on the fracture prevalence. Furthermore, the SFs were classified the same way as in the study by Rocha-Singh et al. (2007) (as shown in Table 3-1) and the majority of the fractured stents were categorized as type 3. This, and the fact that Scheinert et al. (2005) found that more than half of fractures in their study were

classified as moderate and severe, implies that the probability of obtaining more severe SFs increases once the first strut is fractured.

3.2.3 Clinical Relevance of Stent Fracture

Whilst the prevalence of SF appears to be clinically relevant, even more important is the impact that the phenomena are having on patients. In the reports of fractured stents, Cypher stents (Cordis Corporation, Florida, USA) appeared to be commonly fractured devices when compared to Taxus devices (Boston Scientific Corporation, Massachusetts, USA) (Table 3-2). As can be seen by the number of reports of SF, it is a significant problem and may be a contributing factor in restenosis and stent thrombosis (Alexopoulos et al., 2011).

In a case study presented by Kang et al. (2007, 2009) a patient underwent four sirolimus-eluting stents (SES) in four locations with calcified stenoses. At the follow-up angiogram, there was no significant ISR but multiple SFs were observed in two of the previously implanted stents. Two months after the follow-up angiogram the patient suffered sudden cardiac death, the cause of which is uncertain, however it was speculated that it may have been due to stent thrombosis.

A further study reported by Kuramitsu et al. (2012) oversaw the implantation of everolimus-eluting stents (EES) in 1035 patients with 1339 lesions. At the follow-up angiogram 6 to 9 months after the procedure, SF was observed in 39 patients (3.8%) and in 39 lesions (2.9%). The results also show that of those with SF, 20% experienced ISR whilst only 14.6% of those without SF were affected. The rate of those with major adverse cardiac events at 9 months was significantly higher in the SF group than the non-SF group (25.6% and 2.3% respectively), as were the myocardial infarction rates (5.1% compared to 0.4%) and the rates of stent thrombosis (5.1% and 0.4%).

Table 3-2: Incidence of fracture in drug-eluting stents (Alexopoulos et al., 2011)

Authors	Type of study	IVUS	No of pts	No of angio F/U	No of lesions	No of SF	Cypher/Taxus	Incidence
Angio/sporadic IVUS:								
Lee MS et al[2]	Retrospective	No	2728	530	unknown	10	10/0	1.9%
Popma et al[7]	Retrospective	No	305	305	305	4	4/NA	1.3%
Kim et al[16]	Randomized	No	415	415	415	7	6/1	1.7%
Yang et al[15]	Retrospective	16	479	479	686	27	22/NA	3.2%
Chung et al[14]	Retrospective	16	8180	4189	4189	37	37/0	0.84%
Ino et al[8]	Retrospective	22	273	273	364	18	18/NA	4.9%
IVUS additive value:								
Lemos et al[10]	Prospective	11	192	121	221	2	2/NA	1.7%
Lee SH et al[11]	Prospective	14	868/26ISR	366	1109	10	10/NA	2.7%
Lee SE et al[13]	Retrospective	2	3365	1009	unknown	17	15/2	1.5%
High rate of IVUS follow up:								
Aoki et al[1]	Prospective	67.1%	280	256	307	8	8/NA	3.1%
Okumura et al[17]	Prospective	62.4%	151	138	169	4	4/NA	2.4%
Yamada et al[12]	Prospective	100%	56	56	83	3	3/NA	3.1%
Umeda et al[18]	Prospective	90.2%	422	382	430	33	33/NA	7.7%

F/U – follow up; ISR – in-stent restenosis; IVUS – intravascular ultrasound; NA – not applicable; SF – stent fracture.

3.3 Atherosclerotic Plaque

3.3.1 Properties of Atherosclerotic Plaque

Atherosclerotic lesions were initially characterised by Stary et al. (1994, 1995) and Stary (2000), and these studies divided lesions into seven morphological types (Table 3-3). The lesions develop slowly over the course of many years and have a variety of problems associated with each of the different stages.

The mechanical properties of type I and II lesions vary very little from that of the normal artery. Intimal thickening, with layers of smooth muscle cells and initial macrophage foam cell deposits, is not macroscopically visible. The lesion progression, however, becomes visible as the lipid deposits develop between layers of foam cells and smooth muscle cells, and the fatty streak of the type II lesion appears. By the time the lesion develops to type III, the extracellular lipids between the layers of smooth muscle cells begin to change the way the vessel behaves. The lack of structured elastin layers and pools of lipid deposits makes the tissue more heterogeneous and isotropic.

Table 3-3: Classification of atherosclerotic plaque as defined by Stary et al. (1994, 1995) and Stary (2000).

Lesion Type	Characteristics
Type I (initial lesion)	Initial macrophage foam cell deposits
Type II (fatty streak)	Fatty streaks with stratified layers of foam cells and smooth muscle cells with lipid deposits. Macroscopically visible as fatty streaks.
Type III (intermediate lesion)	Extra-cellular lipid pools beneath foam cells.
Type IV (atheroma)	Lipid core with foam cells, proteoglycans and isolated smooth muscle cells. Lesion is now clinically apparent.
Type V (fibroatheroma)	Fibrous connective tissue layered with lipid core.
Type VI (complicated plaque)	Surface defect, haematoma and thrombosis.
Type VII (calcific plaque)	Calcified lipid core
Type VIII (fibrotic plaque)	Minimal lipids with fibrous connective tissue.

The development of the lipid core characterises the advancement of the tissue into types IV and V lesions. The homogeneity of the pre-atheroma is lost as the extracellular lipids accumulate into the lipid core. The insignificant amount of smooth muscle cells and collagen, together with the lipid core, makes the lesion soft and fairly isotropic. Any advancement of the atheroma to include a surface defect, haemotoma or thrombosis is called a complicated plaque or ruptured lesion. The build-up of collagen and smooth muscle cells make the lesion moderately stiff and anisotropic. The atheroma is the first to be considered clinically relevant.

The properties of type VII lesions become more heterogeneous, with soft lipid deposits and localised hard calcifications. As with type VIII (fibrotic plaque), the lesions are stiffer than types I-VI. The fibrotic plaques, however, are more homogeneous than calcific plaques, with more calcification and no lipid core remaining.

Plaques that are softer and lipid-rich are more prone to rupture than their harder, collagen-rich counterparts (Loree et al., 1994b). In a study of different types of atherosclerotic lesions taken within 24 hours post-mortem, Fernandez-Ortiz et al. (1994) exposed the plaques to flowing blood in order to calculate the relative thrombogenicity of the different plaque components. It was discovered that the largest thrombus formation was associated with the atheromatus core when compared with other types of lesions. Whilst such plaque ruptures are more likely to lead to stroke or myocardial infarction, it is the heavily calcified lesions that are thought to adversely affect the structural integrity of stents and are therefore more likely to contribute to SF.

The progressive changes that occur in the intima as atherosclerosis develops are central to understanding the nature of the different mechanical properties associated with each lesion type.

As an inhomogeneous tissue, accurately quantifying the mechanical properties of atherosclerotic plaque is a challenging undertaking. Due to the regulations surrounding the removal, storage and use of human tissue (Human Tissue Act, 2004), acquiring human atherosclerotic plaque for testing is a difficult task. There is, however, data available in literature to which mathematical models can be fit to obtain constants for FE modelling.

A study was carried out by Loree et al. (1994a) to investigate the mechanical properties of human atherosclerotic plaque. The study involved the incremental loading of fibrous caps, dissected from the arterial layers and necrotic plaque components, in the circumferential direction in order to assess the stress-strain relationship for the tissue. All 26 specimens undergoing testing were classified histologically as cellular (n=12), hypocellular (n=9) and calcified (n=5). At a physiological applied stress of 25 kPa, the average tangential moduli of the cellular, hypocellular and calcified samples were 927±468 kPa, 2312±2180 kPa and 1466±1284 kPa respectively. The hypocellular samples were found to be approximately twice as stiff as those categorised as cellular.

3.3.2 Prevalence of Atherosclerotic Plaque and In-Stent Restenosis

With PCI being performed on as much as 80% of all cases (NICOR, 2013), the clinical success of the devices is critical when determining whether to use a bare metal (BMS) or DES and which, if any, drug coating has the highest success rate for preventing restenosis.

After the first introduction of BMS in 1993, stents were shown to be more effective at preventing restenosis when compared to balloon angioplasty procedures (Serruys et al., 1994; Fischman et al., 1994).

The use of SESs have been used successfully to reduce the risk of restenosis. Morice et al. (2002) reported a randomised, double-blind trial to compare the use of SES with BMS. The trial included 238 patients, 50% of whom were allocated the SES Cypher stent, whist the rest were assigned the standard BMS. At the follow-up angiogram 26.6% of those in the BMS group had restenosis of 50% or more compared to none in the sirolimus stent group. There were no occurrences of stent thrombosis in either group, although the overall proportion of cardiac events up to one year after surgery was 28.8% for the BMS group and 5.8% for those with the SES.

In another randomised double-blind study by Moses et al. (2003), in which 533 of the 1058 patients were treated with a SES and the other 525 were allocated a BMS, the rate of restenosis (defined as stenosis of 50% or more of the luminal diameter) was 3.2% for the sirolimus group and 35.4% for the standard stent group. The total number of cardiac events during the 270 days of follow-up was reduced from 18.9% with the BMS group to 7.1% in those with the SES.

3.4 Causes of Stent Fracture

Despite the current inability to accurately quantify the rate at which SF occurs, the phenomena have been proven to be influenced by a large number of variables including stent design, strut size, material and material form used, location of lesion and degree of calcification.

3.4.1 Materials

Material choice for stents is dependent on the deployment method. Balloon expandable stents are required to be able to be plastically deformed by the inflation of a balloon as it must remain in its expanded shape after removal of the balloon. For this reason, a low yield strength and high elastic modulus is necessary to enable the expansion to occur

with the relatively low internal pressures and for the recoil after deformation to be minimal. Conversely, as self-expandable stents are manufactured in their full diameter, the elasticity of the material for such devices is critical. It is important that the yield stress is high to enable to the device to be crimped without fracture. Materials with shape-memory are utilised in this application and the material recoils back to its original manufactured state after release in the vessel.

The most important factor when considering the choice of material for manufacturing stents is biocompatibility, to ensure that there are no adverse effects on the body and so that the material is not debilitated by the corrosive environment. There are currently four main options that fall into such categories and are therefore widely used in stent manufacture; stainless steel, nitinol, cobalt-chromium and tantalum (Stoeckel et al., 2002; Thierry et al., 2004). These materials all exhibit several other properties that are important for such devices, including flexibility, elasticity, radiopacity, and uniform radial strength.

Stainless steel (SS) is the material from which the vast majority of stents are made, usually type 316L. This is largely due to its ease of deformability, thus the large amount of plastic deformation it can withstand before fracture. This makes 316L SS ideal for balloon expandable stents. Furthermore, the ease of availability and low cost of the material make it desirable for the application. Stainless steel is also highly corrosion resistant, thus making it the most commonly used material for stent manufacture (Mani et al., 2007). There are limitations associated with 316L SS, including its ferromagnetism, which would make the devices non-MRI compatible. The composition of the alloy may mean that its biocompatibility can be an issue. With the weight percentages of the nickel, chromium and molybdenum in 316L SS being 12, 17 and 2.5 respectively, the

release of any nickel from bare metal stents have been shown to cause allergic reactions (Haudrechy et al., 1993). The release of nickel, chromate or molybdenum ions in particular from SS stents may cause local inflammations, triggering intimal hyperplasia and in-stent restenosis (Mani et al., 2007).

Nitinol is a nickel-titanium alloy, of which 55% is nickel and the remainder titanium (Trepanier et al., 2000). The material has suitable mechanical properties but is popular largely due to its shape-memory and superelasticity, making it ideal for self-expanding devices. The alloy is manufactured at a slightly larger diameter than that of the blood vessel, with a transformation temperature of about 30° (Stoeckel et al., 2004). This means that the stent can be plastically deformed at room temperature or lower, and will revert to its original shape once the temperature reaches the transformation temperature. This allows the stent to be crimped around a delivery device before implantation, and revert to its original state once in position inside the body, where there is a significant increase in temperature (Mani et al., 2007). Although nitinol is generally thought to have good biocompatibility (Stoeckel et al., 2004; Park et al., 2007), its corrosion resistance is under some debate. The release of Ni ions have caused some concern (O'Brien et al., 2009), however the rate of release and overall concentration of nickel in the blood have been shown to be below the estimated average dietary intake of the metal thus should not have any adverse effects on the patient (Stoeckel et al., 2004). Despite this, reported corrosion of nitinol stents (Heintz et al., 2001) suggests that the nickel release may be an important factor in SF.

Tantalum is used due to its flexibility and high radiopacity and has also been shown to be very corrosion resistant due to its highly stable oxide layer (Mani et al., 2007). The main disadvantage to the use of tantalum in stents is the increased likelihood of fracture

during deployment due to the fact that its yield strength and tensile strength are very similar. Whilst its visibility, corrosion resistance and biocompatibility (Matsuno et al., 2001) are very good, the poor mechanical properties of tantalum mean that the material is less widely available than other metals for this application.

Cobalt-chromium alloys are very biocompatible and have excellent radial strength (Kereiakes et al., 2003). In addition, stent strut thickness has been shown to impact the rate of restenosis (Briguori et al., 2002) thus the ability to draw Co-Cr into ultra-thin struts without losing the strength of the material is one of its most appealing properties.

3.4.2 Design

The structure, geometry and dimensions of stents have a huge impact on their performance. There are several design characteristics that are vital for optimum performance of the devices including flexibility, high radial strength, low elastic recoil, and minimal foreshortening.

Studies have shown that the likelihood of SF is largely dependent on the size of the struts, and also the grain size of the material (Murphy, et al., 2003). Often, the material properties used when designing stents are those observed at the macroscale, however at such small grain sizes the metals behave differently (Savage et al., 2004). As described by Murphy et al. (2003), the strain at necking for 316L SS is hugely dependent on the strut size. A size-based stress-strain relationship exists for struts that are less than 500 µm in diameter, above which macroscale properties apply. As a result, it is critical that accurate material properties of the materials in such small dimensions are considered during the design process.

3.5 Previous Experimental Work

Numerous investigations of the behaviour of stents have been carried out. A good understanding of the stress-strain behaviour of stent struts *in vivo* can provide an indication of the causes of SF. With the use of specially manufactured 'struts' of varying widths, Murphy et al. (2003) investigated the effect of strut size on the stress-strain behaviour of stents. The mechanical testing was carried out using a repeatable gripping technique, which immobilised the ends of the specimen and allowed tensile testing to be performed. Their results showed a variation in the stress-strain behaviour between the different strut widths, indicating a size-dependence of the stress-strain behaviour of SS 316L at small sizes. The implication of this study is that small stent struts (below 500 μm width) may be prone to unexpected local failure if macroscale material properties were used during design calculations.

Due to the prevalence of SFs in nitinol stents, a thorough investigation of such devices and subcomponents thereof was carried out by Pelton et al. (2008). Self-expanding nitinol stents were laser-machined for the purpose of this study from thin walled tubes before being fully expanded into their final dimensions. Diamond-shaped specimens were fabricated to represent the stent strut 'V' shapes with similar geometries, in order to carry out fatigue testing. This meant that pulsatile fatigue properties of the nitinol stents could be obtained. It was found that the fatigue life of both the subcomponents and the stents increased with increasing mean strains.

3.5.1 Silicone Mock Arteries

Due to the strict regulations surrounding experimentation on human tissue and the difficulty obtaining calcified arteries of an animal with large enough vessels, silicone or latex mock arteries are often used as an alternative for experimental testing. Whilst

imitation vessels are designed and manufactured to be as similar to arteries as possible, their properties are not well enough documented for any material to replicate them accurately. Such differences can have a huge impact on the outcome of any experimentation and as such any inaccuracies must be taken into consideration when making conclusions.

The issues associated with the high frequency testing and durability of mock arteries have been considered by Conti et al. (1999). Using an accelerated recreation of the internal pressure change experienced in vivo, the radial compliance of mock arteries tested at high frequency was compared to that of those tested at 72 bpm. The radial compliance for frequencies up to 800 bpm was found to be close to that at 72 bpm, above which the compliance decreased significantly. Using the same methods as above, the durability of silicone versus latex mock arteries was examined by Conti at al. (2001), in which it was found that latex mock arteries lose their integrity after only 100 million cycles compared to 400 million cycles for the silicone alternative. The difference in radial compliance between the two materials was confirmed by the experimentation reported by Rajesh et al. (2005) using similar methods.

3.6 Finite Element Analysis

FE analysis is a numerical method by which approximate solutions for problems can be obtained. The system can be discretised into a number of finite elements of simple geometry, which are connected at 'nodes' (Cook et al., 2001). This arrangement of nodes and elements is called a mesh. The problem can then be solved at each element using simple stress-strain equations. The use of FE analysis begins with the pre-processing stages, which includes the model creation and mesh generation. Often, the model will be created in an alternative modelling program and imported into the FE analysis

software as a mesh, using discretisation algorithms. Material properties and boundary and loading conditions will then be defined for each component (Martin et al., 2011).

FEA provides an advantage over traditional in vivo studies as it allows difficult numerical analyses to be carried out more quickly and efficiently than manual calculations and provides a platform for measuring quantities that can be difficult to measure in a physical stent. Furthermore, the cost of computational modelling is significantly lower than that of mechanical testing. The FE method has been used extensively to determine the stresses in both the implanted stent and vessel, and the expanded stent in isolation. FEA requires the material properties and geometry of stent and blood vessel being modelled, and the loading conditions to be investigated. Many studies have been carried out to investigate the effects of stents on the vessel both during deployment and throughout its lifetime, usually regarding possible restenosis and stent thrombosis rates. It is, however, important to note that FEA has limitations in that the construction of vessel and stent models often relies on idealised geometry and may lead to results that vary slightly from that of realistic stent models. Also, distortions in the shapes of elements may arise during the meshing of large or irregularly shaped models, which can result in distorted solutions (Martin et al., 2011).

3.6.1 Soft Tissue Modelling Methods

In order to carry out representative modelling of stents in bifurcations, the mechanical properties of both plaque and arteries must be known. The performance of stents and rate of SF *in vivo* may be dependent on the amount of calcification in the plaque. For this reason, atherosclerotic lesions play a vital role and must be adequately described by the FE model.

The accuracy with which human arteries are represented in FE models has changed hugely over the decades. They have previously been represented using a variety of mathematical models ranging from the relatively simple linear isotropic model (Chua et al., 2004) to layer-specific anisotropic hyperelastic models (Holzapfel et al., 2000).

Most recently, the Holzapfel-Gasser-Ogden (HGO) model has been devised to describe anisotropic hyperelastic materials such as arterial tissue (Holfzapfel et al., 2000) and is included in most commercial FE packages. As the most accurate model to date, the HGO model was used by Holzapfel et al., (2000) to represent the specific arterial layers to assess the amount of vessel injury during stent deployment.

Before the introduction of the HGO model, hyperelastic isotropic models were used extensively in FE analysis to represent arteries. One of the most popular such models is the Mooney-Rivlin hyperelastic constitutive equation (Mooney, 1940), described by Prendergast et al. (2003) and Lally et al. (2005). Layer-specific hyperelastic models (Gastaldi et al., 2010 and Martin et al., 2013) were later used to describe the intima, media and adventita separately.

Linear isotropic FE modelling, on the other hand, is one of the simplest to carry out and the cheapest both in resources and computing time. Simplifying the tissue to a linear material ensures that computational analyses can be completed in a relatively short time, however a compromise will be made on the accuracy of the results.

3.6.2 Finite Element Analysis of Stents

There have been many studies carried out using FE analysis in order to quantify stresses in stented vessels and accurately describe the interaction between the vessel and the stent. Two different stent designs were analysed by Lally et al. (2005) to test the hypothesis that different stent designs will behave differently within the artery, thus

result in different levels of vascular injury. The two stents that were examined were the S7 (Medtronic AVE, Minnesota, USA), which has a modular stent design with circular cross-section, and the slotted laser-cut tube NIR (Boston Scientific, Massachusetts, USA). In order to carry out this study, the two stent designs were modelled in a FE software using geometries measured from fully expanded devices. Each stent was created in a planar state, taking advantage of the repeating units of each design. The models were then transformed into their cylindrical states by transferring the nodal coordinates from the Cartesian coordinate system into a cylindrical coordinate system. The vessel was modelled as an idealised cylinder with a localised crescent-shaped atherosclerotic lesion. The artery wall was modelled as an isotropic hyperelastic material. The material properties of the stent were modelled as that of linear elastic 316L SS (E=200 GPa, v=0.3). The varying geometries of the two designs created significantly dissimilar reactions in the vessel. The NIR caused a greater volume of arterial wall stresses than that of the S7, thus the NIR would be expected to cause more vascular injury than the S7. In addition, the S7 was found to have greater radial retraction, maintaining lower stresses of the vessel walls, whilst sustaining superior structural integrity.

In a study carried out by Chua et al. (2004), an investigation of the in vivo expansion of a slotted tube stent design was carried out using FEA. The idealised stent geometry, artery, plaque and inflation balloon was created using a FE software, utilising the repeating unit symmetry of the design to eliminate the need to create only one section of the stent thus significantly reducing the simulation time. The stent material properties were defined as that of Stainless Steel 304 (E=193 GPa, v=0.27), whilst the properties of the plaque and artery were based on those published by Veress et al. (2000) (E=0.00219 GPa, v=0.499 and E=0.00175 GPa, v=0.499 respectively). In order to accurately resemble

the implantation procedure, a balloon catheter was created inside the lumen of the slotted tube. The simulation process involved inflating the balloon using a pressure load, thus expanding the stent as would have occurred in vivo before deflating the balloon and leaving the stent in place. The highest stresses in the stent were seen at the corners of the slots and the stress distribution of the plaque and artery was much higher at the plaque location than the artery, demonstrating that the most likely location for SF are those at which struts come into direct contact with calcified plaque regions.

Rogers et al. (1999) carried out a FE analysis of stent deployment focusing on the effect of the balloon-artery interactions. Their study involved the use of idealised stent models and showed that the contact stresses between stent struts was markedly higher with higher inflation pressures and wider stent strut spacing. The stent strut geometry is therefore very important when considering strut fracture, as is the initial inflation pressure.

Four stents of varying geometries were modelled by Tambaca et al. (2011) and analysed using FE analysis and the response of the stents under uniform compression and bending conditions were investigated. The compression force was applied uniformly in the radial direction, whilst the bending force was applied pointwise, both at either end of the stent and at the centre point. Each of the stent geometries were based on devices that are currently commercially available; the Express, Cypher, Xience and Palmaz stents. For each of the stents, different variables were altered to enable the comparison of different geometries. The results suggested that with respect to rigidity, stents that are not fully dilated are less rigid and therefore exhibit larger deformation. Increased deformation can also be seen with non-uniform pressure loads. Both observations emphasise the need for pre- and post-dilation of the vessel during stent implantation. Regarding open-

and closed-cell stent designs, open-cell stents showed increased flexibility during bending. Sinusoidal struts, such as those in Cypher stents, proved to have the highest levels of deformation under uniform radial loading.

4 Aims and Objectives

The aims of this study were to develop and validate an idealised stent model that will be design-independent and represent the mechanical behaviour of a coronary stent device, and to use the idealised stent model to assess the likelihood and expected locations of SF in angulated vessels undergoing hinge-motion bending.

The first aim was completed by creating and validating a FE model of a deployed cardiovascular stent that had been idealised to a cylinder. The idealised cylindrical stent meant that the model did not allow for any intricacies in the stent design. A 3-point-bend experimental test was carried out on a deployed stent and the data was used to calculate an "effective" modulus to represent the elastic modulus of the device. This 3-point-bend test was then replicated using FE analysis software ANSYS Mechanical APDL (ANSYS 14.5 Mechanical, ANSYS, Inc., Canonsburg, PA, USA). The FE model was then validated to ensure that it was fully representative of the behaviour of the stent in the mechanical test.

The resulting idealised stent was then used carry out a FE analysis of the stent stresses in a bifurcated lesion. An angulated stented FE vessel was created using the effective modulus calculated in Chapter 5. The vessel was then subjected to a 20° displacement to represent the movement of the stent throughout the cardiac cycle. The model was assessed with five different material models representing the artery: one linear model, two single-layer hyperelastic models and two hyperelastic models defined with 3 separate arterial layers. Stress analysis was then carried out to assess the likelihood and likely locations of stent SF in the device.

5 Idealised Stent Model Development

5.1 Introduction

In order to evaluate the success of PCI, FE analysis has been carried out extensively to evaluate the deployment technique and the mechanical response of both the stent and vessel after implantation (Lally et al., 2005). Whilst the published work is comprehensive, it is almost exclusively focused on the level of vascular injury incurred during deployment (Hajiali et al., 2014; Liang et al., 2005; Shang, 2014). In short, much of the published work involving stent-artery interactions is thorough in its approach to calculating vascular stress but lacking in consideration to the stent itself. The stresses undergone by the stent and how this might relate to SF is little understood.

To evaluate the stent stresses in the *in vivo* environment, specifically in the regions where the stent is likely to be under higher levels of stress such as curved vessels and bifurcations, FE analysis has been used to recreate and analyse the environment. To ensure the results of the stress simulations would reliably represent any stent structure or design, an idealised, design independent stent model was necessary for the simulations. This chapter describes the process by which the models used in future chapters was created and validated.

The purpose of the work in this chapter was to create and validate a suitable model to account for the mesh-like structure of the stent and allow patterns to be observed on the device as a whole, whilst eliminating any distortions created by specific stent designs. To create such a model, the stent was idealised to a cylindrical tubular structure. This necessitated the calculation of an 'effective' elastic modulus to describe the device as a whole. Subsequent chapters focus on the effect of bending of stents deployed in coronary arteries, particularly those in bifurcations, which undergo hinge-

motion repetitive bending throughout the cardiac cycle. The 'effective' modulus, therefore, was calculated based on the bending stiffness of deployed stents.

Initially, a 3-point-bend test was carried out on a deployed stent using a dynamic mechanical analysis (DMA) machine. For the effective modulus calculation, bending stiffness was obtained from a 3-point-bend test using a dynamic mechanical analysis (DMA) machine. An idealised cylindrical stent FE model was created and the results from the 3-point-bend test were then fed into the model as the elastic modulus. Other model parameters could then be adjusted to ensure that it was representative of the deployed device.

5.2 Methods

5.2.1 Mechanical Testing

The mechanical testing involved in the idealised model validation was a 3-point-bend test. From this, the force-deflection graphs were obtained and analysed so that a bending stiffness could be calculated.

A stent was initially chosen for testing based on suitability undergoing a 3-point-bend test with the equipment available. There were limited stents available for testing and it was important that the results could be repeated to check for reliability.

The device chosen for testing was a 2.25 mm nominal diameter and 26 mm long Resolute Integrity Zotarolimus-Eluting Coronary Stent System (REF RSINT22526X; Medtronic, Minneapolis, MN, USA). This stent was chosen because it was the only one of which there were multiple available for use with the same diameter and length. A BasixCompak inflation device (Merit Medical, South Jordan, UT, USA) was used to expand the stent with the appropriate pressure for nominal deployment. As per the

pressure chart on the device packaging, a pressure of 9 atm was applied for a nominal deployment of 2.3 mm. The pressure was applied for a duration of 20 seconds to allow optimal plastic deformation of the struts.

The stent was deployed free, i.e. with no encasing mock-artery tubing. The outer diameter of the expanded device was then measured using a Vernier calliper and noted for future reference. The deployed stent can be seen in Figure 5-1 below.
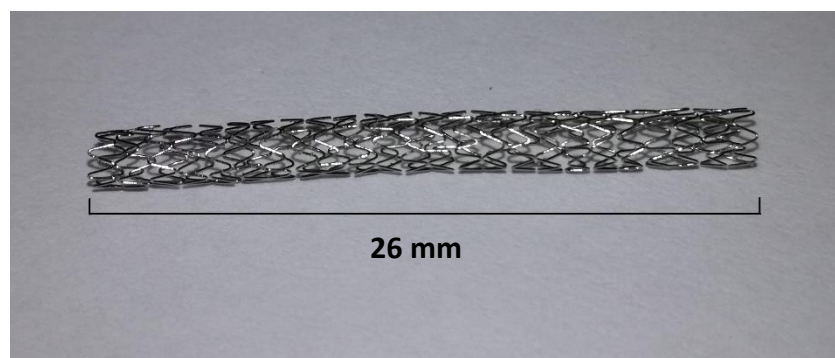
Figure 5-1: Deployed stent

A 3-point bend test was carried out on the expanded stent experimentally using a DMA machine, the Q800 (TA Instruments, New Castle, DE, USA). Adjustments to the existing sample supports were made to ensure that they complied with the ASTM F2606-08 standard guide (ASTM, 2008) for the 3-point bending of balloon expandable coronary stents. In accordance with the ASTM standard, the support span length to stent diameter ratio must be at least 4:1. The span of the supports was therefore selected to be 20 mm, which was greater than the 9 mm necessary for the 2.25 mm nominal diameter of the Resolute Integrity. The supports were also required to be cylindrical, and with a diameter appropriate for the sample diameter and span length (span length > lower support diameter + upper support diameter + 2 x (test article diameter)). With

a span length of 20 mm and test article diameter of 2.25 mm, lower support diameter +
upper support diameter < 20 mm – 2 x 2.25 mm. From this, the support diameters were
required to be less than 7.75 mm. The supports used were altered with additions
fashioned from 5.2 mm diameter rigid silicone tubing to provide adequate support for
the samples (Figure 5-2 and Figure 5-3). The silicone tubing was taped into place.
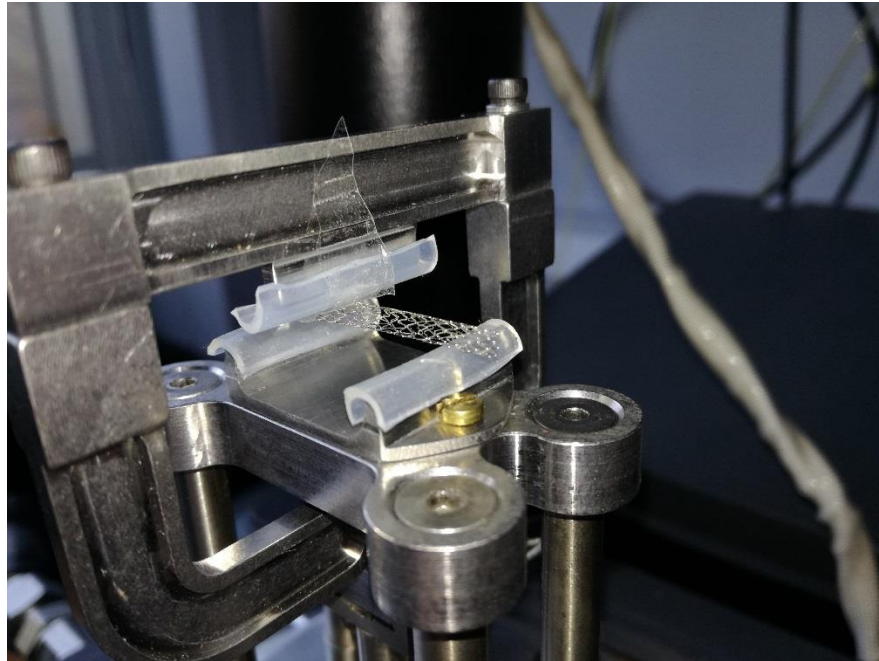
Figure 5-2: Stent in dynamic mechanical analysis machine
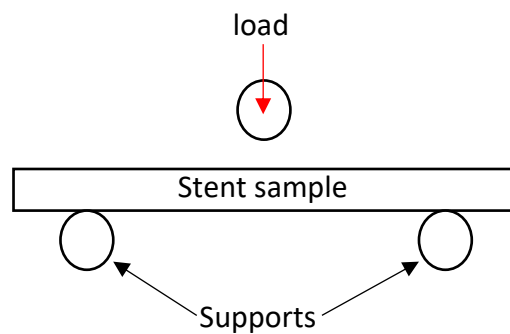
Figure 5-3: Schematic for 3-point-bend test

The machine was first calibrated for displacement using a rectangular plate to ensure the measurements being taken were accurate. Once this was complete, the sample was moved into position. The stent was placed to rest on the supports, relying on visual inspection to ensure that it was positioned centrally in the longitudinal direction.

The "tubular" setting in the DMA software was used to categorise the sample, with the appropriate inner and outer radii input as per measurements taken after stent deployment. A 0.001N pre-load was applied vertically to ensure correct contact between the stent and load applicator and prevent any movement of the sample during testing. It also ensured a constant starting point for the load-displacement graph between the 3 samples subjected to the 3-point bend test. The applied load of 0.05N/min was then applied to a maximum of 0.1N. Results obtained were then exported to a text file and analysed using Microsoft Excel (Microsoft Corp., WA, USA).

The mechanical testing process was repeated for each of the 2 remaining stents for a total of three sets of data.

5.2.2 Effective Modulus Calculation

As the stent model was being idealised to a tube, the material model of the stent material (a cobalt-based alloy) was not an appropriate representation of the device as a whole. The stent exhibits different mechanical behaviour to that of a metal cylinder due to the difference in material volume; thus, it was necessary to first calculate a theoretical, effective elastic modulus to validate the model. Future chapters will focus on the effect of bending the devices, therefore it was appropriate to base the elastic modulus on the bending stiffness of the device.

Equation 5-1 below was used to calculate the bending stiffness of the stent with the results of the 3-point bend test. The derivation of the equation is shown in Appendix A.

$$E_{stent} = \frac{-PL^3}{48y_1I}$$

<div align="right">**Equation 5-1**</div>

Where E_{stent} represents the elastic modulus of the stent, accounting for the mesh-like structure, P represents the load applied, L is the length of the stent, y_1 is the deflection of the stent and I is the second moment of area of the beam.

5.2.3 Model Generation

Once the stent elastic modulus had been calculated, it was necessary to use the acquired data to create an idealised stent for subsequent investigations. The 3-point-bend test was replicated using FE analysis software ANSYS Mechanical APDL (ANSYS 14.5 Mechanical, ANSYS, Inc., Canonsburg, PA, USA). Five models with the same geometry but different boundary conditions were created to analyse the most appropriate representation of the mechanical testing.

The models were in the X, Y and Z orientations as shown in the schematic below (Figure 5-4). The models attempted are summarised in Table 5-1.
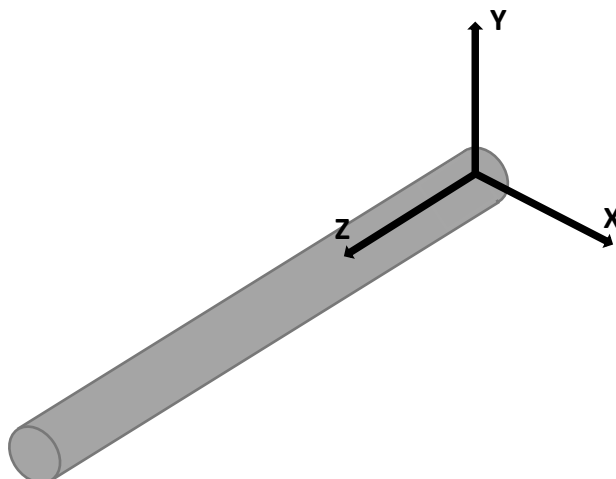
Figure 5-4: Schematic to show X, Y and Z directions for all stent models

The model was defined with a stent outer diameter of 2.46 mm as per the average outer diameter from the stent samples from the mechanical testing (Table 5-2) in section 5.2.2).

The model was initially created to represent the mechanical testing as closely as possible. The stent was generated by first creating four cylinders of diameter 2.46 mm with 3 mm, 10 mm, 10 mm and 3 mm depths, resulting in a combined depth of 26 mm. The four parts were then glued together so that the model would behave as one volume but the original lines separating the sections remained. This meant that the boundary conditions could be applied more easily to the model (Figure 5-5). The volume was then deleted so that only the remaining areas were left to form the outline for the stent.

Due to the relative slenderness of the struts, shell elements were used to represent the material. This meant that the areas remaining after deleting the volume were meshed using SHELL281 elements. The element description can be found in Appendix B. This element allows a user-defined value to dictate the thickness of the elements. Thickness was defined to be 88.9 µm as per the thickness of the Resolute Integrity struts (Medtronic, 2013).
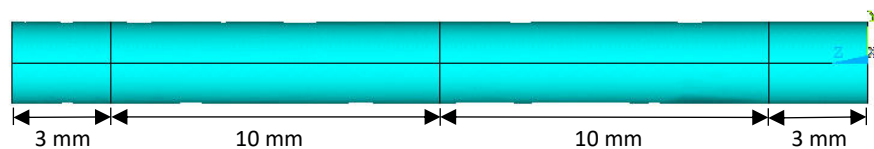
Figure 5-5: Idealised stent areas for model 1

Once the geometry was created, five variations of boundary conditions were applied to the stent to ensure that the experimental testing was represented as accurately as possible. A summary of the models can be seen in Table 5-1 below.

Table 5-1: Summary of the boundary conditions of each of the five models

Model No.	Supports	Load
1	Single point constrained for zero displacement in UY, UX	Divided over 3 nodes. Nodes also constrained for zero displacement in UX
2	Three nodal point constrained for zero displacement in UY	Divided over calculated area of 588 nodes. Nodes also constrained for zero displacement in UX
3	Line constraints along a line of nodes parallel to X axis. Constraints applied for zero displacement in UY and UX	Divided over3 nodes. Nodes also constrained for zero displacement in UX
4	Line constraints along a line of nodes parallel to X axis. Constraints applied for zero displacement in UY and UX	Load divided over 50 nodes in a line parallel to the X axis. Nodes also constrained for zero displacement in UX
5	Rigid link supports	Divided over calculated area of 588 nodes. Nodes also constrained for zero displacement in UX

For each of the models, the load applied is 0.04 N. The explanation for using this value can be found in Results section 5.3.1.

5.2.3.1 Model 1

Model 1 was a simple idealised cylindrical stent with single nodal constraints to represent the supports and the load applied to a single node on the top of the cylinder.

Single nodes were identified at locations at the bottom of the stent and 3 mm from either end, to correspond with the supports on the DMA 3-point-bend test, on which structural constraints were applied in both UY and UX directions. The boundary conditions can be seen in Figure 5-6. A single node was identified at the top of the model halfway along the length of the stent, as shown by a red arrow in Figure 5-6, on which the 0.04 N vertical load was applied. The node on which the load was applied was also constrained in UX to add stability to the model.

All boundary conditions were applied to nodes that had been identified to be as close to the Z axis as possible.
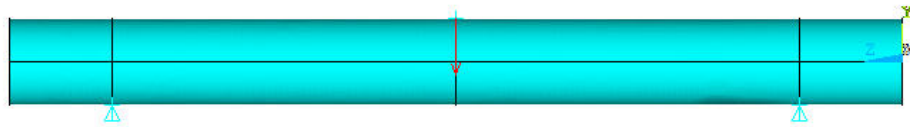
Figure 5-6: Boundary conditions for Model 1

5.2.3.2 Model 2

The boundary conditions in Model 2 were designed to eliminate any potential localised indentations from a point load and supports. This meant that the supports were represented by 3 nodes at each location, calculated to be 3 mm from either end of the stent at the bottom of the cylinder. The support nodes were constrained in the UY direction only.

The load was distributed over 588 nodes at the location of the cylinder that would have made contact with the load applicator as per the experimental testing.

The contact area was calculated as per Hertzian theory (Williams and Dwyer-Joyce, 2000).

Using the equation:

$$\alpha = \sqrt[3]{\frac{3RF}{4E^*}}$$

Where α is the contact area radius, *R* is the radius of the load applicator, *F* is the load applied. E^* is defined as:

$$\frac{1}{E^*} = \frac{1 - \gamma_1^2}{E_1} + \frac{1 - \gamma_2^2}{E_2}$$

where E_1 and E_2 are the Young's moduli of the load applicator and the stent respectively and γ_1 and γ_2 are the Poisson's ratio of the load applicator and the stent respectively. The schematic in Figure 5-7 below shows the contact between the load applicator and stent.
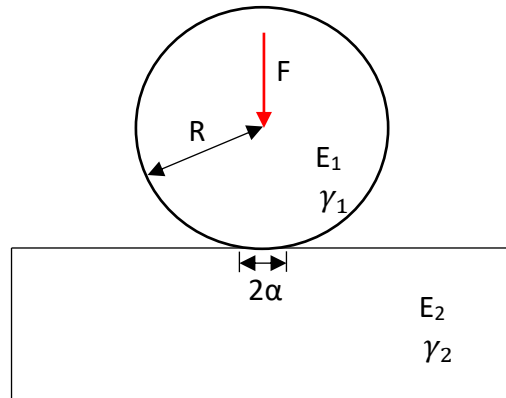
Figure 5-7: Schematic to show load applicator and stent in contact

The load applicator in the DMA was adapted so that the contact material was a section of silicone tubing. As the specific mechanical properties of the tubing used was unavailable, the Young's modulus for the material was derived from experimental data published by Martins et al. (2006) and defined to be 78.947 kPa. The Young's modulus used for the stent was that derived experimentally in section 5.2.1 and defined to be 7.89 MPa. γ_1 and γ_2 were both defined to be 0.3.

With a load applicator radius, R, of 2.6 mm and a load applied of 0.04 N, the contact area was defined by a length of 1.94 mm along the length of the stent, and a depth of 1.51 mm along the width of the stent (Figure 5-8).

1.51 mm

1.94 mm
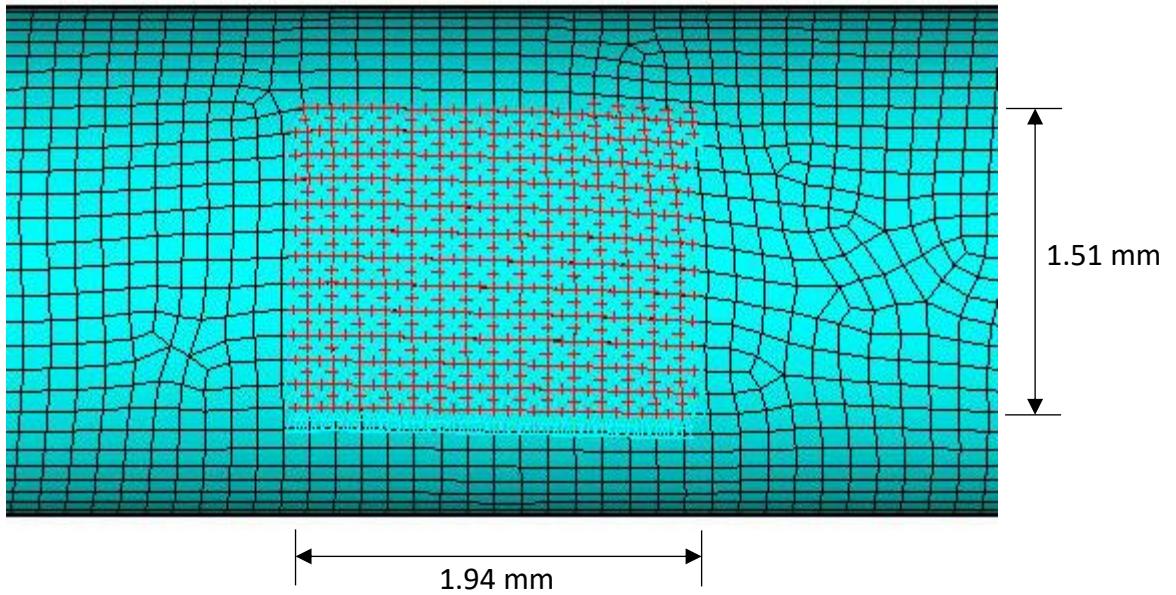
Figure 5-8: Contact area of the load applied for Model 2

Once the contact area had been calculated, the load was applied to all the nodes within that area. This meant that the load was divided over 588 nodes. These nodes were also constrained in the UX direction to prevent sideways movement.

The boundary conditions can be seen in Figure 5-9.
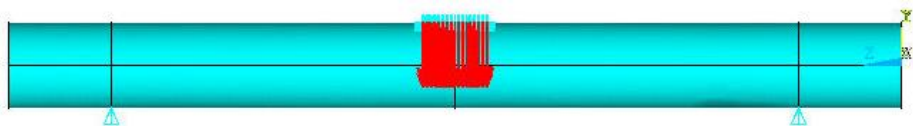
Figure 5-9: Boundary conditions for Model 2

5.2.3.3 Model 3

In Model 3, the supports were represented by a selection of nodes in a straight line parallel to the X axis. The number of nodes constrained was calculated based on the length of contact as calculated for Model 2. This meant that the selected nodes were 3 mm from either end of the stent and covered a length of 1.94 mm. This resulted in 25 nodes at each support location constrained in both the UX and UY directions.

The load was applied to three nodes halfway along the length of the stent, which were also constrained in the UX direction. The BCs can be seen below in Figure 5-10.
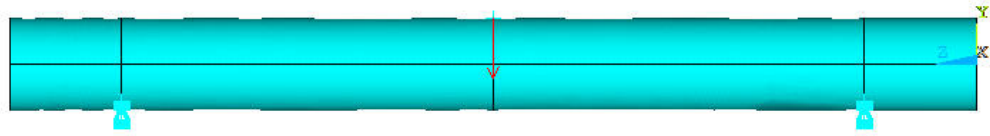
Figure 5-10: Boundary conditions for Model 3

5.2.3.4 Model 4

The supports for Model 4 were the same as that for Model 3. A total of 25 nodes at each support location were selected. The nodes were aligned in a straight line parallel to the X axis. They were constrained in both the UY and UX directions.

The load for Model 4 was also applied in the same way as the supports. A selection of 25 nodes along the centre line at the top of the stent were selected. The nodes covered a length of 1.94 mm as per the contact length calculated for Model 2. This meant that the 0.04 N load was divided over the 25 nodes.
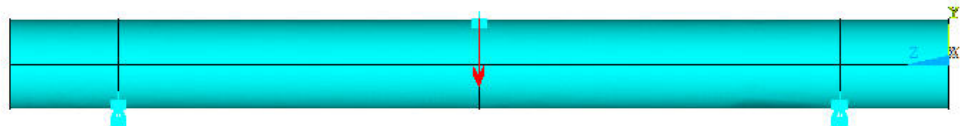
Figure 5-11: Boundary conditions for Model 5

5.2.3.5 Model 5

Model 5 utilised a rigid link element to represent the radius of the cylindrical supports. This method required two nodes to be defined at the location of the centre of the cylindrical supports as per the mechanical testing, which was 2.6 mm below the bottom of the stent. The two nodes on the base of the stent in the location most likely to have contact with the supports were then identified. A rigid link element (MCP184) was then

created between the two new nodes and the corresponding node at the base of the stent. The element definition can be found in Appendix B.

The two new nodes were constrained in all directional degrees of freedom (UX, UY and UZ).

The load was applied in the same was as in Model 2. The 588 nodes within the calculated contact area were selected and the load divided over them. These nodes were also constrained in the UX direction to prevent sideways movement.
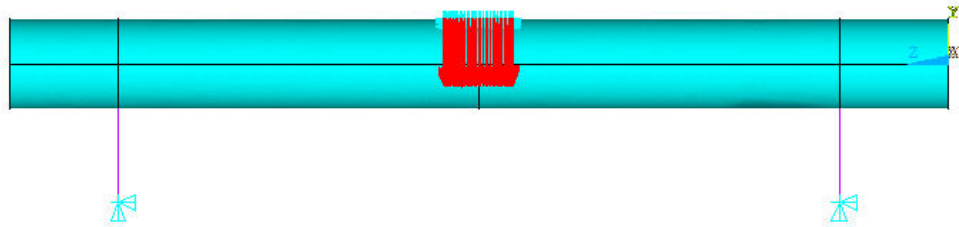
Figure 5-12: Boundary conditions for Model 5

5.2.4   Material Properties

5.2.4.1 Stent

The elastic modulus for the stent in both models was defined as 7.89 MPa as per the calculations from section 5.3.3 below.

5.2.5   Model Convergence

A convergence study was carried out to determine the appropriate number of elements for accurate results. To achieve this, size controls were applied to each of the lines in the model to define the element edge length. Element edge length was changed from iteration to iteration and the results and the number of elements in the model were recorded each time. The model was considered converged when the result stopped changing with the increase in number of elements.

5.3 Results

5.3.1 Mechanical Testing

The physical measurements taken from the 3 stents used in the 3-point-bend test is shown in Table 5-2.

Table 5-2: Measurements of deployed stents used for 3-point-bend test

	Deployment pressure	Length	Outer diameter measured
Stent 1	9 atm	26 mm	2.44 mm
Stent 2	9 atm	26 mm	2.51 mm
Stent 3	9 atm	26 mm	2.42 mm
Mean	9 atm	26 mm	2.46 mm

Force-deflection graphs obtained from the DMA results are shown below in Figure 5-13, Figure 5-14, Figure 5-15 and Figure 5-16. All the data from each of the stents is shown in Figure 5-13. The data is then broken down to look at only the linear section of the graph, which describes the elastic behaviour of the stents before plastic deformation and was necessary for further analysis. These sections of the data for stent 1, stent 2 and stent 3 are depicted in the graphs in Figure 5-14, Figure 5-15 and Figure 5-16 respectively. To allow direct comparison, the data in each of the graphs has been normalised to the origin and a line of best fit added. The equation of the trendline and the R-squared value are shown on each of the graphs.

The raw data for these graphs can be found in Appendix C.
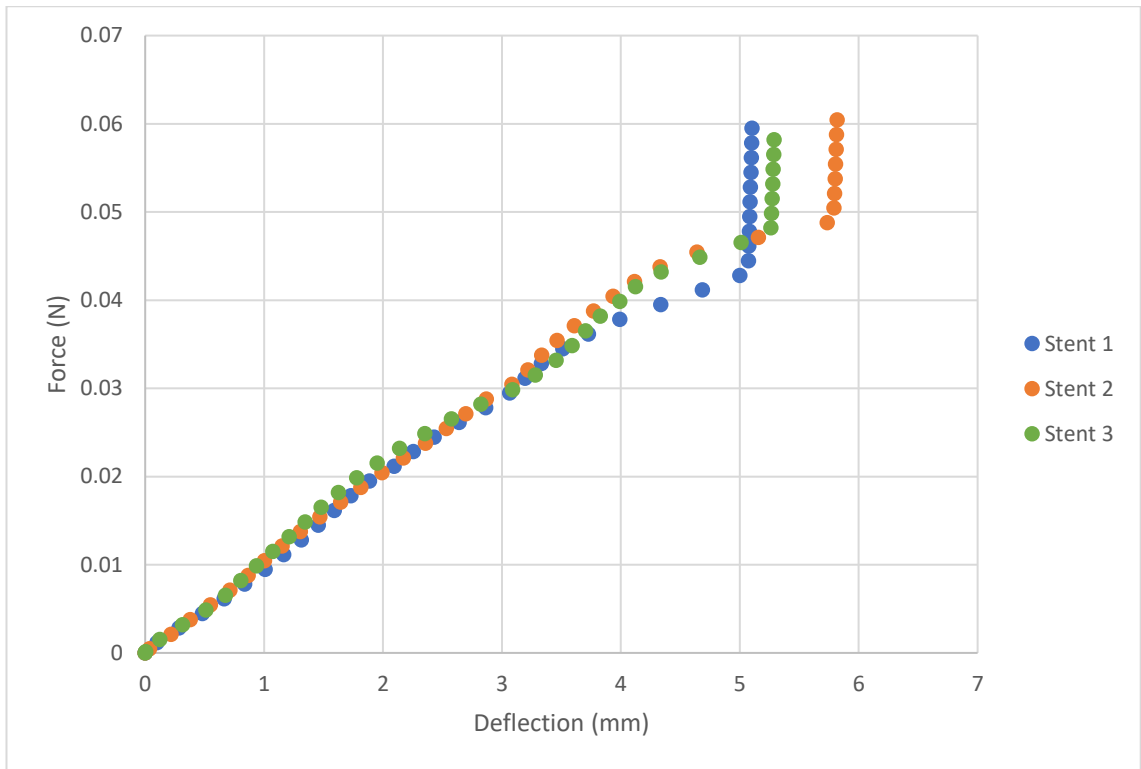
Figure 5-13: Force-deflection graph for Stents 1, 2 and 3
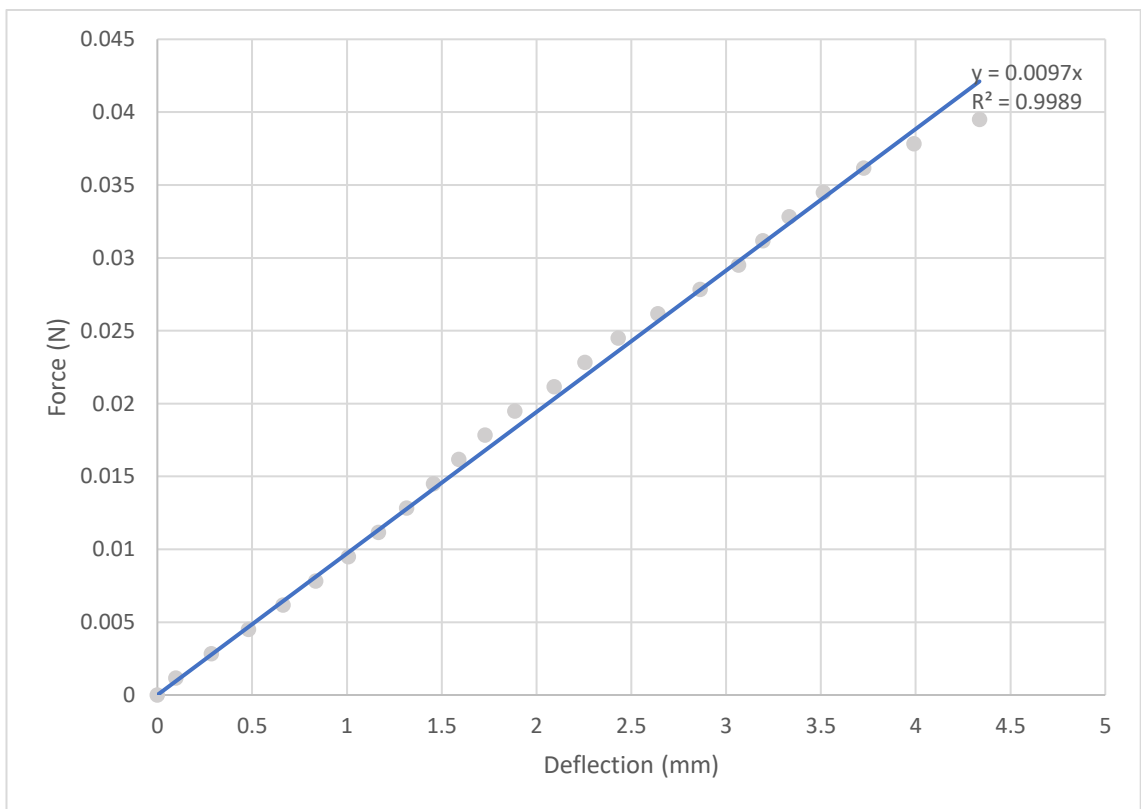
Figure 5-14: Stent 1 force-deflection graph normalised to origin
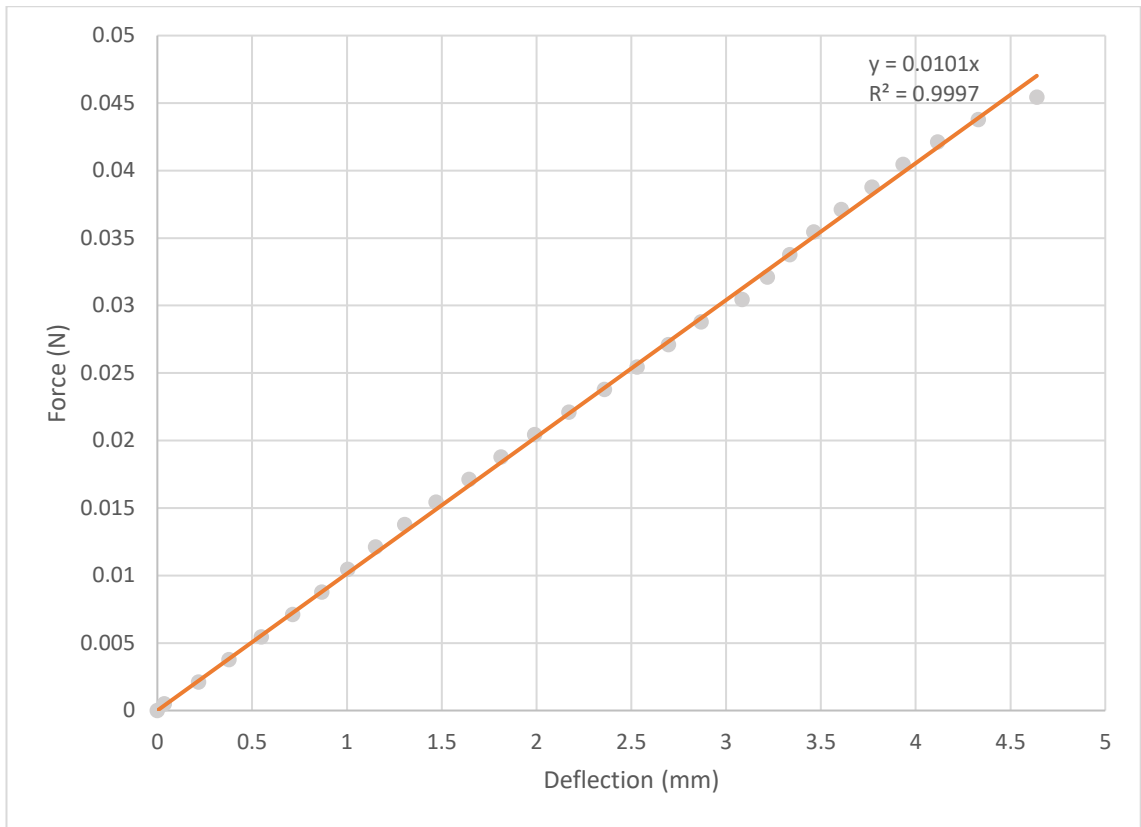
Figure 5-15: Stent 2 force-deflection graph normalised to origin
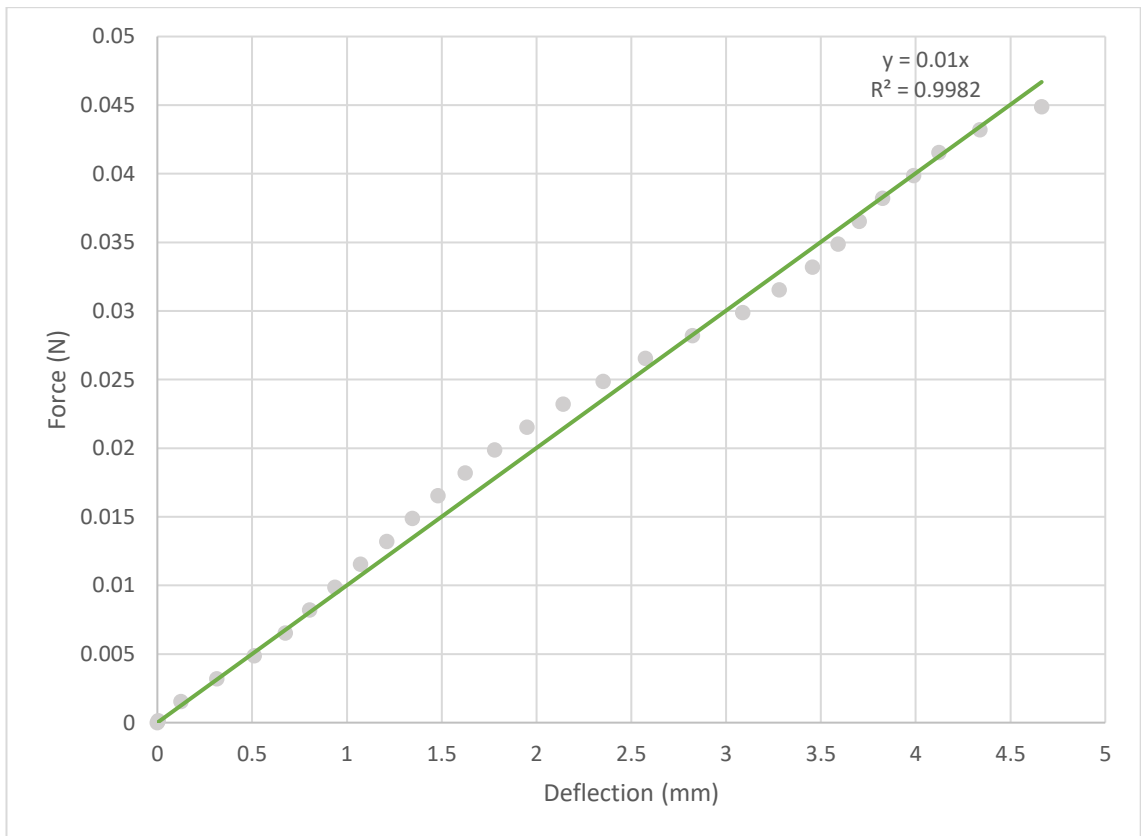
Figure 5-16: Stent 3 force-deflection graph normalised to origin

The gradient of the lines of best fit from the graphs were used to calculate the average expected deflection as shown in Table 5-3. An applied load of 0.04 N was used to fit within the linear elastic section of the force-displacement graphs.

Table 5-3: Deflection of each stent with 0.04 N load applied

	Gradient	Deflection when y=0.04 N
Stent 1	0.0097	4.12 mm
Stent 2	0.0101	3.96 mm
Stent 3	0.0100	4.00 mm
Mean	0.0099	4.03 mm
Standard deviation (SD)	0.00017	6.96 mm
Standard deviation as a percentage of Mean (%)	1.71	1.73

For the purpose of comparing the three data sets, the data points have been compiled into the same graph as show below in Figure 5-17. The R-squared value and equation of the line of best fit are shown on the graph.
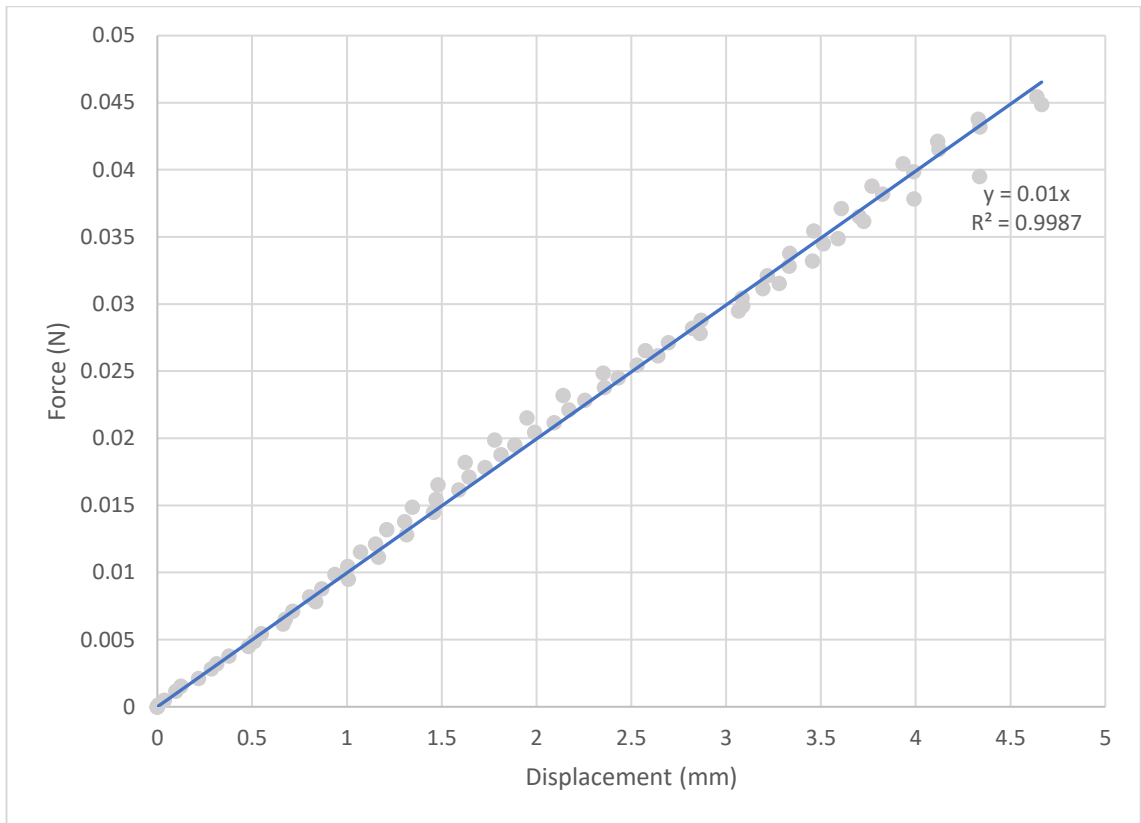
Figure 5-17: Force-deflection data for all three stents

5.3.2 **Effective Modulus Calculation**

From Equation 5-1, the effective modulus was calculated using the following data (Table 5-4) taken from the force-deflection graphs from the DMA testing. Equation 5-2 was used to calculate the second moment of area for the idealised stent.

$$I = \frac{\pi}{4}(r_2{}^4 - r_1{}^4)$$

Equation 5-2

Where r_2 and r_1 are the outer and inner radii of the stent, respectively. The values for r_2 and r_1 are taken from the average outer diameter measurement of 2.46 mm in Table 5-2 and the known strut thickness of 88.9 μm for the Resolute Integrity stent device.

Table 5-4: Values for parameters used to calculate effective stent modulus

Parameter	Symbol	Value
Load applied	P	-0.04 N
Length of stent	L	0.026 m
Deflection	y_1	0.004 m
Second moment of area of idealised stent	I	4.64077E-13 m^4
Stent outer radius	r_2	1.23 mm
Stent inner radius	r_1	1.14 mm

From this the effective modulus was calculated to be 7.89 MPa.

5.3.3   Boundary Conditions

The results of the different models are summarised below in Table 5-5.

Table 5-5: Summary of results from Models 1-5

Model No.	Maximum Deflection	Deflection pattern description
1	4.27 mm deflection	Localised indentation on top of stent
2	2.77 mm deflection	Expected deformation pattern
3	1.20 mm deflection	Localised indentation on top of stent
4	2.58 mm deflection	Localised indentation on top of stent along the line of nodes.
5	2.88 mm deflection	Expected deformation pattern

The deflection patterns for each of the models are shown below.

The results of Model 1 are shown below in Figure 5-18, Figure 5-19 and Figure 5-20.
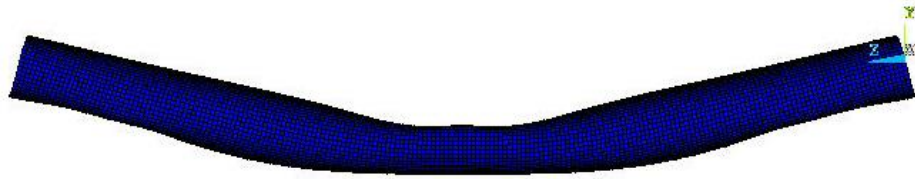
Figure 5-18: Deflection pattern for Model 1
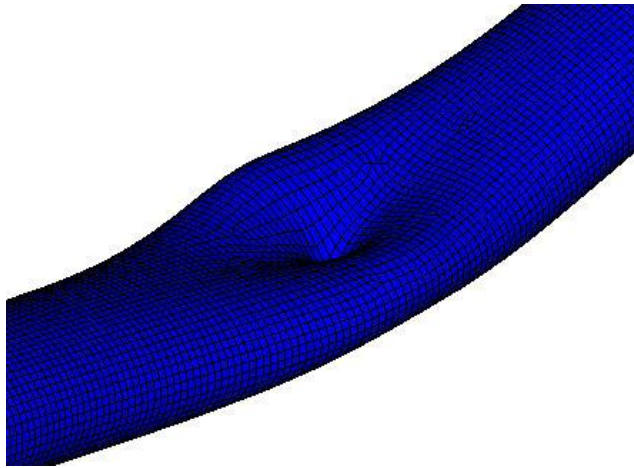
Figure 5-19: Close-up image of deflection pattern for Model 1 at load location
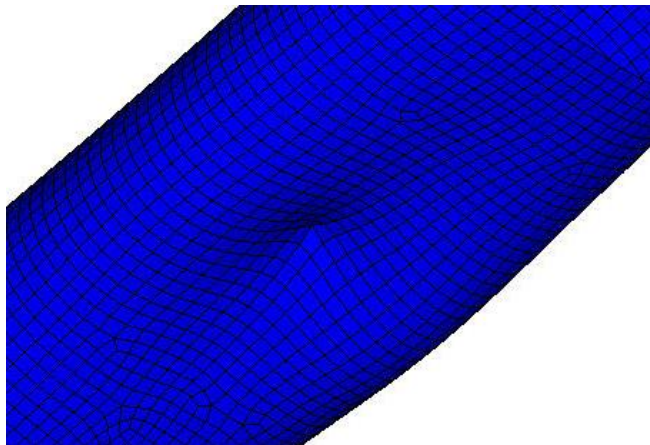
Figure 5-20: Close-up image of deflection pattern for Model 1 at support location

5.2.3.1 Model 2

The results of Model 2 are shown below in Figure 5-21, Figure 5-22 and Figure 5-23.
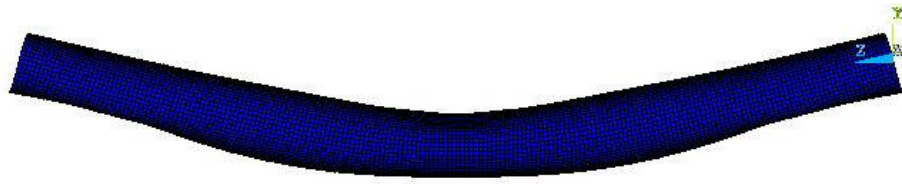
Figure 5-21: Deflection pattern for Model 2
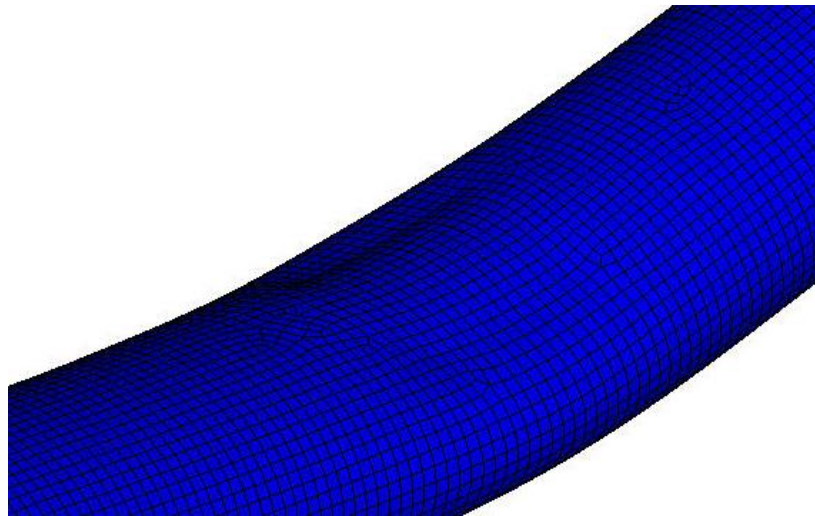
Figure 5-22: Close-up image of deflection pattern for Model 2 at load location
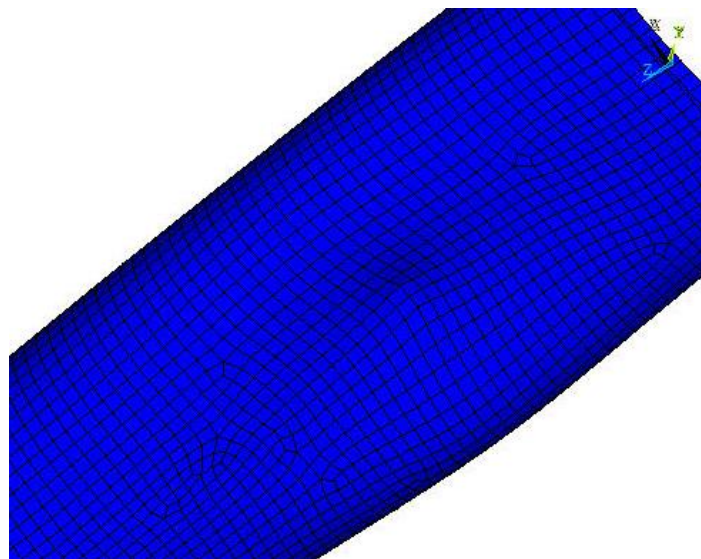
Figure 5-23: Close-up image of deflection pattern for Model 2 at support location

5.2.3.1 Model 3

The results of Model 3 are shown below in Figure 5-24, Figure 5-25 and Figure 5-26
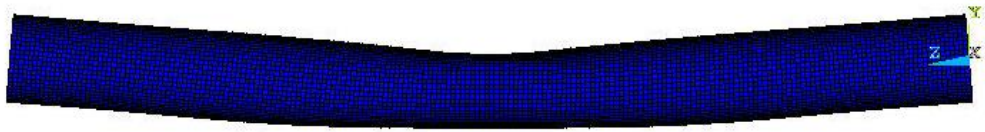
Figure 5-24: Deflection pattern for Model 3
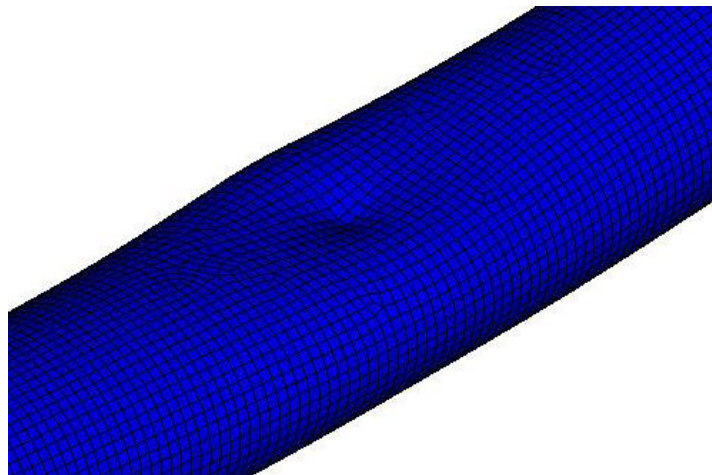
Figure 5-25: Close-up image of deflection pattern for Model 3 at load location
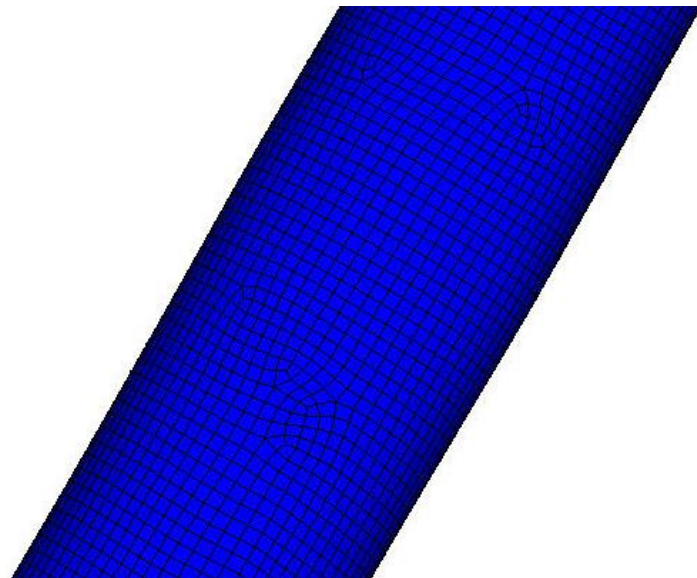
Figure 5-26: Close-up image of deflection pattern for Model 3 at support location

5.2.3.1 Model 4

The results of Model 4 are shown below in Figure 5-27, Figure 5-28 and Figure 5-29
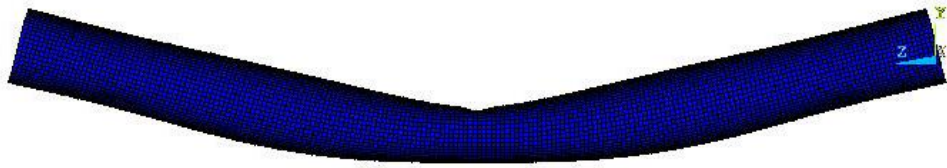
Figure 5-27: Deflection pattern for Model 4
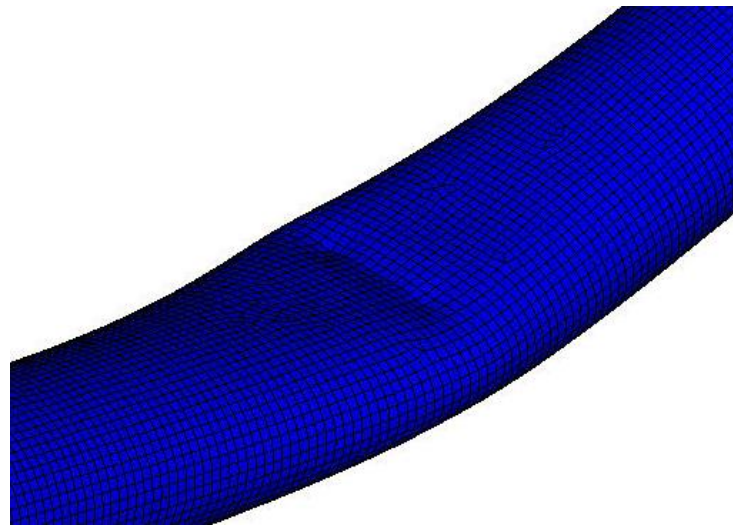
Figure 5-28: Close-up image of deflection pattern for Model 4 at load location
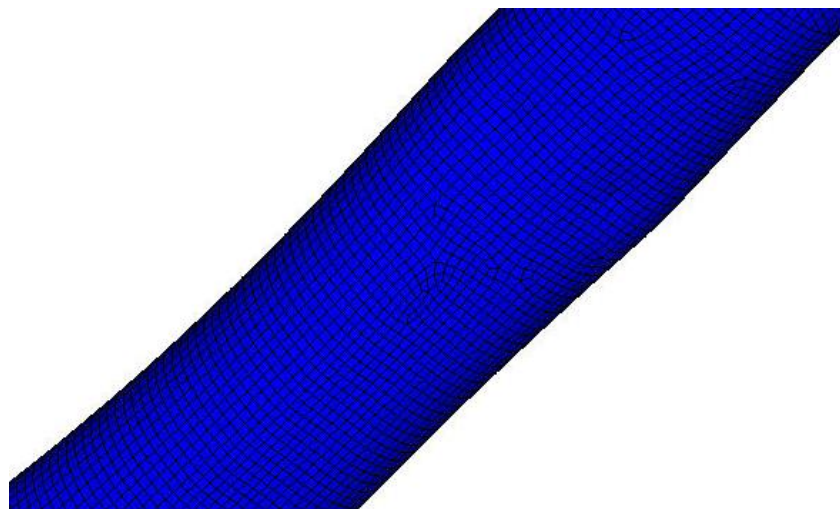
Figure 5-29: Close-up image of deflection pattern for Model 4 at support location

The results of Model 5 are shown below in Figure 5-30, Figure 5-31 and Figure 5-32.
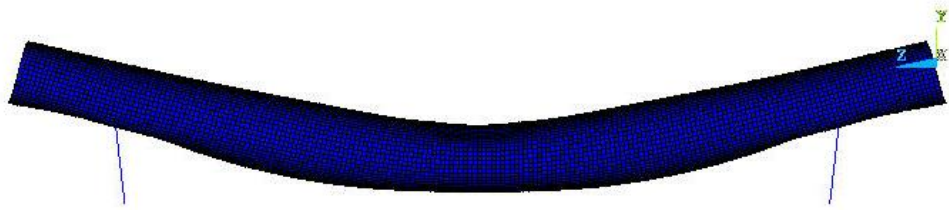
Figure 5-30: Deflection pattern for Model 5
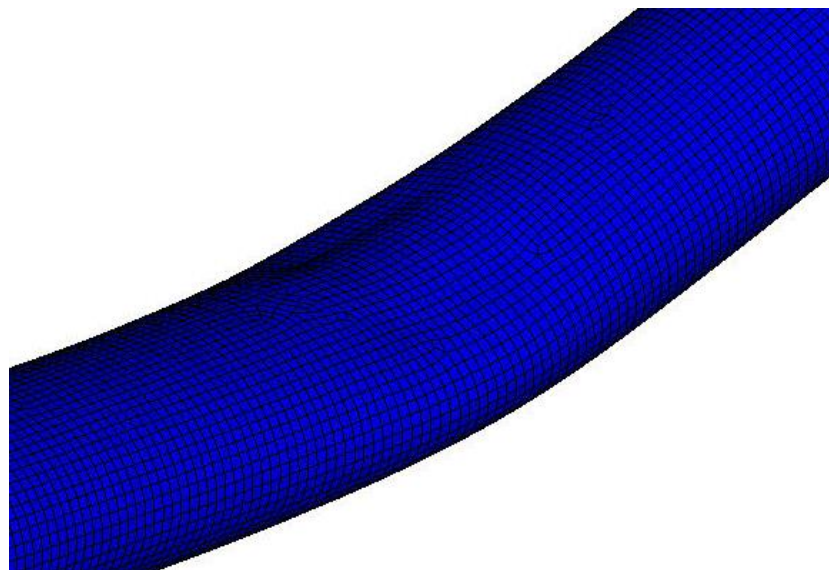
Figure 5-31: Close-up image of deflection pattern for Model 5 at load location
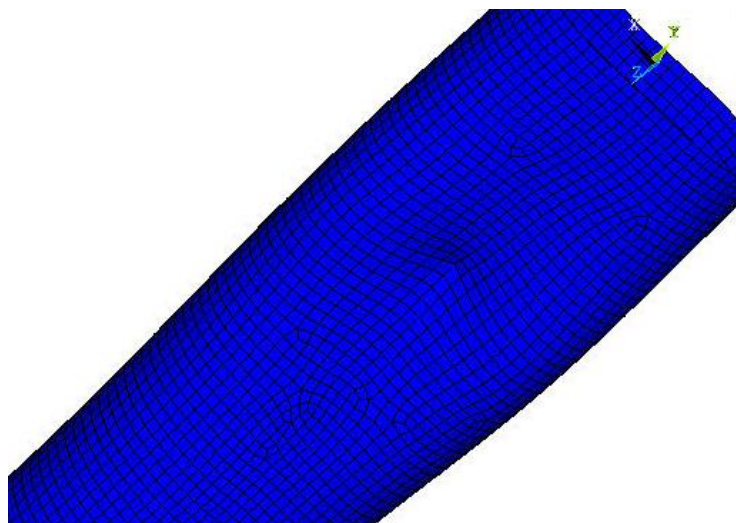
Figure 5-32: Close-up image of deflection pattern for Model 5 at support location

5.3.4 **Model Convergence**

A convergence study was carried out on model 2 to ensure that there were enough elements in the stent mesh to obtain a reliable result. The mesh was refined by incrementally decreasing the element edge length to increase the number of elements in the model. The data from the convergence study are shown in Table 5-6 and Figure 5-33 below. The deflection noted is taken as the maximum displacement in the stent model.

Table 5-6: Convergence study data

Maximum element edge length (m)	No. of elements	Maximum deflection (mm)
0.0004	1320	2.5101
0.00035	1826	2.5695
0.0003	2354	2.6319
0.00026	3311	2.6814
0.00024	3879	2.6917
0.00022	4368	2.6937
0.0002	5324	2.7074
0.00018	6538	2.7147
0.00016	8893	2.7525
0.00015	9248	2.7538
0.00014	10800	2.7666
0.00013	12657	2.7727
0.00012	15819	2.7852
0.00011	18147	2.7884
0.0001	22393	2.8035
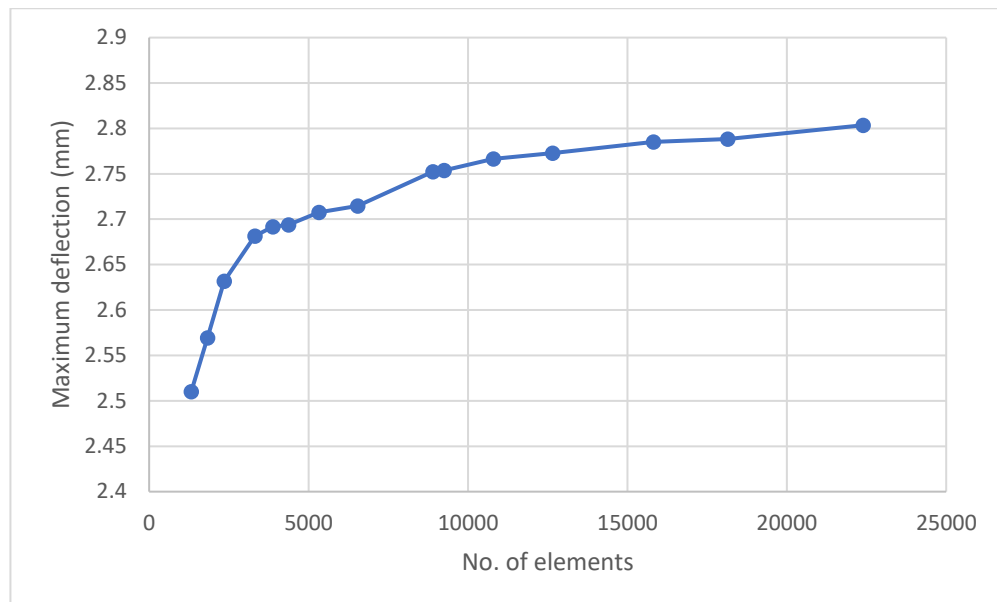
Figure 5-33: Graph of convergence study data

The nodal result is deemed to have converged at the approximately 12000 elements in the stent, which was achieved with a defined maximum element edge length of 0.13 mm. Any modelling going forward, therefore, will be defined with the same element edge length.

5.4 Model Finalisation

Looking at the results from Models 1-5, the target deflection of 4.03 mm from the experimental testing was not obtained. Despite using a number of different boundary condition configurations to attain the most appropriate deflection, the models that provided the expected deflection pattern as per the 3-point-bend test without any highly localised areas of indentation (Models 2 and 5) achieved a deflection of 2.77 mm and 2.88 mm respectively. This is 69% and 71% of the 4.03 mm target deflection for Models 2 and 5 respectively. For this reason, it was decided to adjust the model to fully simulate the behaviour of the stent in the 3-point-bend test. Further explanation on the reason behind this can be found in the Discussion section, section 5.5 below.

5.4.1 Method

The model finalisation involved altering the defined thickness of the shell elements representing the stent strut thickness to ensure that the model was representative of the samples that had undergone mechanical testing.

The maximum deflection was recorded for each of the stent thicknesses, starting at 88.9 μm as per the thickness of the Resolute Integrity struts and decreasing until the correct deflection was observed. As per the mechanical testing, the deflection target deflection from a load of 0.04 N was 4.03 mm. The stent thickness, therefore, was reduced until this target deflection was achieved.

5.4.2 Results

The data from the stent strut thickness alteration is shown in Table 5-7 and Figure 5-34 below.

As can be seen from the graph, the stent with the closest deflection value to the target 4.03 mm is that with a thickness of 70.6 μm.

Table 5-7: Data from stent thickness alteration

Stent thickness (µm)	Maximum deflection (mm)
88.9	2.7727
80.0	3.2770
75.0	3.6431
71.0	3.9951
70.7	4.0240
70.6	4.0338
70.5	4.0435
70.0	4.0931
65.0	4.6566
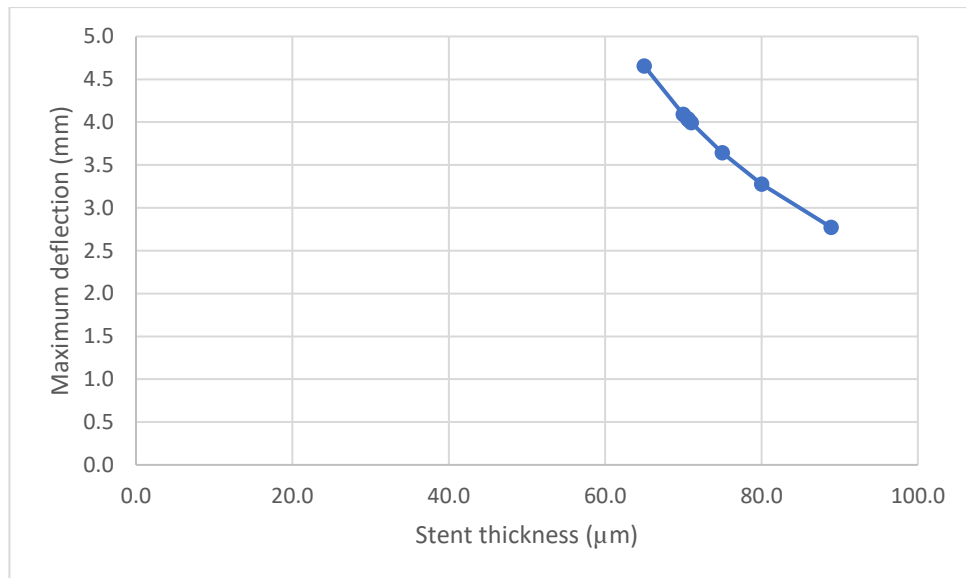
Figure 5-34: Graph of stent thickness data

5.5 Discussion

5.5.1 Mechanical Testing

When taking measurements for the diameter of the stent after expansion, there is a level of inherent inaccuracy due to the flexibility of the device. The stent was fragile and easily deformed so although every care was taken to enable the most accurate measurement possible, the Vernier calliper used was required to be adjusted manually

to the size of the stent thus there will be an element of human error involved. The measurements for all 3 devices tested, however, were taken by the same person thus eliminating any measurement errors associated with measurements being taken by different people. Also, the Vernier calliper was calibrated to zero in the closed position before measurements were taken so that the results would be as accurate as possible, however the device was only accurate to 2 decimal places thus there is an associated error of ±0.005 mm. As the stents were over 2.4 mm, this equates to an error of 0.2% and was deemed acceptable.

The stents were all deployed to 0.2mm greater than nominal. Whilst the deployment pressure used was that suggested in the deployment instructions, there was no resistance of the artery when deploying, which may account for the larger diameter of the deployed stent. The stent inflation device was also a manual device, which means that there is room for error due to human measurement error.

There will also always be infinitesimal variations in the 3-point-bend test of stents due to the intricacies of their structures. There is great variation in the design at various locations along the device's length and circumference and therefore it will never be possible to position a second device on the test rig in exactly the same rotational and axial location as a previously tested device. This is an inherent error, however, that is impossible to eliminate.

Several attempts were made in the initial 3-point-bend tests to ensure a reasonable load was being applied to the device. The test was initially carried out with too much load, which resulted in a crushed stent (Figure 5-35). This meant that the methods initially needed some fine-tuning and resulted in several lost stents. There were therefore fewer samples available when an appropriate loading had been ascertained. Results were
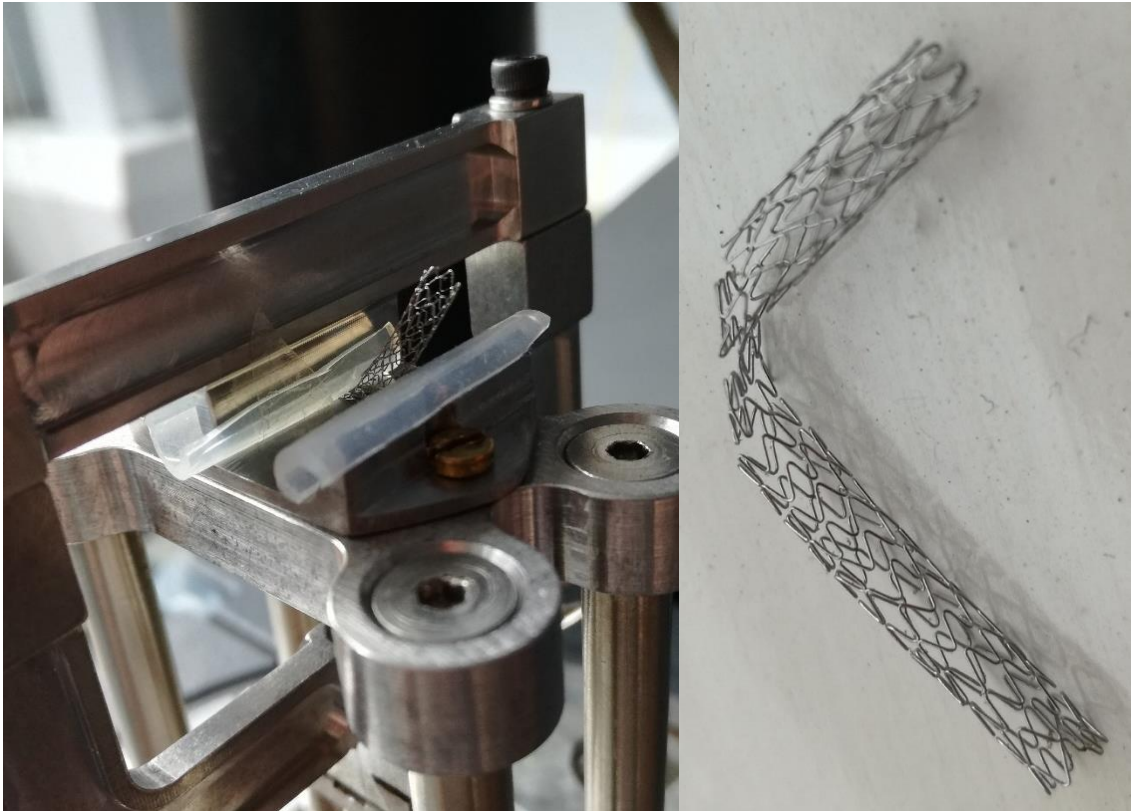
Figure 5-35: Image of crushed stent from first DMA test

available therefore from only 3 stents, which means that there is a relatively small pool of data from which to draw conclusions.

Despite there being only 3 data samples, the results were very similar throughout the datasets. The R-squared value is above 0.99 for the data from each of the stents (Figure 5-14, Figure 5-15 and Figure 5-16), suggesting that the lines of best fit are accurate enough to draw conclusions from. The R-squared value when all of the data was combined was 0.9987 (Figure 5-17), which suggests that the test was reliable and repeatable. The standard deviation for the deflection was only 1.73%, which also suggests that the data is repeatable. The R-squared value also validates the error associated with axial and circumferential positioning on the DMA test rig mentioned above and shows that this is negligible.

5.5.2 Effective Modulus Calculation

Several assumptions were made when calculating the elastic modulus for the idealised stent. Firstly, some of the physical parameters used in the calculation were taken as per manufacturing specifications and were not confirmed using measurements in the lab. This included the thickness of the stent struts for the calculation of the second moment of area, and the length of the devices. This means the values may not exactly represent the true measurements from the stent samples tested but the equation used in the calculation would be relatively insensitive to the negligible discrepancies. Also, manufacturing tolerances are presumed to be tight due to the nature of the device, thus the stent strut thickness manufacturing specification is expected to be reliable.
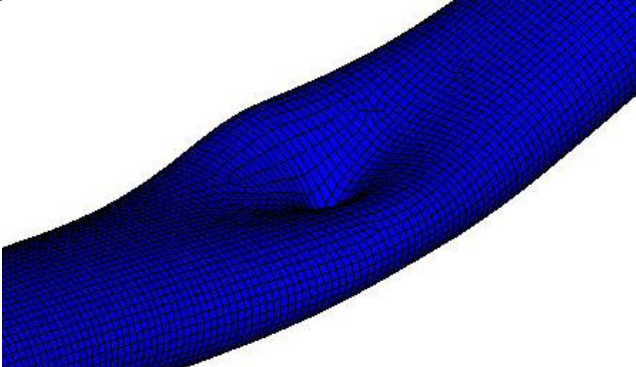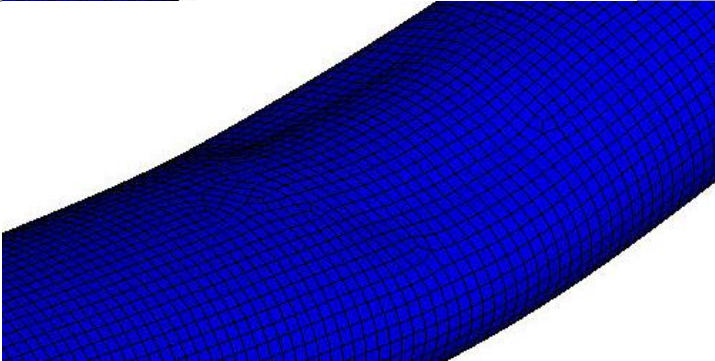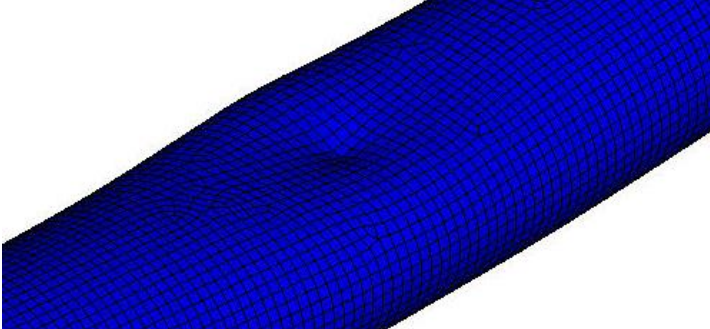
The modulus was also based on the force-displacement relationship of the 3 samples. The results used were an average of the 3 samples, which was the most accurate way of using the data, however if more stents had been available it would have been preferable to have a larger sample size. Despite this, the R-squared value of the data from all three force-displacement graphs was above 0.99 so the test is repeatable and reliable.

5.5.3 Model Generation

It is clear from the deflection plots of the models that there was a variation in the results from the different boundary conditions. The models that had single or 3 node loads resulted in highly localised indentations on the top of the stent. The models with the largest indentations were Model 1 and Model 3, as can be seen in Table 5-8. Model 4 also had a localised indentation from the load, however it was not as severe due to the more distributed area over which the load was applied. This is due to the low stiffness of the idealised model and the small area over which the loads were applied.

The deflection plots for Models 2 and 5, however, were much more as expected from the mechanical testing (Table 5-8). Calculating the load area using Hertzian theory was a more realistic way of applying the load. Having the load distributed over 588 nodes meant that there were no localised areas of high levels of deflection and the stent behaved much more as expected from the experimental testing.

Table 5-8: Summary of deflection plots a load location for Models 1 to 5

Model No.	Deflection plot at load location
1	
2	
3	

4	
5	
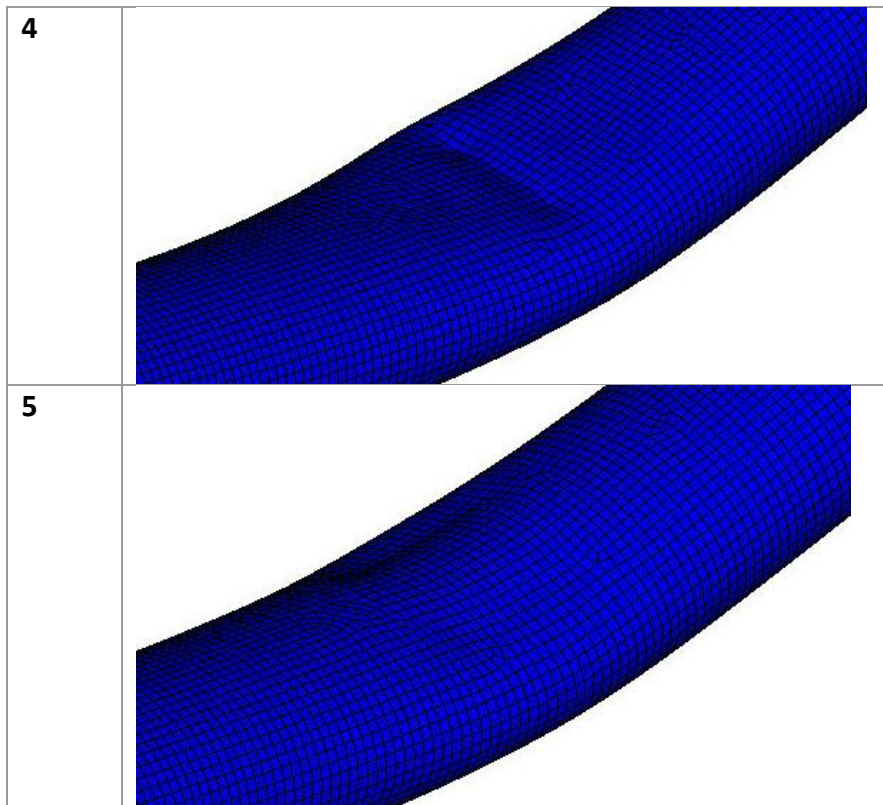
Although using a calculated contact area over which to apply the load allowed for a more realistic representation of the contact from the load applicator in the 3-point-bend test, the load was distributed evenly over the entire area. This meant that it did not allow for any variation in the distribution of the load applied within the area. In reality, more of the load may have passed through the centre of the cylindrical load applicator than the edges, which may have produced a slightly different deflection pattern.

The boundary conditions that represented the supports in the 3-point-bend test also resulted in localised indentations, although not to the same extent as the load. As can be seen in The maximum deflection observed in each of the models ranged from 1.2 mm to 4.27 mm (Table 5-5 in section 5.3.3). This variation was caused by the variety of BCs in the models. As has been discussed, highly localised deflection at the load and supports locations have been observed in most of the models. It was decided that the models with a single node, 3 nodes and a line of nodes for the load (Models 1, 3 and 4) were

unsuitable representations as the load was not distributed enough and caused a deflection pattern that was not as expected from the mechanical testing.

Models 2 and 5, however, were both more representative of the mechanical testing due to the more distributed load. Model 5 utilised a rigid link element to simulate the radius of the supports used in the 3-point-bend test. The rigid link element, however, was connected to a single node on the base of the stent. This caused a larger indentation than the 3 nodes used to represent the supports for Model 2.

Overall, the model chosen to be most representative of the mechanical testing was Model 2 as the deflection pattern was as expected from the testing. The supports being distributed over three nodes was more realistic than the single node support. As the maximum deflection observed in Model 2 was 2.77 mm and that in Model 5 was 2.88 mm, which is 69% and 71% of the target 4.03 mm respectively, it was decided that the difference in the maximum deflection between the two models is insignificant.

Table 5-9, Models 1 and 5 result in a more localised deflection point due to the single nodes that were constrained to represent the supports. The rigid link supports used in Model 5, which were attached to a single node at the support locations behaved in the same way as that of the single load support. Model 2 is not dissimilar, although the deflection is not as great at the support location as there were 3 nodes over which constraints were applied, thus the load was more distributed.
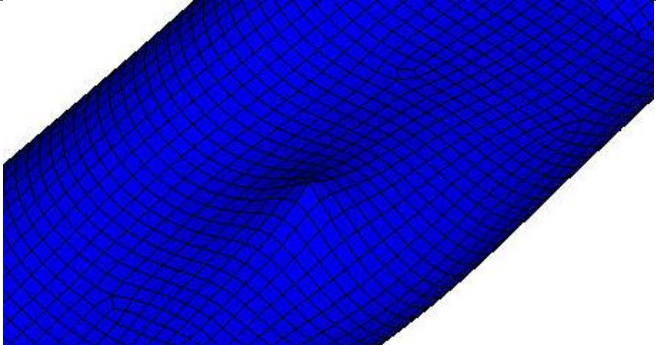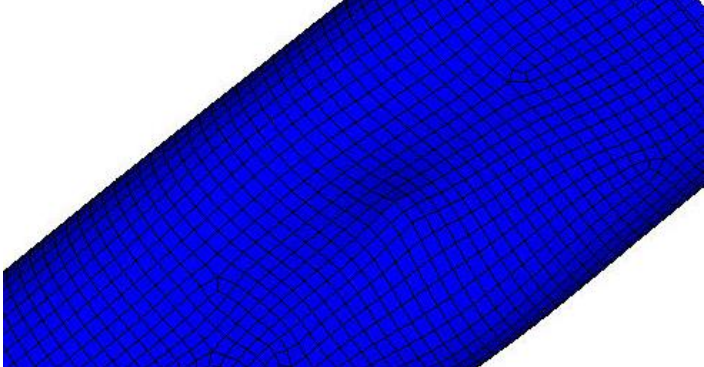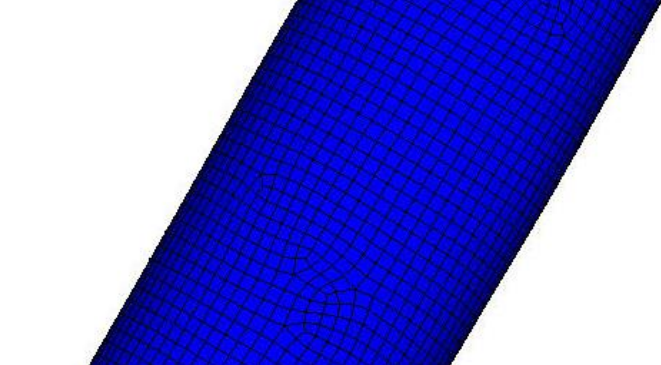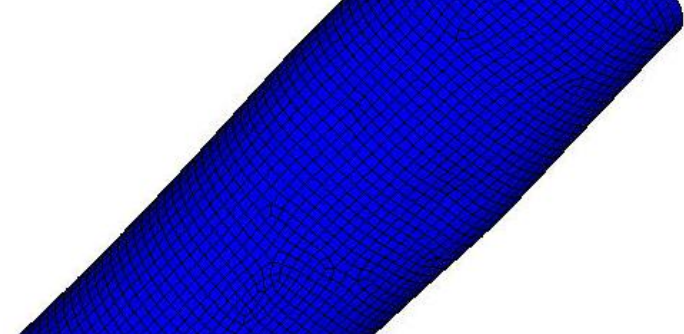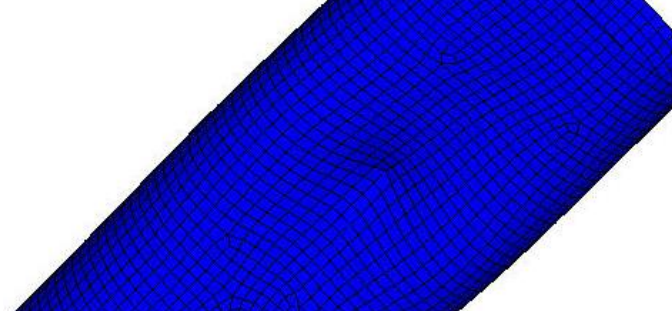
Models 3 and 4 provided the deflection patterns with the smallest localised deflection at the support locations due to the more distributed support area. For both models, the supports were represented by a single line of nodes parallel to the X axis, on which degree-of-freedom constraints were applied in the UY and UX directions. This meant that the load was distributed over the 25 nodes for each support, but the movement of the stent was much more restricted resulting in a smaller maximum deflection.

The maximum deflection observed in each of the models ranged from 1.2 mm to 4.27 mm (Table 5-5 in section 5.3.3). This variation was caused by the variety of BCs in the models. As has been discussed, highly localised deflection at the load and supports locations have been observed in most of the models. It was decided that the models with a single node, 3 nodes and a line of nodes for the load (Models 1, 3 and 4) were unsuitable representations as the load was not distributed enough and caused a deflection pattern that was not as expected from the mechanical testing.

Models 2 and 5, however, were both more representative of the mechanical testing due to the more distributed load. Model 5 utilised a rigid link element to simulate the radius of the supports used in the 3-point-bend test. The rigid link element, however, was connected to a single node on the base of the stent. This caused a larger indentation than the 3 nodes used to represent the supports for Model 2.

Overall, the model chosen to be most representative of the mechanical testing was Model 2 as the deflection pattern was as expected from the testing. The supports being distributed over three nodes was more realistic than the single node support. As the maximum deflection observed in Model 2 was 2.77 mm and that in Model 5 was 2.88 mm, which is 69% and 71% of the target 4.03 mm respectively, it was decided that the difference in the maximum deflection between the two models is insignificant.

Table 5-9: Summary of deflection plots a support location for Models 1 to 5

Model No.	Deflection plot at load location
1	
2	
3	
4	
5	
	Deflection plot at load location

5.5.4 **Model Finalisation**

Although the stent in Model 2 was deforming as expected from the mechanical testing, the deflection was below the target of 4.03 mm observed in the 3-point-bend test.

One of the assumptions made when generating the model was the second moment of area of the stent, on which the idealised model is based. The effective modulus calculation used for the idealised stent required the second moment of area of the device (Equation 5-2, page 68). It is not possible to calculate a second moment of area for a stent, which is effectively a tubular mesh. For this reason the stent was idealised to a tube for the purpose of this calculation, as in the idealised model being generated. The inner and outer radii of the cylinder was based on the strut thickness of the stent.

As the strut thickness was not measured for the stents undergoing mechanical testing, the strut thickness used was taken from the Resolute Integrity "Instructions for Use" document as 88.9 μm (Medtronic, 2013). This meant that there was a margin for error due to manufacturing discrepancies and the devices tested may not have had the same strut thickness. The high R-squared value of the experimental testing, however, suggests that the thickness was consistent amongst these three stents. In addition, it is possible that the thickness of the struts would have had some variation along the length of the stent, although as previously discusses, the nature of the device would suggest that manufacturing tolerances are tight, which means that the manufacturing specification is expected to be reliable.

Furthermore, the cross-section of the stent struts was also not known. The effective modulus calculation was based on the second moment of area of the stent. As the second moment of area was calculated based on the strut thickness, it was assumed that the strut thickness given in the "Instructions for Use" document (Medtronic, 2013)

was the thickness in the radial direction. The possibility remains, however, that the thickness given was that in the tangential direction, in which case the radial thickness was unknown. In addition, it is assumed that the struts cross-section is rectangular or square, which may also not be the case. This also provides a margin for error and may mean that the calculated second moment of area was not accurate.

The assumptions stated may explain the difference between the maximum deflection observed and the FE simulation of the mechanical testing.

As this idealised model will be used for analysis in further chapters, the main aim of this idealised model generation was to create a model that was representative of the mechanical testing carried out. This means that the model was not required to be an accurate version of a stent, simply to reliably represent the stent 3-point-bend test undertaken.

To ensure the model was representative of the stents that had undergone mechanical testing, it was decided to adjust the parameters to obtain the correct deformation for the load applied. It was decided that the most appropriate parameter to adjust was the thickness of the stent struts. To achieve this, the thickness of the shell elements defining the stent was altered incrementally until the model exhibited the appropriate level of deformation.

As can be seen in the results of the stent strut thickness alteration, the stent achieved the expected level of deformation at a strut thickness of 70.6 μm. This was a 21% decrease in stent strut thickness.

Once the stent strut thickness had been adjusted, the model was as representative as possible of the mechanical testing undertaken. This meant that further idealised

modelling could be reliable based on the model generated with an elastic modulus of 7.89 MPa and a stent strut thickness of 70.6 µm.

5.6 **Conclusions**

The model created in this chapter is independent of any individual artifacts in the stents and eliminates effects of the complex geometry. This means that the results of any FE analysis will show a larger picture of the expected locations of the areas of higher stress and thus the most likely location for potential stent strut fracture. This does not account for any localised points of likely SF that arise from design intricacies such as joins between cells and bridges.

The FE model is representative of the stent that underwent mechanical testing and appears to behave appropriately when under the same loading and support conditions as the sample did in the DMA machine. This means that it is an accurate model for its intended use in future chapters.

Although this model cannot be used for analysis of other specific stents, the method is easily repeatable and can be used for any type of stent.

6 Idealised Modelling Sensitivity Study

6.1 Introduction

The aim of this chapter is to study the sensitivity of an idealised stent model to the modelling methods of the arterial structure. In order to assess the stresses undergone by stents *in vivo* the idealised stent will be modelled using FE analysis in its surrounding vessel. It is expected that the likelihood of SF can be predicted using the data from this analysis, as well as the likely locations on the stent where fracture would be expected to occur.

SF is known to be more prevalent in angulated vessels such as bifurcations, where the angle between the main vessel and the side branch can range from 15° to 120° (Chaichana et al., 2011). This study, therefore, will focus on a vessel with initial angle of 105°. Throughout the cardiac cycle, the artery also undergoes cyclical hinge-motion bending. As the impact of the bending of the vessel puts further stress on the stents, this study will assess the effect of a 20° displacement on the already angulated vessel.

To represent the *in vivo* environment as accurately as possible, it was necessary to include the coronary artery in the simulated environment. There are, however, a wealth of material models available in literature for this purpose (Holzapfel et al., 2000; Prendergast et al., 2003; Lally et al., 2005; Chua et al., 2004; Liang et al., 2005; Pericevic et al., 2009; Martin and Boyle, 2013; Gastaldi et al., 2010; Zahedmanesh and Lally, 2009).

Despite the wealth of data currently available pertaining to the material properties of human arteries, there has been little comparative work to qualify the necessity of using the ever-more complicated constitutive models. Whilst it is vital in the study of vessel wall stresses to model arterial tissue with as much accuracy as possible, the nature of

this study having its focus on the stresses in the stent means that the sensitivity of stent stresses to the exact nature of the vessel needs to be ascertained. The purpose of this study is to assess the depth of detail required in the artery model to carry out the FE analysis of stent stresses.

6.2 Materials and Methods

6.2.1 Model Development

The 3-dimensional geometry of the stent and artery was created using FE analysis software ANSYS Mechanical APDL (ANSYS 14.5 Mechanical, ANSYS, Inc., Canonsburg, PA, USA). The model was produced in the Cartesian coordinate system with an arterial segment surrounding the device.

Initially, a series of lines were created to define the centreline of the model. This defined the length of the artery segment, which included the length of the stent and a 2.5 mm overhang at either end, and the angle and radius of curvature of the vessel. Annuli were then created at the location of the top of the arterial segment to represent the arterial layers, using the initial line as a guide. The line was then used as a sweep path over which the annuli could be used to create volumes.

Two models were created; one with one arterial layer, and anoth with that aterial later split into 3 separate volumes.

Once the geometry had been created, the stent could be defined as shell elements on the area of the inner surface of the volume. A cross-section of the completed geometries can be seen in Figure 6-1 and Figure 6-2 below, with the artery shown in turquoise and the stent in purple.
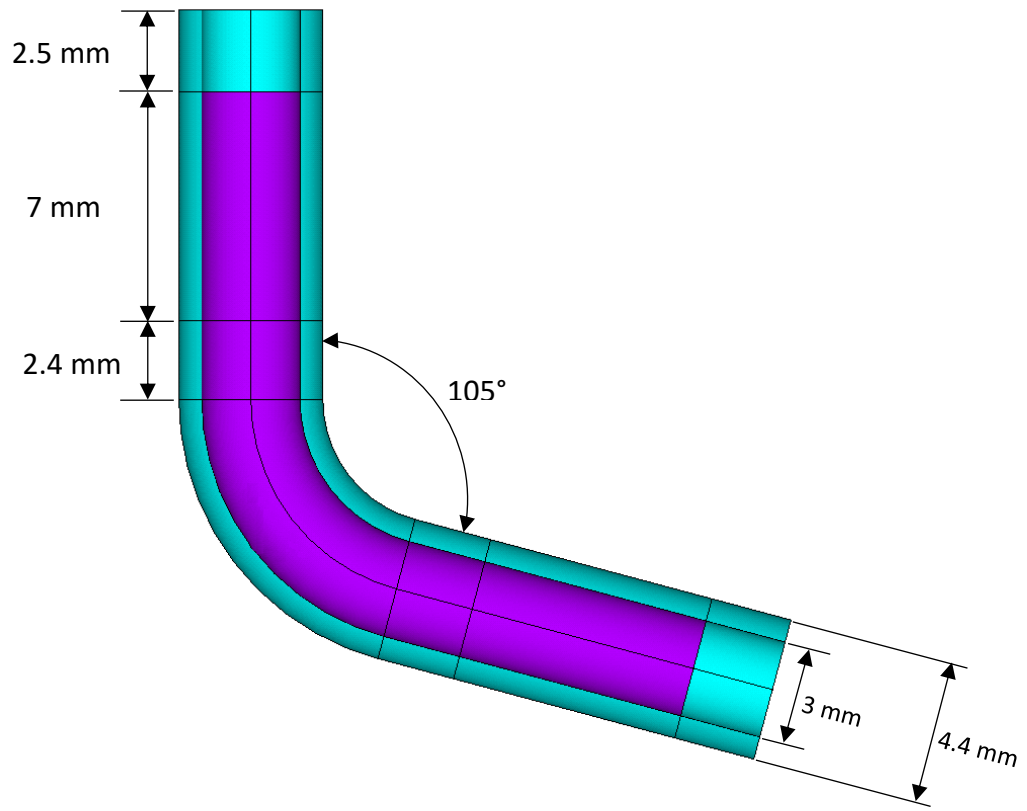
Figure 6-1: 1 layer idealised model geometry
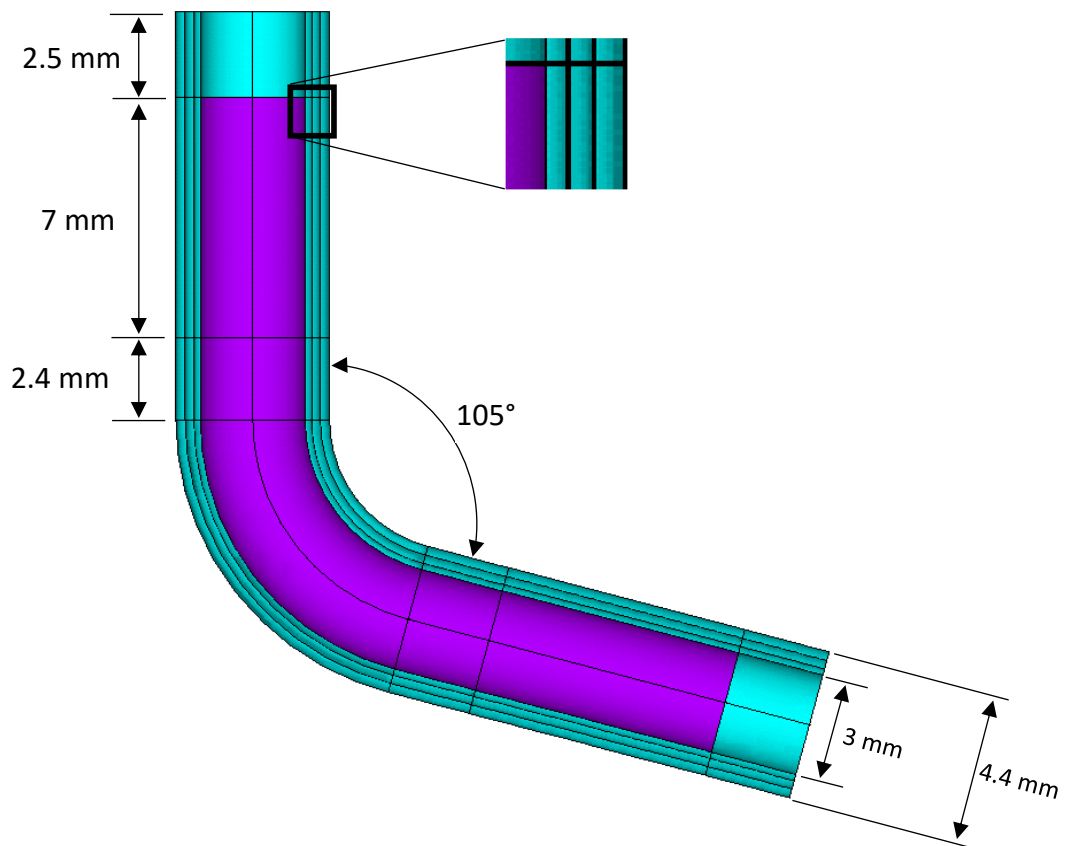
Figure 6-2: 3 layer idealised model geometry

6.2.2 **Material Properties**

6.2.2.1 Stent

As described in section 5, an effective modulus was calculated to validate the use of an idealised cylindrical stent and to account for the lack of mesh-like structure in this model. This was calculated using a bending stiffness test and was defined to be 7.89 MPa. The models, therefore, were defined with a stent elastic modulus, E, of 7.89 MPa and a Poisson's ratio, v, of 0.3. The shell elements were defined with a thickness of 0.0706 mm as also established in section 5.

6.2.2.2 Artery

The surrounding vessel was defined by a number of material models found in literature. Six material models in total were represented, one linear and 5 non-linear hyperelastic. Of the hyperelastic models, 4 represented tissue properties outlined in the literature. The other is a hyperelastic model representing silicone, which is commonly used in *in vitro* stent testing. The material models used, the type of model, the material it represents and the reference source are summarised in Table 6-1 below.

Table 6-1: Material models used in artery model sensitivity study

Model	No. of arterial layers	Mathematical model	Material	Reference
A	1	Linear	Artery	Chua et al., 2004
B	1	Mooney-Rivlin (eq. 1)	Artery	Lally et al., 2005
C	1	Mooney-Rivlin (eq. 1)	Artery	Pericevic et al., 2009
D	1	Mooney-Rivlin (eq. 1)	Silicone	Conti, 2010
E	3	Ogden (eq. 2)	Artery	Martin and Boyle., 2013
F	3	Ogden (eq. 2)	Artery	Zahedmanesh and Lally, 2009

Model A

The first of the models is a linear representation of arterial tissue as described by Chua et al. (2004), based on experimental work carried out by Veress et al. (2000). The artery was defined with a Young's modulus, E, of 0.00175 GPa and a Poisson's ratio, v, of 0.499.

Model B

The vessel in Model B was defined by a third-order Mooney-Rivlin hyperelastic constitutive equation (Equation 6-1);

$$W(I_1, I_2, I_3) = \sum_{i,j,k=0}^{\infty} a_{ijk} \, (I_1 - 3)^m (I_2 - 3)^n (I_3 - 3)^0 \qquad \textbf{Equation 6-1}$$

$$a_{000} = 0$$

where W is the general form of the strain-energy density function, a_{ijk} are the hyperelastic constants that can be calculated experimentally and I_1, I_2 and I_3 are the strain invariants defined as (Equations 6-2 to 6-4);

$$I_1 = \lambda_1{}^2 + \lambda_2{}^2 + \lambda_3{}^2 \qquad \textbf{Equation 6-2}$$

$$I_2 = \lambda_1{}^2\lambda_2{}^2 + \lambda_2{}^2\lambda_3{}^2 + \lambda_1{}^2\lambda_3{}^2 \qquad \textbf{Equation 6-3}$$

$$I_3 = \lambda_1{}^2\lambda_2{}^2\lambda_3{}^2 \qquad \textbf{Equation 6-4}$$

where λ are the principal stretches. The incompressible nature of arterial tissue was determined by Carew et al. (1968) and as $I_3 = 1$ for an incompressible material, the second principal stretch can be written as;

$$I_2 = \frac{1}{\lambda_1{}^2} + \frac{1}{\lambda_2{}^2} + \frac{1}{\lambda_3{}^2} \qquad \textbf{Equation 6-5}$$

For the purposes of modelling arterial tissue, a third-order reduced form of the strain-energy density function was used (Equation 6-6);

$$W = a_{10}(I_1 - 3) + a_{01}(I_2 - 3) + a_{20}(I_3 - 3)^2 + a_{11}(I_1 - 3)(I_2 - 3)$$

<div align="right">**Equation 6-6**</div>

The model parameters for Model B were calculated experimentally by Prendergast et al. (2003) and used in FE analysis by Lally et al. (2005) and shown in Table 6-2.

Table 6-2: Material constants for the artery in Model B (Prendergast et al., 2003; Lally et al., 2005)

Parameter	Arterial wall tissue (kPa)
a_{10}	18.90
a_{01}	2.75
a_{20}	590.43
a_{11}	85.72
a_{30}	0

Model C

The material model used in Model C was also based on the Mooney-Rivlin hyperelastic constitutive equation as shown in equation 3 above. The parameters were used by Pericevic et al. (2009) and shown in Table 6-3 below.

Table 6-3: Material constants for the artery in Model C (Pericevic et al., 2009)

Parameter	Arterial wall tissue (kPa)
a_{10}	708.146
a_{01}	-620.042
a_{20}	2827.33
a_{11}	0
a_{30}	0

Model D

To account for the use of silicone mock arteries often used in stent testing (Pelton et al., 2008), a silicone model (Model D) was included in this study. This model was also based on the Mooney-Rivlin hyperelastic constitutive equation shown in equation 3 and parameters are those used by Conti (2010), shown in Table 6-4.

Table 6-4: Material constants for the artery in Model D (Conti 2010)

Parameter	Arterial wall tissue (kPa)
a_{10}	-2403.01
a_{01}	3023.54
a_{20}	456.29
a_{11}	-1728.92
a_{30}	2735.98

Model E

The material properties for Model E are described by a third-order Ogden isotropic hyperelastic material model represented by Equation 6-7:

$$\Psi = \sum_{i=1}^{N} \frac{2\mu_i}{\alpha_i^2} \left(\bar{\lambda}_1^{\alpha_i} + \bar{\lambda}_2^{\alpha_i} + \bar{\lambda}_3^{\alpha_i} - 3 \right) + \sum_{i=1}^{N} \frac{1}{D_i} (J-1)^{2i} \qquad \textbf{Equation 6-7}$$

where μ_i, α_i and D are the hyperelastic constants that can be calculated experimentally. The material constants for Model E were obtained from the mechanical testing of circumferentially loaded tension tests carried out by Holzapfel et al. (2005) and used by Martin and Boyle. (2013). The parameters used in the model are shown in Table 6-5 below.

Table 6-5: Material constants for the artery in Model E (Martin and Boyle., 2013)

Parameter	Intima	Media	Adventitia
μ_1 (kPa)	-5700.00	-1840.00	-1990.00
μ_2 (kPa)	3580.00	1120.00	1200.00
μ_3 (kPa)	2170.00	730.00	810.00
α_1	24.43	21.71	24.61
α_2	25	22	25
α_3	23.24	21.2	23.9
D_1	0.85	4.11	3.92

Model F

The final material model used in this sensitivity study was taken from Zahedmanesh and

Lally (2009). Similarly to Model E, the parameters were also taken from mechanical tests

carried out by Holzapfel et al. (2005). The parameters are shown in Table 6-6 below.

Table 6-6: Material constants for the artery in Model F (Zahedmanesh and Lally, 2009)

Parameter	Intima	Media	Adventitia
μ_1 (kPa)	-7037.59	-1231.14	-1276.31
μ_2 (kPa)	4228.84	785.12	846.41
μ_3 (kPa)	2853.77	453.62	438.51
α_1	24.48	16.59	24.63
α_2	25	16.65	25
α_3	23.54	16.5	23.74
D_1	0.000000895	0.00000531	0.00000467

6.3 Boundary Conditions

Once meshed, the loading and constraints were applied to the nodes. To simulate the

hinge motion throughout the cardiac cycle, a displacement was applied to a selection of

nodes on the outer surface of the vessel at either end (Figure 6-4). The displacement

was calculated using a rotation matrix, thus enabling the hinge motion to be accurately represented with a relative 10° rotation of the model from each end. To calculate the displacements, the nodal coordinates of each node to be displaced were exported from ANSYS into Microsoft Excel (Microsoft Corp., WA, USA). The rotation matrix was then applied to each of the X and Y locations of every node to calculate the appropriate new coordinates. The difference in each X and Y coordinate was then calculated in order to apply displacement is both axial directions to each of the approriate nodes. A schematic to show the X, Y and Z directions for the models can be found in Figure 6-3.
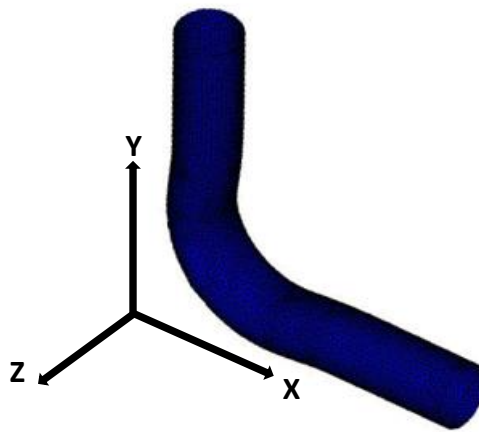
Figure 6-3: Schematic to show X, Y and Z directions for all models

Three nodes on the outer surface of the artery were constrained in all degrees of freedom at the hinge-point of the vessel to allow for an appropriately constrained model.

The boundary conditions (BCs) can be seen in Figure 6-4 below.
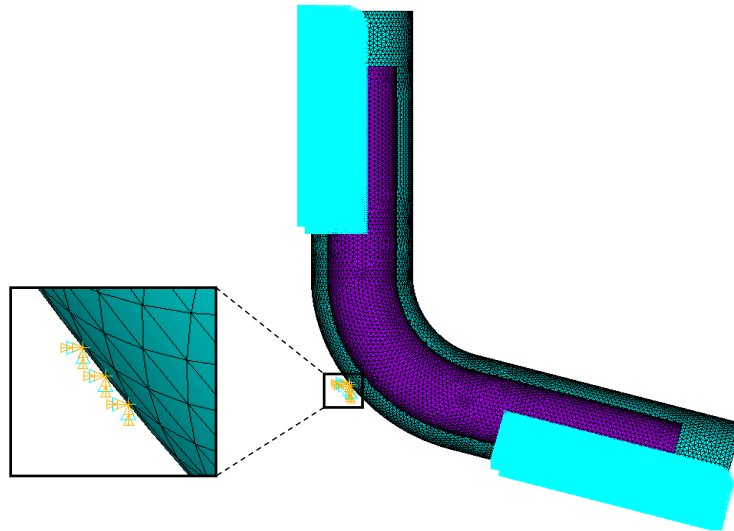
Figure 6-4: Discretised artery with boundary conditions

6.4 **Model Convergence**

A convergence study was carried out to ensure that the mesh was sufficiently refined to provide a reliable result. The mesh was originally created by defining a maximum element edge length along all the lines that make up the model. This meant that the mesh would be uniform across the whole model and that it could easily be altered to change the total number of elements.

The model was defined with a variety of maximum element edge lengths which ranged from 0.32 mm to 0.14 mm. Each iteration required new BCs to be applied, including finding the appropriate locations for degree-of-freedom constraints

The results from each model were recorded to determine the point at which the result was consistent and there were the appropriate number of elements in the models.

6.5 Results

6.5.2 Convergence

The convergence study was carried out by altering the defined element edge length for the mesh from 0.32 mm until the von Mises stress results of each model had converged. The displacement applied was calculated for each model as described in section 6.3 and was the same 10° each side for each iteration. The constraints applied were also the same for each model as described in section 6.3. The material models used were as described in section 6.2.2 and summarised in Table 6-1.

6.5.2.2 Model A

Table 6-7 shows the data from the convergence study of Model A. A graph of this data is shown in Figure 6-5.

Table 6-7: Data from convergence study of Model A

Maximum element edge length (m)	No. of elements	Maximum von Mises stress (MPa)
0.00032	5626	0.87033
0.00028	7154	0.86766
0.00025	8844	0.87087
0.00022	10990	0.86578
0.0002	13136	0.86358
0.00018	17190	0.86380
0.00016	20550	0.86276
0.00014	26888	0.86165
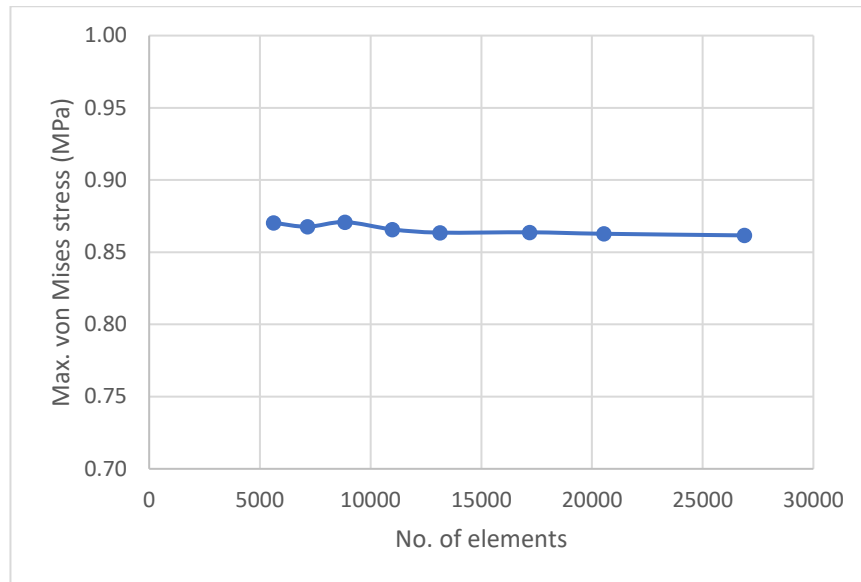
Figure 6-5: Graph of data from convergence study of Model A

6.5.2.3 Model B

Table 6-8 shows the data from the convergence study of Model B. A graph of this data

is shown in Figure 6-6.

Table 6-8: Data from convergence study of Model B

Maximum element edge length (m)	No. of elements	Maximum von Mises stress (MPa)
0.00032	5626	0.54122
0.00028	7154	0.53608
0.00025	8844	0.54238
0.00022	10990	0.53528
0.0002	13136	0.53888
0.00018	17190	0.53659
0.00016	20550	0.52824
0.00014	26888	0.53806
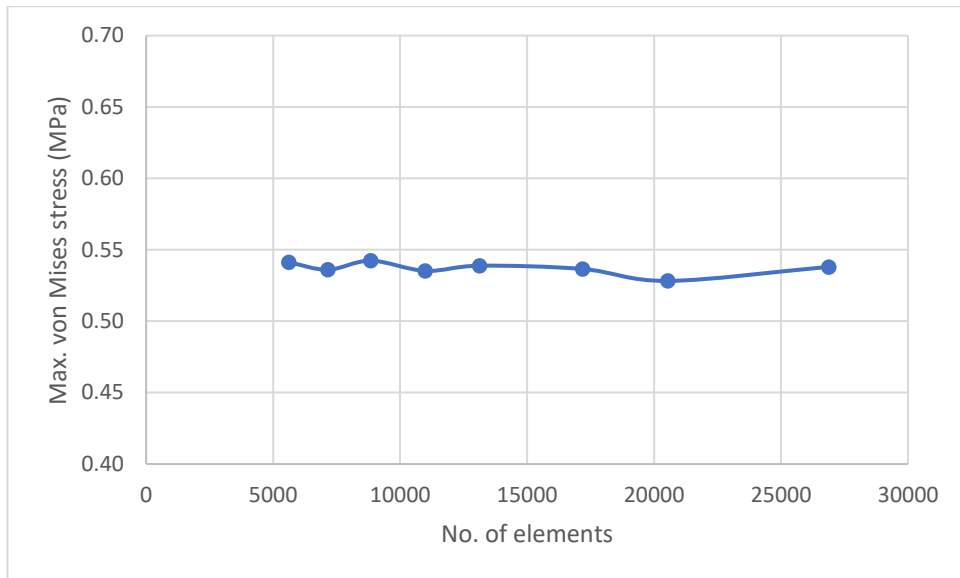
Figure 6-6: Graph of data from convergence study of Model B

6.5.2.4 Model C

Table 6-9 shows the data from the convergence study of Model C. A graph of this data is shown in Figure 6-7.

Table 6-9: Data from convergence study of Model C

Maximum element edge length (m)	No. of elements	Maximum von Mises stress (MPa)
0.00032	5626	0.72444
0.00028	7154	0.72309
0.00025	8844	0.72351
0.00022	10990	0.72353
0.0002	13136	0.72943
0.00018	17190	0.73157
0.00016	20550	0.72537
0.00014	26888	0.72557
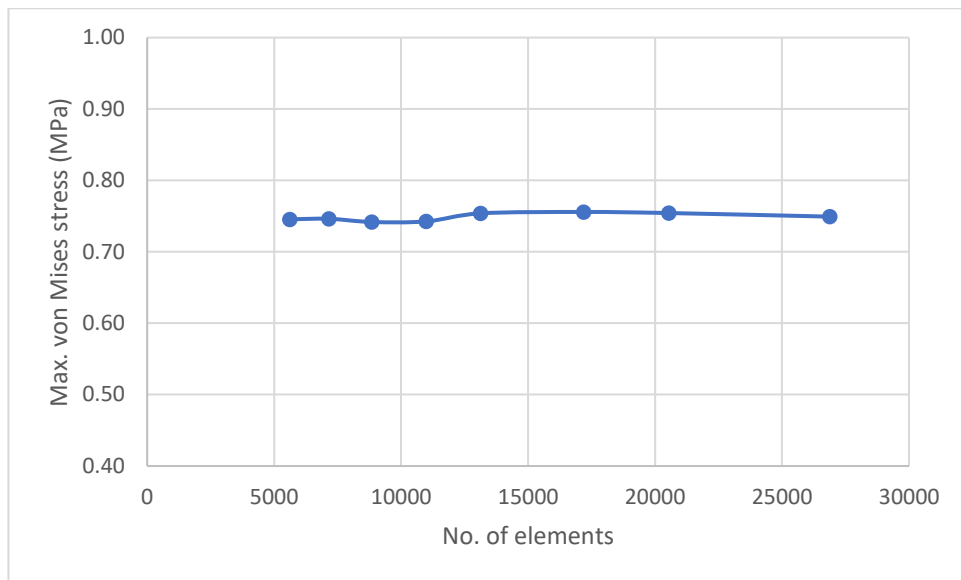
Figure 6-7: Graph of data from convergence study of Model C

6.5.2.5 Model D

Table 6-10 shows the data from the convergence study of Model D. A graph of this data

is shown in Figure 6-8.

Table 6-10: Data from convergence study of Model D

Maximum element edge length (m)	No. of elements	Maximum von Mises stress (MPa)
0.00032	5626	0.90361
0.00028	7154	0.90725
0.00025	8844	0.93287
0.00022	10990	0.94425
0.0002	13136	0.91258
0.00018	17190	0.90245
0.00016	20550	0.90826
0.00014	26888	0.90129
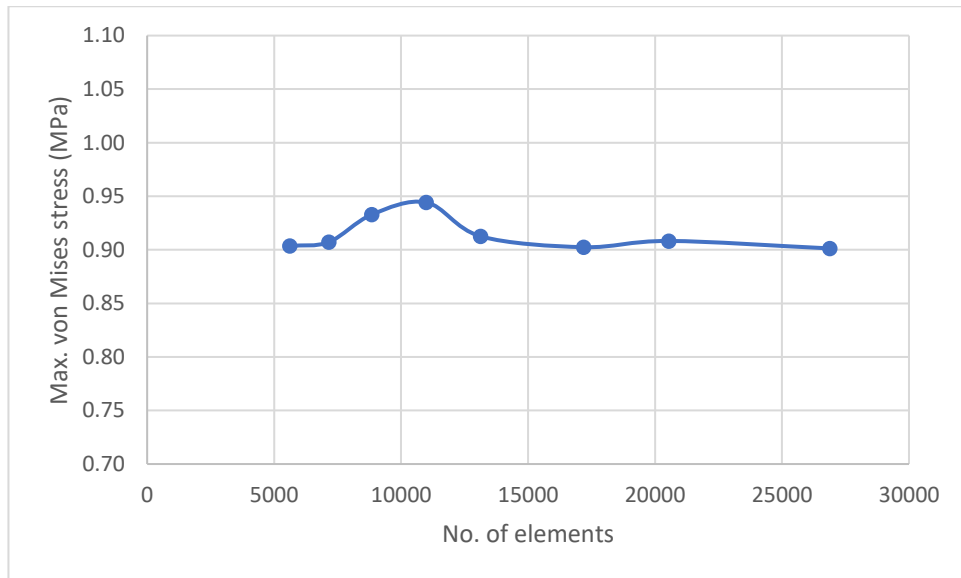
Figure 6-8: Graph of data from convergence study of Model D

6.5.2.6 Model E

Table 6-11 shows the data from the convergence study of model D. A graph of this data

is shown in Figure 6-9.

Table 6-11: Data from convergence study of Model E

Maximum element edge length (m)	No. of elements	Maximum von Mises stress (MPa)
0.00032	5626	0.60022
0.00028	7154	0.61011
0.00025	8844	0.61465
0.00022	10990	0.61914
0.0002	13136	0.61950
0.00018	17190	0.61812
0.00016	20550	0.61488
0.00014	26888	0.61645
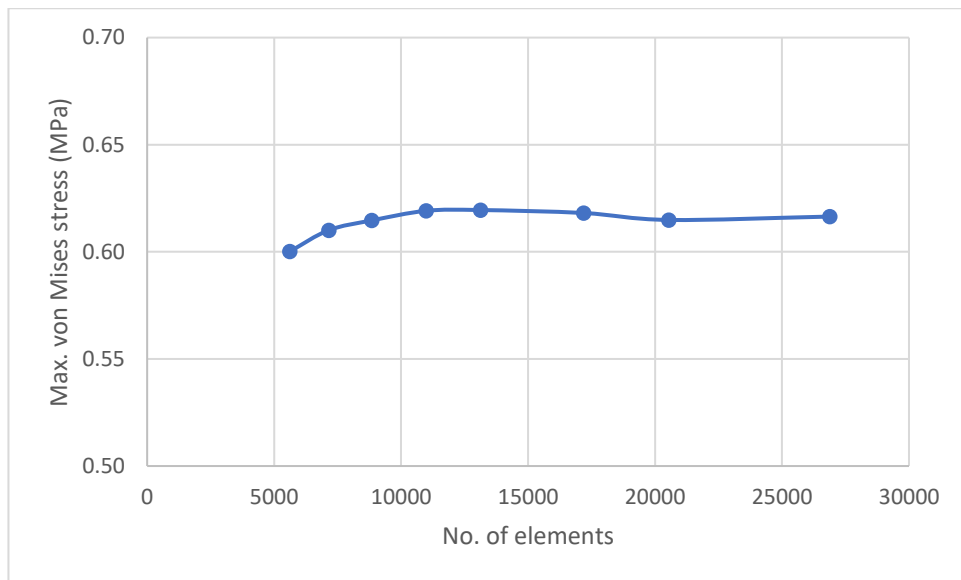
Figure 6-9: Graph of data from convergence study of Model E

6.5.2.7 Model F

Table 6-12 shows the data from the convergence study of Model F. A graph of this data

is shown in Figure 6-10.

Table 6-12: Data from convergence study of model F

Maximum element edge length (m)	No. of elements	Maximum von Mises stress (MPa)
0.00032	5626	0.49821
0.00028	7154	0.50079
0.00025	8844	0.50122
0.00022	10990	0.50571
0.0002	13136	0.50017
0.00018	17190	0.50205
0.00016	20550	0.50272
0.00014	26888	0.50432
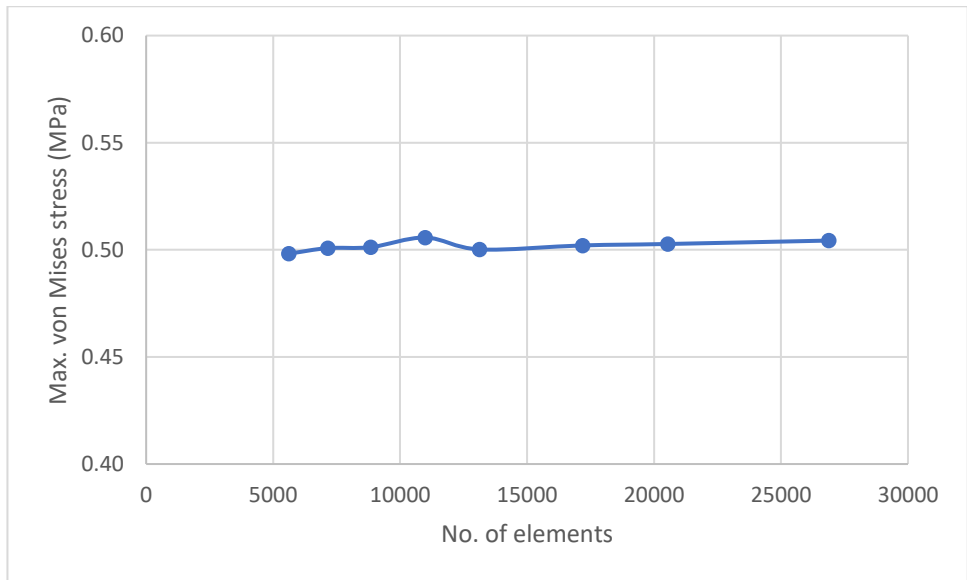
Figure 6-10: Graph of data from convergence study of Model F

6.5.2.8 Finite Element Models

The results of the FE analysis of Models A to F are shown below in Table 6-13 and Figure 6-11. The statistical analysis of these results is summarised in Table 6-14.

Table 6-13: Results from the FE analysis of Models A to F

Model	Maximum von Mises (MPa)	Maximum 1st Principal Stress (MPa)	Minimum 3rd Principal Stress (MPa)
A	0.8636	0.3808	-0.7790
B	0.5389	0.2932	-0.5243
C	0.7294	0.4427	-0.6509
D	0.9126	0.5533	-1.051
E	0.6195	0.3693	-0.7171
F	0.5002	0.2647	-0.5520
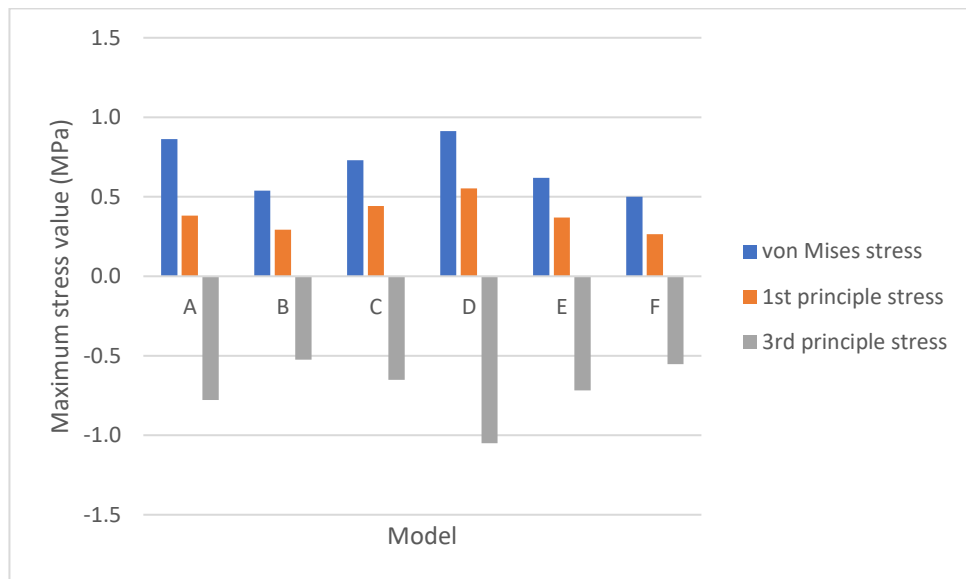
Figure 6-11: Graph to show results from the FE analysis of Models A to F

Table 6-14: Results from statistical analysis of Models A to F

	Maximum von Mises	Maximum 1st Principal Stress	Minimum 3rd Principal Stress
Mean (MPa)	0.6940	0.3840	-0.7124
Standard deviation (SD) (MPa)	0.1554	0.1047	0.1918
SD as a percentage of Mean (%)	22.40	27.27	26.93

The deflection in the Z direction, towards the sides of the stent, is shown below for Models A to F in Table 6-15.

Table 6-15: Data to show maximum deflection of Models A to F in the Z direction

Model	Maximum deflection in Z direction (mm)
A	0.1735
B	0.2821
C	0.2082
D	0.2277
E	0.2915
F	0.2913

Contour plots from the stress analysis of Models A to F are shown below in Figure 6-12, Figure 6-13, Figure 6-14, Figure 6-15 and Figure 6-17.
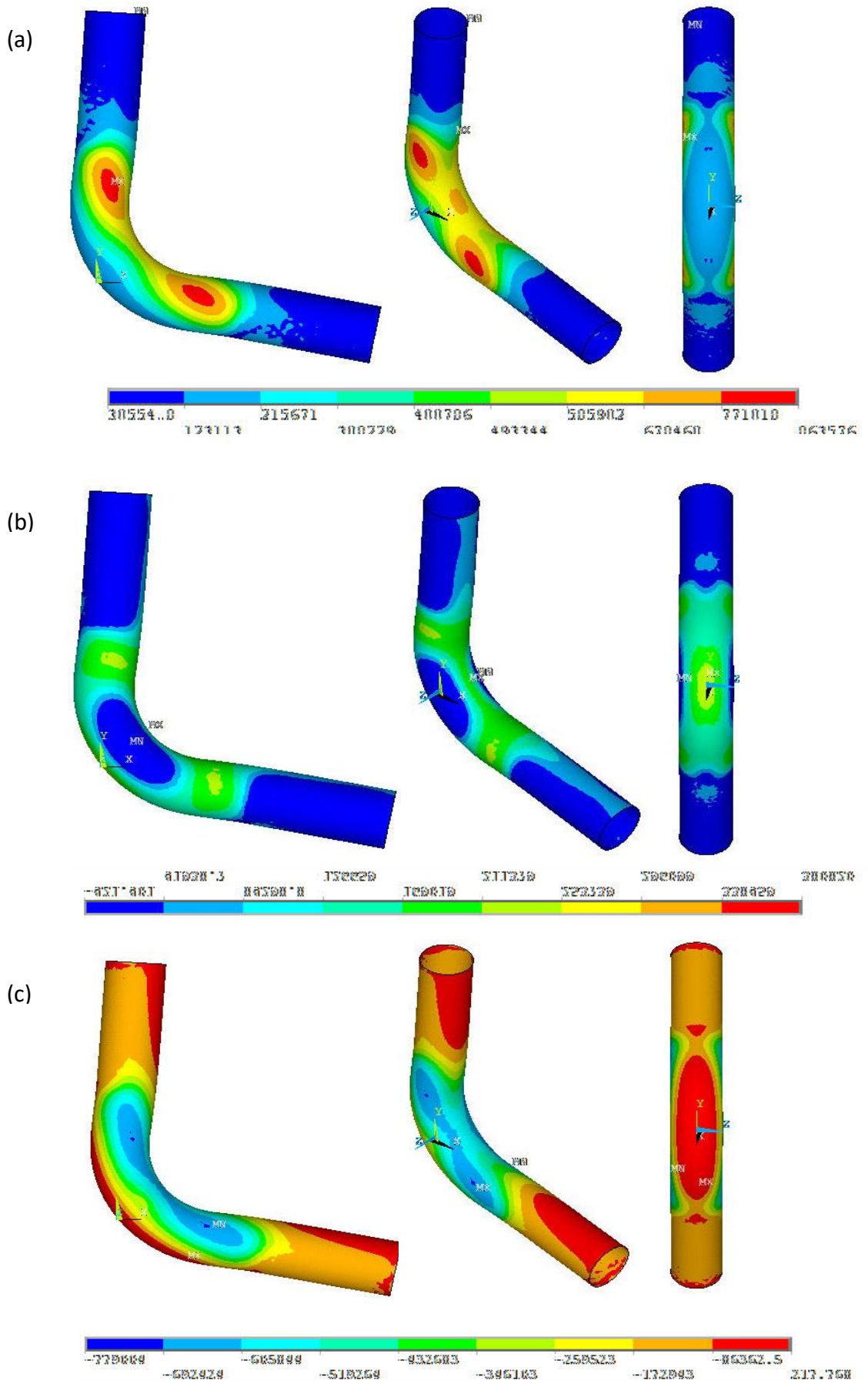
Figure 6-12: Model A side view, isometric view and back view of stress distribution in the stent: (a) von mises, (b) tensile and (c) compressive

(a)

(b)

(c)
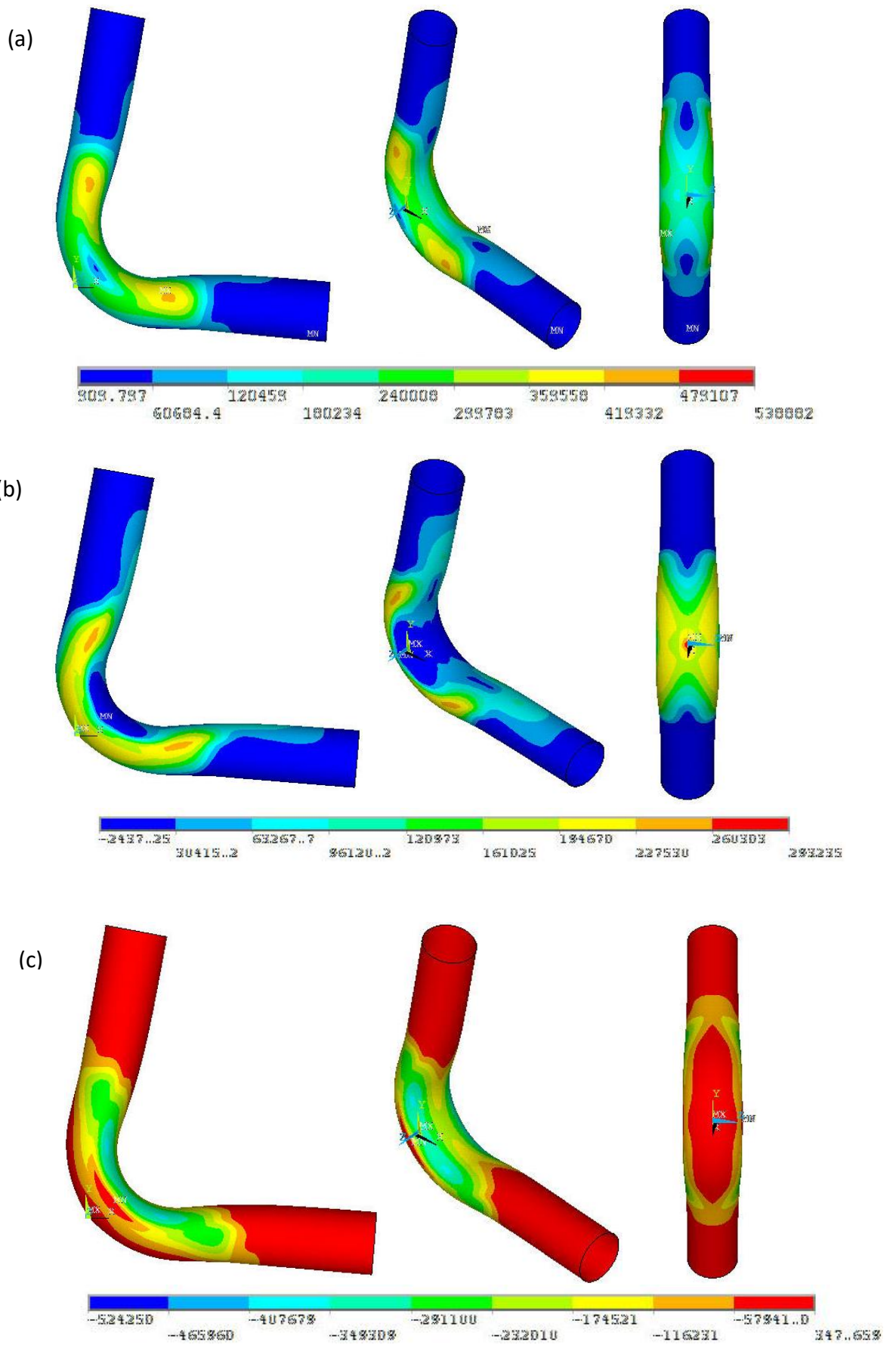
Figure 6-13: Model B side view, isometric view and back view of stress distribution in the stent: (a) von mises, (b) tensile and (c) compressive
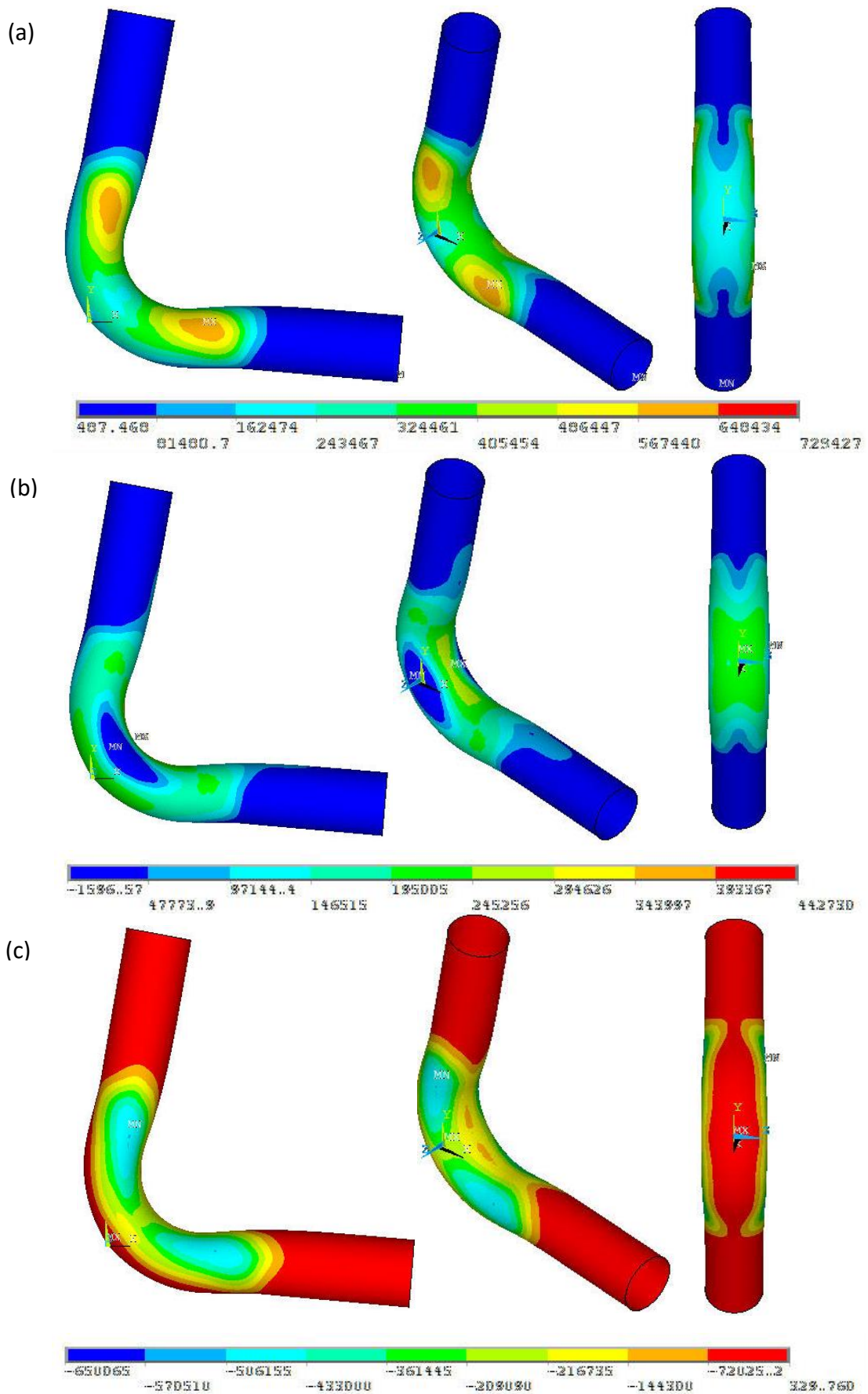
Figure 6-14: Model C side view, isometric view and back view of stress distribution in the stent: (a) von mises, (b) tensile and (c) compressive

(a)

(b)

(c)
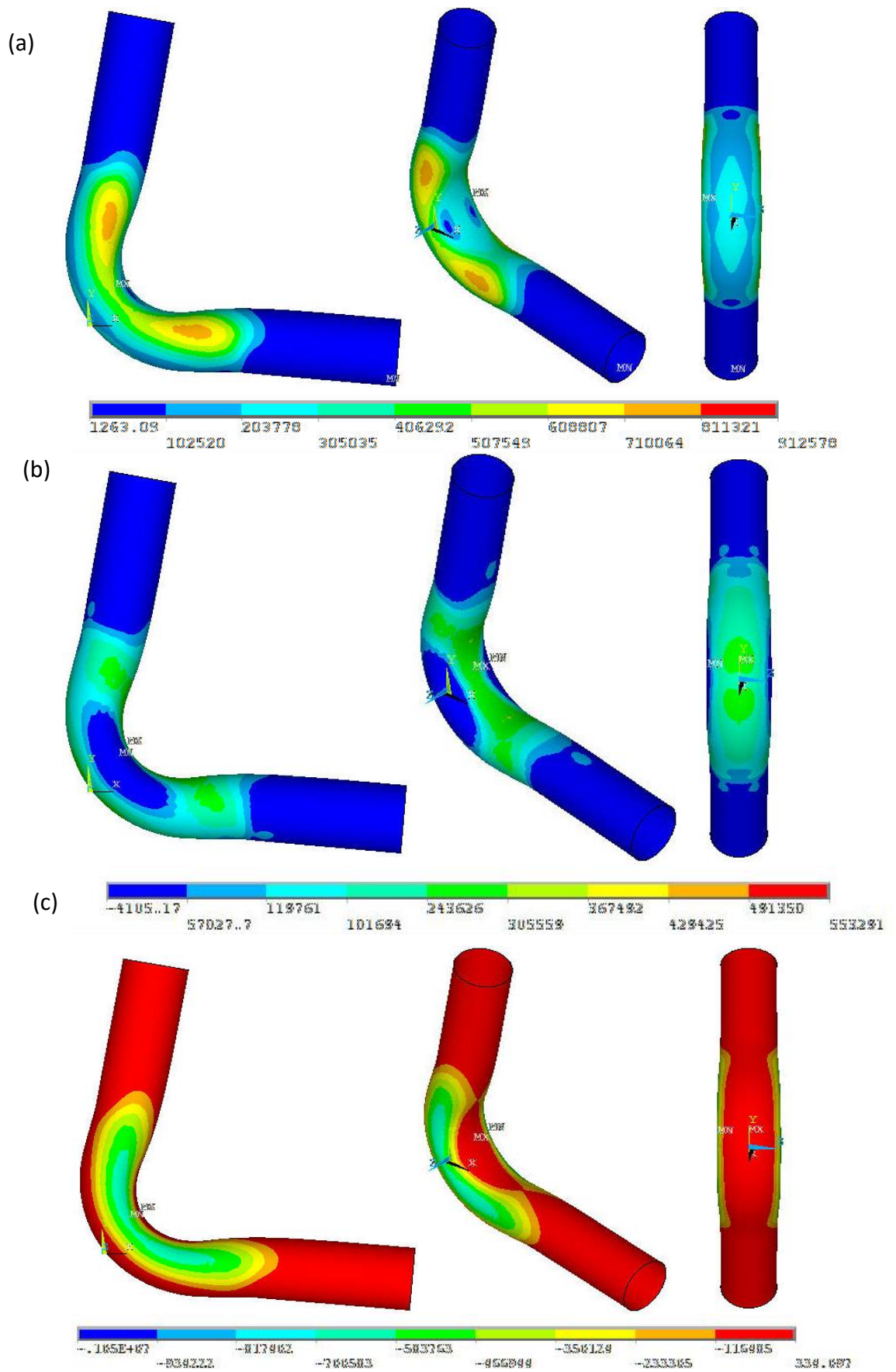
Figure 6-15: Model D side view, isometric view and back view of stress distribution in the stent: (a) von mises, (b) tensile and (c) compressive
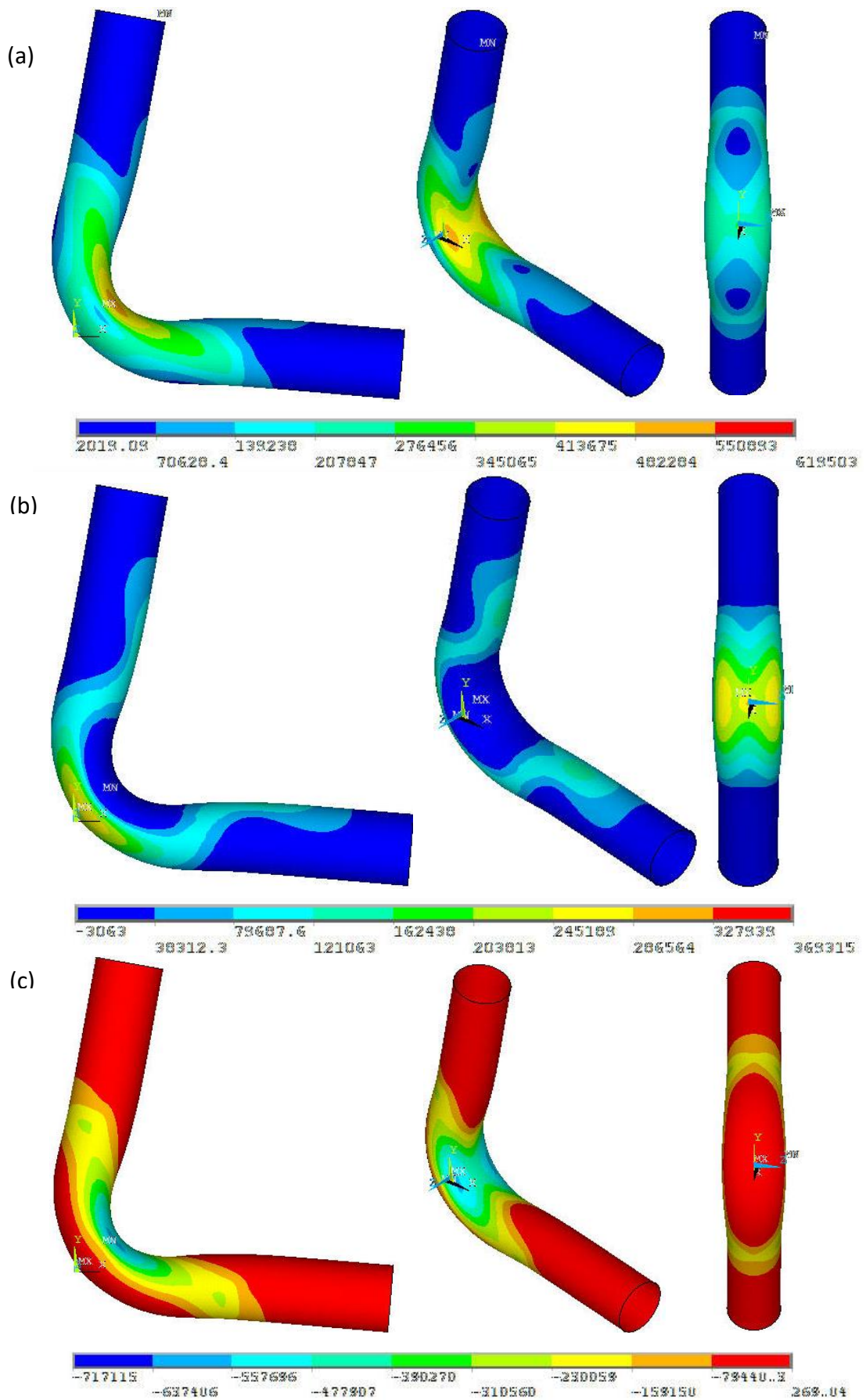
Figure 6-16: Model E side view, isometric view and back view of stress distribution in the stent: (a) von mises, (b) tensile and (c) compressive
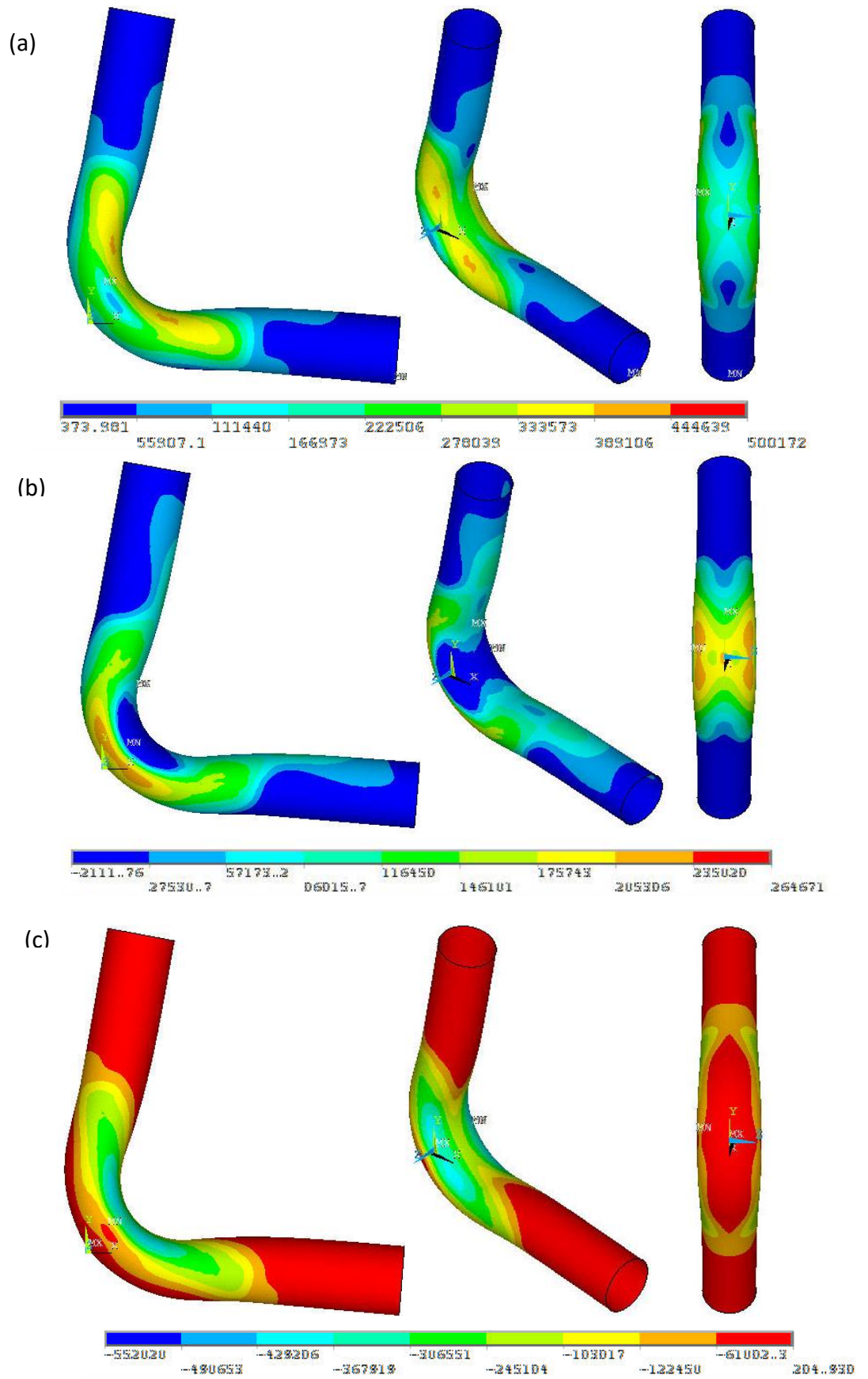
Figure 6-17: Model F side view, isometric view and back view of stress distribution in the stent: (a) von mises, (b) tensile and (c) compressive

6.5 Discussion

6.5.2 Model Generation

The geometry for the models in this chapter was relatively straightforward, however applying the boundary conditions was incredibly time consuming. Several variations of BCs were applied before deciding on those described in section 6.3. For the model with the appropriate mesh density as per the convergence study, the artery was discretised into a mesh of 3-D solid, 10-node elements (SOLID187) with a user-defined maximum element edge length of 0.2 mm. This resulted in a mesh of 243167 elements in the 1-layer models (models A-D) and 193278 in the 3-layer models (models E and F). The stent was represented by 13136 shell elements (SHELL281) located on the inner surface of the vessel (Figure 6-18).
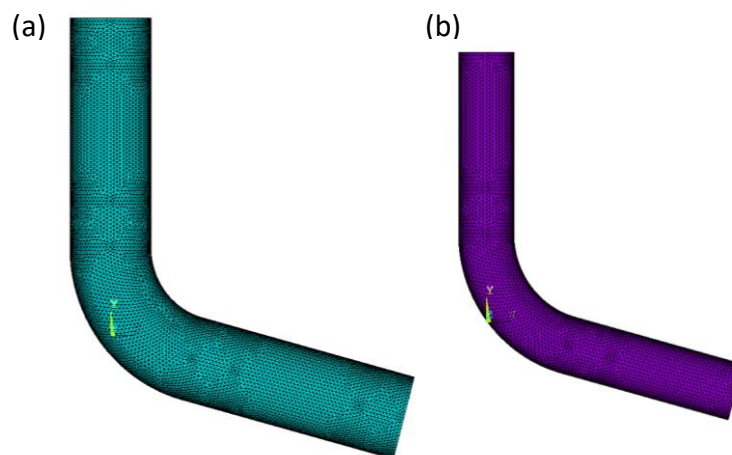
Figure 6-18: Discretised 1-layer model (a) artery and (b) stent

In the area selected to apply the displacements to, there were 14610 nodes upon which a 10° displacement was required to be applied. This required a considerable amount of time calculating the required displacement in both the X and Y directions using Microsoft Excel. Although it was particularly time-consuming when carrying out the convergence

study, the process was effective and resulted in a sufficiently loaded model with no highly localised points of stress to be accounted for by the boundary conditions.

6.5.3 Models A to F

The maximum stress values in the stent have been shown to vary for each of the different artery material models.

The maximum tensile stresses vary slightly between each of the models. With a standard deviation of 0.1 MPa, which is 27% of the mean value, there is a significant variation between the models (Table 6-14). There is also a similar amount of variation when looking at the maximum compressive stresses, with a standard deviation of 0.19 MPa (27% of average). The spread of maximum von Mises stresses is smaller than the tensile and compressive stresses with a standard deviation of 0.16 MPa, which is 22% of the mean.

Looking at the variation in the data from Table 6-13 and Figure 6-11, the linear artery model (Model A) and the hyperelastic silicone model (Model D) appear to be slightly further from the mean for von Mises and 3rd principal stresses than the remaining models. If these models are isolated from the others, the standard deviation for the maximum von Mises, 1st principal and 3rd principal stresses become 0.088 MPa, 0.069 MPa and 0.077 MPa respectively for Models B, C, E and F (Table 6-16). Compared to the results of all the models, the standard deviation is considerably lower than with models A and D included at 15%, 20% and 13% of the mean for the von Mises, 1st principal and 3rd principal stresses respectively.

The significantly lower standard deviation for the four hyperelastic artery models (Models B, C, E and F) suggests that they are more likely to result in a true representation of stent stresses than both the linear model and the silicone model (Models A and D

118

respectively). As Model A is a linear representation of the same material, it is likely that the material model is not complex enough to represent biological tissue. Similarly, the silicone model, although a more complex hyperelastic material model, may not closely enough represent the artery since it is based on a different material.

Table 6-16: Results from statistical analysis of models B, C, E, and F

	Maximum von Mises (B, C, E, F) *(all models)*	Maximum 1st Principal Stress (B, C, E, F) *(all models)*	Minimum 3rd Principal Stress (B, C, E, F) *(all models)*
Mean (MPa)	0.5970 *(0.6940)*	0.3245 *(0.3840)*	-0.6111 *(-0.7124)*
Standard deviation (SD) (MPa)	0.08775 *(0.1554)*	0.06937 *(0.1047)*	0.07722 *(0.1918)*
SD as a percentage of Mean (%)	14.70 *(22.40)*	20.26 *(27.27)*	12.64 *(26.93)*

The schematic in Figure 6-19 below shows a visual representation of which parts of the stent model are described as the "front", "side" and "back" of the stent, as well as "inside of the hinge-point" and "outside of the hinge-point" in this section.
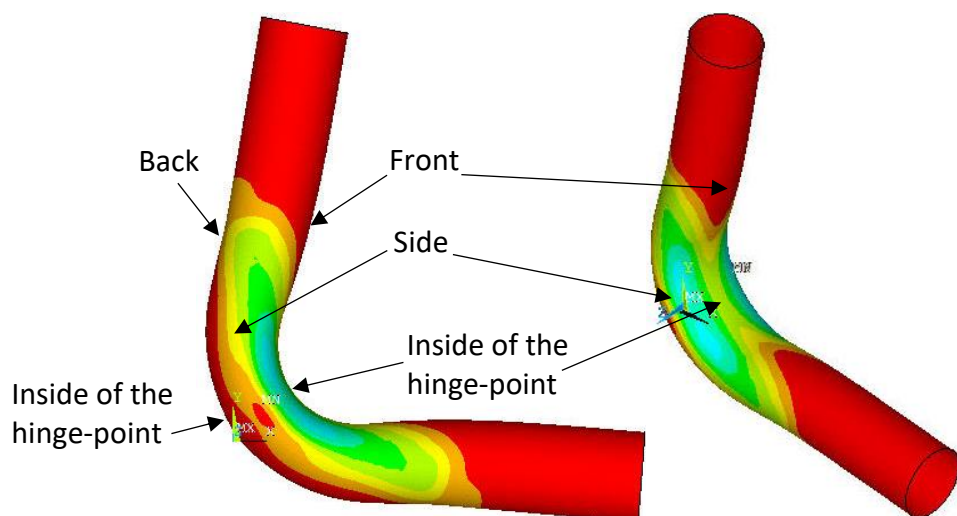
Figure 6-19: Schematic to show the locations of the different nomenclature used to describe the model.

All of the models have very similar von Mises stress distribution patterns as can be seen in Figure 6-12, Figure 6-13, Figure 6-14, Figure 6-15, Figure 6-16 and Figure 6-17. The points of highest von Mises stress are at two locations on the side of the hinge-point of the stent. For Model E, however, there is only one location in the centre of the side of the stent where the stress is highest. This suggests that overall, the most likely locations for SF would be the side of the hinge-point of the stent.

Due to the hinge-motion of the stent, the highest compressive stress would have been expected on the inside of the hinge-point. Instead, this was observed to be towards the front of the side of the stent in all models. The stress distribution for 3rd principal stress for each model are very similar, with the locations of highest stress values towards the front of the side the hinge-point.

Interestingly, there is more variation between the models when looking at the distribution of 1st principal stresses. For Models A, C and D, the locations of highest tensile stress are both the inside and outside of the hinge-point of the stent. The highest tensile stresses would have been expected on the outside of the hinge-point, which was observed in Models B, E and F, although areas of higher stress were also located towards the side of the stent in Model B.

6.5.4 Observations

The aim of this study was to assess the effect of the artery material models on the stent stresses and predict the likelihood and location of SF. From the results, it appears that the model is relatively insensitive to the artery material model when looking at locations of highest stress but more sensitive regarding the maximum stress values.

Although there was a variation in the maximum stress values with a standard deviation of over 22% for each of the stress values, this improved once the linear artery model (Model A) and the silicone hyperelastic model (Model D) were removed and only the four hyperelastic artery models remained. The standard deviation reduced to less than 20% of the mean for each of the maximum 1st principal, 3rd principal and von Mises stresses. The insensitivity of Models B, C, E and F to the stress distribution patterns suggest that the idealised model is relatively insensitive to the artery model, providing it was non-linear and it was a material model based on an artery. This meant that it would be reasonable to continue further analysis with one of models B, C, E and F. As models E and F are 3-layer models and are therefore more complex and time-consuming models to run, either model B or C would be the ideal model to use for further research.

The stress distribution plots show points of higher stress in unexpected locations such as locations of highest tensile stress on the inside of the hinge-point for Models A, C and D, and higher compressive stress on the side of the stent in all of the models. This increased stress may be the result of pressure from the artery model rather than any internal stresses from the device itself. If this is the case, then the stent may also be influenced by the structure of the artery.

Of all the models, the stress distribution patterns of model E fit the expected locations of highest tensile and compressive stresses better than any of the other models with the highest compressive stresses inside the hinge-point and highest tensile stresses on the outside. As the von Mises stress in this model is highest at two locations on the inside of the hinge-point, this may indicate that the most likely location for SF is in the inside of the hinge-point Figure 6-20. As this corresponds with the location of highest

compressive stresses, this suggests that SF is most likely to be caused by the repetitive compressive stresses in the device as the stent moves throughout the cardiac cycle.
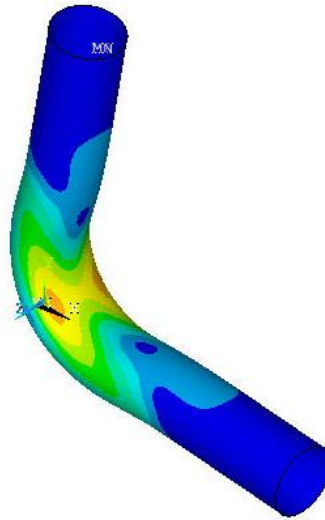
Figure 6-20: von Mises stress distribution pattern for Model E

Overall, the FE model may be relatively sensitive to the material model for the stent as well as the artery. As the higher von Mises stresses correspond with the locations of higher compressive stresses in the model, it is expected to be repetitive compression in the model that causes SF.

6.6 Conclusions

From available literature it is clear that no comparative work has been carried out to justify the necessity of using ever-more costly computing methods for the analysis of stent stresses. The artery material models used in this investigation are not being used in the same way as were intended by the initial authors. The aim was to assess whether, and to what extent the artery model affects the load transfer for stent stress analysis.

The results of this sensitivity study suggest that the stent stresses, and therefore indication of likelihood of SF, vary significantly between the many available non-linear analyses in Models A to F and therefore likelihood of SFis difficult to determine. As the method of failure is likely to be fatigue, it is difficult to determine the point at which failure would occur at stresses below the ultimate tensile strength of the material. In this case, the idealised model would be useful as a comparative model between two stent materials. This would enable stent material to be assessed to determine the material with lower stress values in this model, and therefore the material that is less likely to fail.

The stress distribution patterns of the models are, however, more similar than the maximum values, which indicates the location of likely SF to be towards the side of the stent, but still in the inside of the hinge-point.

In conclusion, stress analysis results are sensitive to the material model used to define the artery in terms of maximum stress values, but not when looking at stress distribution. Due to the complexity of the models, Model B is the preferred artery model to be used in future studies in order to achieve accurate results and reduce computing time.

7 Limitations of Study

There are several limitations of the studies presented it this thesis, many of which have been discussed in the various discussion sections in chapters 5 and 6.

The stent model developed in chapter 5 seemed to behave similarly to the stent samples that had undergone 3-point-bend testing. Unfortunately, there were only 3 devices available for testing, which meant that conclusions were drawn from a small sample of data and the test would have been more reliable had more stents been available to carry out further testing.

If a wider variety of stents were available, it would have been interesting to have been able to test larger selection of devices to assess how versatile the idealised model is. The model was designed to be entirely design-independent without localised points of higher stresses due to stent struts and other design artifacts. Although the model was confirmed to have been representative of the Resolute Integrity devices, if more stents could be tested, the model could have been assessed for how design-independent it is across a variety of stents.

As the sensitivity study showed a variety of maximum stress values across the different artery models when using the stent model validated in chapter 5, the results appear to be fairly inconclusive in terms of the likelihood of SF. This would be of more use as a comparative model looking at different stent materials to assess the one least likely to fracture.

8 Conclusions

The results of this study indicate that an idealised, design-independent stent model can be created using FE analysis software and realistically exhibit the behaviour of a stent undergoing a 3-point-bend mechanical test. The idealised model created had the same level of deflection as the sample tested in the lab for the load applied.

Unfortunately, the variety of maximum stress values observed in the results of the artery model sensitivity study suggests conclusions are unable to be drawn as to the likelihood of SF, however the model would be of use as a comparison between different stent devices and materials. The expected locations of SF in angulated vessels undergoing cyclical hinge-motion bending are on the inside of the hinge-point of the bend, however they are more likely to be found towards the side of the hinge-point than the middle.

9 Future Work

With the methods available for the validation of the idealised stent model in chapter 5, further stent devices should be tested and compared to the results from the Resolute Integrity. The idealised model could then be assessed to see how universal it is and how useful it may be in other research avenues.

The sensitivity study should be utilised with a variety of different stent materials and devices to assess the ones most likely to fracture. This should be studied alongside a mechanical test of the same configuration so that comparisons can be made and conclusions drawn as to the accuracy of the model.

References

AL SUWAIDI, J., BERGER, P.B., RIHAL, C.S., GARRATT, K.N., BELL, M.R., TING, H.H., BRESNAHAN, J.F., GRILL, D.E. and HOLMES JR., D.R., 2000. Immediate and long-term outcome of intracoronary stent implantation for true bifurcation lesions. *Journal of the American College of Cardiology,* **35**(4), pp. 929-936.

ALEXOPOULOS, D. and XANTHOPOULOU, I., 2011. Coronary stent fracture: How frequent it is? Does it matter? *Hellenic Journal of Cardiology*, **52**(1), pp. 1-5.

ALLIE D.E., HEBERT C.J., WALKER C.M., 2004. Nitinol stent fractures in the SFA: the biomechanical forces exerted on the SFA provide a "stiff" challenge to endovascular stenting. *Endovascular Today*, **7,** pp.22–34.

ASTM, 2008. *F2606: Standard guide for three-point bending of balloon expandable vascular stents and stent systems*. ASTM International, West Conshohocken, PA, USA.

BRIGUORI, C., SARAIS, C., PAGNOTTA, P., LIISTRO, F., MONTORFANO, M., CHIEFFO, A., SGURA, F., CORVAJA, N., ALBIERO, R., STANKOVIC, G., TOUTOUTZAS, C., BONIZZONI, E., DI MARIO, C. and COLOMBO, A., 2002. In-stent restenosis in small coronary arteries: Impact of strut thickness*. Journal of the American College of Cardiology*, **40**(3), pp. 403-409.

BRITISH HEART FOUNDATION (2020) *Heart and Circulatory Disease Statistics 2020.* British Heart Foundation and the Institute of Applied Health Research at the University of Birmingham.

CANFIELD, T.R. and DOBRIN, P.B., 2006. Mechanics of blood vessels. In: J.D. BRONZINO, ed, *The Biomedical Engineering Handbook, Third Edition: Biomedical Engineering Fundamentals.* 3 edn. CRC Press, pp. 57-1-57-13.

CAREW, T.E., VAISHNAV, R.N., PATEL, D.J., 1968. Compressibility of the arterial wall. *Circulation Research*, **23**(1), pp. 61-68.

CHIACHANA, T., SUN, Z., JEWKES, J., 2011. Computation of haemodynamics int he left coronary artery with variable angulations. *Journal of Biomechanics,* **44**, pp. 1869-1878.

CHUA, S.N.D., MACDONALD, B.J., and HASHMI, M.S.J., 2004. Finite element simulation of slotted tube (stent) with the presence of plaque and artery by balloon expansion. *Journal of Materials Processing Technology*, **155-156**(1-3), pp. 1772-1779.

CONTI, M., 2010. *Finite Element Analysis of Carotid Artery Stenting.* PhD thesis. Università degli Studi di Pavia, and Ghent University.

CONTI, J.C., STROPE, E.R., PRICE, K.S., GOLDENBERG, L.M., 1999. The high frequency testing of vascular grafts and vascular stents: Influence of sample dimensions on maximum allowable frequency. *Biomedical Sciences Instrumentation*, **35**, pp. 339-346.

CONTI, J.C., STROPE, E.R., GOLDENBERG, L.M., PRICE, K.S., 2001. The durability of silicone versus latex mock arteries. *Biomedical Sciences Instrumentation*, **37**, pp. 305-312.

COOK, R.D., MALKUS, D.S., PLESHA, M.E. and WITT, R.J., 2001. Concepts and Applications of Finite Element Analysis. 4th edn. Wiley.

DANEAULT, B., BAIRD, S. and KIRTANE, A.J., 2014. Acute Left Main Coronary Occlusion Caused by Stent Fracture, Peri-Stent Aneurysm Formation, and Very-Late Stent Thrombosis: Revisiting the Dark Side of Drug-Eluting Stents. *Canadian Journal of Cardiology*, **30**(1), pp. 146.e1-146.e3.

DEAN, R.T. and KELLY, D.T., eds, 2000. *Atherosclerosis: gene expression, cell interactions and oxidation.* New York: Oxford University Press.

DOI, H., MAEHARA, A., MINTZ, G.S., TSUJITA, K., KUBO, T., CASTELLANOS, C., LIU, J., YANG, J., OVIEDO, C., AOKI, J., FRANKLIN-BOND, T., DASGUPTA, N., LANSKY, A.J., DANGAS, G.D., STONE, G.W., MOSES, J.W., MEHRAN, R. and LEON, M.B., 2009. Classification and Potential Mechanisms of Intravascular Ultrasound Patterns of Stent Fracture. *American Journal of Cardiology,* **103**(6), pp. 818-823.

DRAKE, R.L., VOGL, A.W. and MITCHELL, A.W.M., 2010. *Gray's Anatomy for Students.* 2 edn. Churchill Livingstone.

DUERIG, T.W. and WHOLEY, M., 2002. A comparison of balloon- and self-expanding stents. *Minimally Invasive Therapy and Allied Technologies,* **11**(4), pp. 173-178.

FERNANDEZ-ORTIZ, A., BADIMON, J.J., FAULK, E., FUSTER, V., MEYER, B., MAILHAC, A., WENG, D., SHAH, P.K. and BADIMON, L., 1994. Characterization of the relative thrombogenicity of atherosclerotic plaque components: Implications for consequences of plaque rupture. *Journal of the American College of Cardiology*, **23**(7), pp. 1562-1569.

FISCHMAN, D.L., LEON, M.B., BAIM, D.S., SCHATZ, R.A., SAVAGE, M.P., PENN, I., DETRE, K., VELTRI, L., RICCI, D., NOBUYOSHI, M., CLEMAN, M., HEUSER, R., ALMOND, D., TEIRSTEIN, P.S., FISH, R.D., COLOMBO, A., BRINKER, J., MOSES, J., SHAKNOVICH, A., HIRSHFELD, J., BAILEY, S., ELLIS, S., RAKE, R. and GOLDBERG, S., 1994. A randomized comparison of coronary-stent placement and balloon angioplasty in the treatment of coronary artery disease. *New England Journal of Medicine,* **331**(8), pp. 496-501.

GAGE, K.L. and WAGNER, W.R., 2003. Cardiovascular devices. In: M. KUTZ, ed, *Standard Handbook of Biomedical Engineering & Design.* United States of America: McGRAW-HILL, pp. 20.1-20.48.

GASTALDI D., MORLACCHI S., NICHETTI R., CAPELLI C., DUBINI G., PETRINI L., MIGLIAVACCA F., 2010. Modelling of the provisional side-branch stenting approach for the treatment of atherosclerotic coronary bifurcations: Effects of stent positioning. Biomechanics and Modeling in Mechanobiology, 9(5), pp. 551-561.

GRIENDLING, K.K. and ALEXANDER, R.W., 1998. Cellular Biology of Blood Vessels. In: R.W. ALEXANDER, R.C. SCHLANT, V. FUSTER, R.A. O'ROURKE, R. ROBERTS and E.H. SONNENBLICK, eds, *Hurst's the Heart, Ninth Edition.* 9 edn. New York: McGraw-Hill, pp. 125-141.

HAJIALI Z., DABAGH M., JALALI P., 2014. A Computational Model to Assess Poststenting Wall Stresses Dependence on Plaque Structure and Stenosis Severity in Coronary Artery. Mathematical Problems in Engineering, 2014, art. no. 937039.

HAUDRECHY, P., FOUSSEREAU, J., MANTOUT, B., and BAROUX, B., 1993. Nickel release from 304 and 316 stainless steels in synthetic sweat. Comparison with nickel and nickel-plated metals. Consequences on allergic contact dermatitis. *Corrosion Science,* **35**(1–4):329–36.

HEINTZ, C., RIEPE, G., BIRKEN, L., KAISER, E., CHAKFÃ, N., MORLOCK, M., DELLING, G. and IMIG, H., 2001. Corroded nitinol wires in explanted aortic endografts: An important mechanism of failure? *Journal of Endovascular Therapy*, **8**(3), pp. 248-253.

HIGASHIURA, W., KUBOTA, Y., SAKAGUCHI, S., KURUMATANI, N., NAKAMAE, M., NISHIMINE, K. and KICHIKAWA, K., 2009. Prevalence, factors, and clinical impact of self-expanding stent fractures following iliac artery stenting. *Journal of Vascular Surgery,* **49**(3), pp. 645-652.

HOLZAPFEL, G.A., GASSER, T.C., ODGEN, R.W., 2000. A new constitutive framework for arterial wall mechanics and a comparative study of material models. Journal of Elasticity, 61(1-3), pp. 1-48.

HOLZAPFEL, G.A., STADLER, M., GASSER, T.C., 2005. Changes in the mechanical environment of stenotic arteries during interaction with stents: Computational assessment of parametric stent designs. *Journal of Biomechanical Engineering*, **127**(1), pp. 166-180.

Human Tissue Act, 2004. Available online: https://www.legislation.gov.uk/ukpga/2004/30/pdfs/ukpga_20040030_en.pdf

[Accessed 21/09/2020]

IAKOVOU, I., GE, L. and COLOMBO, A., 2005. Contemporary stent treatment of coronary bifurcations. *Journal of the American College of Cardiology,* **46**(8), pp. 1446-1455.

KAN, J., GE, Z., ZHANG, J.-J., LIU, Z.-Z., TIAN, N.-L., YE, F., LI, S.-J., QIAN, X.-S., YANG, S., CHEN, M.-X., RAB, T., CHEN, S.-L., 2016. Incidence and clinical outcomes of stent fractures on the basis of 6,555 patients and 16,482 drug-eluting stents from four centers. JACC: Cardiovascular Interventions, 9(11), pp. 1115-1123.

KANG, W.Y., KIM, W., HWANG, S.H. and KIM, W., 2009. Dark side of drug-eluting stent: Multiple stent fractures and sudden death. *International Journal of Cardiology,* **132**(3), pp. e125-e127.

KANG, W.Y., KIM, W., KIM, H.G. and KIM, W., 2007. Drug-eluting stent fracture occurred within 2 days after stent implantation. *International Journal of Cardiology,* **120**(2), pp. 273-275.

KEREIAKES, D.J., COX, D.A., HERMILLER, J.B., MIDEI, M.G., BACHINSKY, W.B., NUKTA, E.D., LEON, M.B., FINK, S., MARIN, L. and LANSKY, A.J., 2003. Usefulness of a cobalt chromium coronary stent alloy. *The American Journal of Cardiology*, **92**(4), pp. 463-466.

KHANNA, R., KAPOOR, A., SINHA, N., 2012. Acute ST-elevation myocardial infarction 6 years following a sirolimus-eluting stent secondary to complete stent fracture. *Journal of Invasive Cardiology.*, **24**(4) E64-E66.

KOENIG, W. and KHUSEYINOVA, N., 2006. Biomarkers of atherosclerotic plaque instability and rupture. *Arteriosclerosis, Thrombosis, and Vascular Biology,* **27**, pp. 15-26.

KURAMITSU, S., IWABUCHI, M., HARAGUCHI, T., DOMEI, T., NAGAE, A., HYODO, M., YAMAJI, K., SOGA, Y., ARITA, T., SHIRAI, S., KONDO, K., ANDO, K., SAKAI, K., GOYA, M., TAKABATAKE, Y., SONODA, S., YOKOI, H., TOYOTA, F., NOSAKA, H. and NOBUYOSHI, M., 2012. Incidence and clinical impact of stent fracture after everolimus-eluting stent implantation. *Circulation: Cardiovascular Interventions*, **5**(5), pp. 663-671.

LALLY, C., DOLAN, F. and PRENDERGAST, P.J., 2005. Cardiovascular stent design and vessel stresses: A finite element analysis. *Journal of Biomechanics*, **38**(8), pp. 1574-1581.

LEE, M.S., JUREWITZ, D., ARAGON, J., FORRESTER, J., MAKKAR, R.R. and KAR, S., 2007. Stent fracture associated with drug-eluting stents: Clinical characteristics and implications. Catheterization and Cardiovascular Interventions, **69**(3), pp. 387-394.

LEE, P.H., LEE, S.-W., LEE, J.-Y., KIM, Y.-H., LEE, C.W., PARK, D.-W., PARK, S.-W. and PARK, S.-J., 2015. Two cases of immediate stent fracture after zotarolimus-eluting stent implantation. *Korean Circulation Journal*, **45**(1), pp. 67-70.

LEE, S.E., JEONG, M.H., KIM, I.S., KO, J.S., LEE, M.G., KANG, W.Y., KIM, S.Y., SIM, D.S., PARK, K.H., YOON, N.S., YOON, H.J., KIM, K.H., HONG, Y.J., PARK, H.W., KIM, J.H., AHN, Y.K., CHO, J.G., PARK, J.C. and KANG, J.K., 2009. Clinical outcomes and optimal treatment for stent fracture after drug-eluting stent implantation. *Journal of Cardiology,* **53**, pp. 422-428.

LEFÈVRE, T., LOUVARD, Y., MORICE, M.-., DUMAS, P., LOUBEYRE, C., BENSLIMANE, A., PREMCHAND, R.K., GUILLARD, N. and PIÉCHAUD, J.-., 2000. Stenting of bifurcation

lesions: Classification, treatments, and results. Catheterization and Cardiovascular Interventions, **49**(3), pp. 274-283.

LIANG D.K., YANG D.Z., QI M., WANG W.Q., 2005. Finite element analysis of the implantation of a balloon-expandable stent in a stenosed artery. International Journal of Cardiology, 104 (3), pp. 314-318.

LOREE, H.M., GRODZINSKY, A.J., PARK, S.Y., GIBSON, L.J., LEE, R.T., 1994a. Static circumferential tangential modulus of human atherosclerotic tissue. *Journal of Biomechanics*, **27**(2), pp. 195-204.

LOREE, H.M., TOBIAS, B.J., GIBSON, L.J., KAMM, R.D., SMALL, D.M., LEE, R.T., 1994b. Mechanical properties of model atherosclerotic lesion lipid pools. *Arteriosclerosis and Thrombosis*, **14**(2), pp. 230-234.

LOUSINHA, A., FIARRESGA, A., CARDONA, L., LOPES, J.P., LOPES, A., CACELA, D., DE SOUSA, L., PATRÍCIO, L., BERNARDES, L., FERREIRA, R.C., 2011. Stent fracture: case report and literature review. *Rev Port Cardiol*, **30**(2), pp.213–221.

MANI, G., FELDMAN, M.D., PATEL, D. and AGRAWAL, C.M., 2007. Coronary stents: A materials perspective. *Biomaterials,* **28**(9), pp. 1689-1710.

MANOLA, Å., PINTARIÄ†, H., PAVLOVIÄ†, N. and Å TAMBUK, K., 2010. Coronary artery stent fracture with aneurysm formation and in-stent restenosis. *International journal of cardiology*, **140**(2), pp. e36-e39.

MARTIN, D. and BOYLE, F.J., 2011. Computational structural modelling of coronary stent deployment: A review. *Computer methods in biomechanics and biomedical engineering*, **14**(4), pp. 331-348.

MARTIN, D., BOYLE, F., 2013. Finite element analysis of balloon-expandable coronary stent deployment: Influence of angioplasty balloon configuration. International Journal for Numerical Methods in Biomedical Engineering, 29(11), pp. 1161-1175.

MARTINS, P.A.L.S., NATAL JORGE, R.M. and FERREIRA, A.J.M., 2006. A Comparative Study of Several Material Models for Prediction of Hyperelastic Properties: Application to Silicone-Rubber and Soft Tissues. *Strain*, **42**, pp. 135–147.

132

MATSUNO, H., YOKOYAMA, A., WATARI, F., UO, M. and KAWASAKI, T., 2001. Biocompatibility and osteogenesis of refractory metal implants, titanium, hafnium, niobium, tantalum and rhenium. *Biomaterials*, **22**(11), pp. 1253-1262.

MCDOUGALL, J., 2006. The Angioplasty Debacle. *The McDougall Newsletter,* **5**(9).

MOONEY, M., 1940. A Theory of Large Elastic Deformation. *Journal of Applied Physics*, **11**, pp. 582.

MEDTRONIC, 2013. Resolute Integrity Zotarolimus-Eluting Coronary Stent System Rapid Exchange Delivery System: Instructions for use. Available online: https://www.accessdata.fda.gov/cdrh_docs/pdf11/P110013S005c.pdf [Accessed 21/09/2020].

MORICE, M.-C., SERRUYS, P.W., EDUARDO SOUSA, J., FAJADET, J., HAYASHI, E.B., PERIN, M., COLOMBO, A., SCHULER, G., BARRAGAN, P., GUAGLIUMI, G., MOLNÀR, F. and FALOTICO, R., 2002. A randomized comparison of a sirolimus-eluting stent with a standard stent for coronary revascularization. *New England Journal of Medicine,* **346**(23), pp. 1773-1780.

MOSES, J.W., LEON, M.B., POPMA, J.J., FITZGERALD, P.J., HOLMES, D.R., O'SHAUGHNESSY, C., CAPUTO, R.P., KEREIAKES, D.J., WILLIAMS, D.O., TEIRSTEIN, P.S., JAEGER, J.L. and KUNTZ, R.E., 2003. Sirolimus-eluting stents versus standard stents in patients with stenosis in a native coronary artery. *The New England Journal of Medicine,* **349**(14), pp. 1315-1323.

MURPHY, B.P., SAVAGE, P., MCHUGH, P.E. and QUINN, D.F., 2003. The stress-strain behaviour of coronary stent struts is size dependent. *Annals of Biomedical Engineering,* **31**, pp. 686-691.

NAKAZAWA, G., FINN, A.V., VORPAHL, M., LADICH, E., KUTYS, R., BALAZS, I., KOLODGIE, F.D. and VIRMANI, R., 2009. Incidence and Predictors of Drug-Eluting Stent Fracture in Human Coronary Artery. A Pathologic Analysis. *Journal of the American College of Cardiology,* **54**(21), pp. 1924-1931.

NICOR (National Institute for Cardiovascular Outcomes Research), 2013. National Audit of Percutaneous Coronary Interventions. London: UCL. Available online:

http://www.ucl.ac.uk/nicor/audits/adultpercutaneous/documents/2013_annual_repo rt_pdf [Accessed 07/01/16]

O'BRIEN, B. and CARROLL, W., 2009. The evolution of cardiovascular stent materials and surfaces in response to clinical drivers: A review. *Acta Biomaterialia*, **5**(4), pp. 945-958.

PAN, M., SUÁREZ DE LEZO, J., MEDINA, A., ROMERO, M., HERNÁNDEZ, E., SEGURA, J., CASTROVIEJO, J.R., PAVLOVIC, D., MELIAN, F., RAMÍREZ, A. and CASTILLO, J.C., 1999. Simple and complex stent strategies for bifurcated coronary arterial stenosis involving the side branch origin. *The American Journal of Cardiology,* **83**(9), pp. 1320-1325.

PARK, J. and LAKES, R.S., 2007. Metallic Implant Materials. Biomaterials. 3rd edn. New York: Springer, pp. 99-137.

PELTON, A.R., SCHROEDER, V., MITCHELL, M.R., GONG, X.-Y., BARNEY, M. and ROBERTSON, S.W., 2008. Fatigue and durability of Nitinol stents. *Journal of the Mechanical Behaviour of Biomedical Materials,* **1**(2), pp. 153-164.

PERICEVIC, I., LALLY, C., TONER, D., KELLY, D.J., 2009. The influence of plaque composition on underlying arterial wall stress during stent expansion: The case for lesion-specific stents. Medical Engineering and Physics, 31(4), pp. 428-433.

POPMA, J.J., TIROCH, K., ALMONACID, A., COHEN, S., KANDZARI, D.E. and LEON, M.B., 2009. A Qualitative and Quantitative Angiographic Analysis of Stent Fracture Late Following Sirolimus-Eluting Stent Implantation. *American Journal of Cardiology,* **103**(7), pp. 923-929.

PRENDERGAST, P.J., LALLY, C., DALY, S., REID, A.J., LEE, T.C., QUINN, D., DOLAN, F., 2003. Analysis of Prolapse in Cardiovascular Stents: A Constitutive Equation for Vascular Tissue and Finite-Element Modelling. *Journal of Biomechanical Engineering*, **125**(5), pp. 692-699.

RAJESH, R., STROPE, E.R., PRICE, K.S., CONTI, J.C., 2005. Frequency dependent hysteresis of silicone and latex mock arteries used in stent testing. *Biomedical Sciences Instrumentation*, **41**, pp. 163-168.

ROCHA-SINGH, K.J., JAFF, M.R., CRABTREE, T.R., BLOCH, D.A. and ANSEL, G., 2007. Performance Goals and Endpoint Assessments for Clinical Trials of Femoropopliteal Bare

Nitinol Stents in Patients With Symptomatic Peripheral Arterial Disease. *Catheterization and Cardiovascular Interventions,* **69**, pp. 910-919.

ROGERS, C., TSENG, D.Y., SQUIRE, J.C. and EDELMAN, E.R., 1999. Balloon-artery interactions during stent placement: A finite element analysis approach to pressure, compliance, and stent design as contributors to vascular injury. *Circulation Research*, **84**(4), pp. 378-383.

SAVAGE, P., O'DONNELL, B.P., MCHUGH, P.E., MURPHY, B.P. and QUINN, D.F., 2004. Coronary stent strut size dependent stress-strain response investigated using micromechanical finite element models. *Annals of Biomedical Engineering,* **32**(2), pp. 202-211.

SCHEINERT, D., SCHEINERT, S., SAX, J., PIORKOWSKI, C., BRÄUNLICH, S., ULRICH, M., BIAMINO, G. and SCHMIDT, A., 2005. Prevalence and clinical impact of stent fractures after femoropopliteal stenting. Journal of the American College of Cardiology, **45**(2), pp. 312-315.

SEURRYS, P.W., DE JAEGERE P., KIEMENEIJ F., KIEMENEIJ, F., MACAYA, C., RUTSCH, W., HEYNDRICKX, G., EMANUELSSON, H., MARCO, J., LEGRAND, V., MATERNE, P., BELARDI, J., SIGWART, U., COLOMBO, A., GOY, J.J., VAN DE HEUVEL, P., DECLAN, J. and MORELI, M., 1994. A comparison of balloon-expandable-stent implantation with balloon angioplasty in patients with coronary artery disease. *New England Journal of Medicine*, **331**(8) pp. 489–495.

SHANG K., 2014. The effects of vascular residual stress on cardiovascular stent implanting: A finite element analysis. 2014 IEEE Workshop on Electronics, Computer and Applications, art. no. 6845790, pp. 995-998.

SHAIKH, F., MADDIKUNTA, R., DJELMAMI-HANI, M., SOLIS, J., ALLAQABAND, S., BAJWA T., 2008. Stent fracture, an incidental finding or a significant marker of clinical in-stent restenosis?. *Catheterization and Cardiovascular Interventions,* **71**(5) pp.614-618.

SIANOS, G., HOFMA, S., LIGTHART, J., SAIA, F., HOYE, A., LEMOS, P. and SERRUYS, P., 2004. Stent Fracture and Restenosis in the Drug-Eluting Stent Era. *Catheterization and Cardiovascular Interventions,* **61**, pp. 111-116.

SIMARD, T., HIBBERT, B., RAMIREZ, F.D., FROESCHL, M., CHEN, Y.-. and O'BRIEN, E.R., 2014. The Evolution of Coronary Stents: A Brief Review. *Canadian Journal of Cardiology,* **30**(1), pp. 35-45.

STARY, H.C., CHANDLER, A.B., GLAGOV, S., GUYTON, J.R., INSULL JR., W., ROSENFELD, M.E., SCHAFFER, S.A., SCHWARTZ, C.J., WAGNER, W.D. and WISSLER, R.W., 1994. A definition of initial, fatty streak, and intermediate lesions of atherosclerosis: A report from the committee on vascular lesions of the council on arteriosclerosis, American Heart Association. *Circulation*, **89**(5), pp. 2462-2478.

STARY, H.C., CHANDLER, A.B., DINSMORE, R.E., FUSTER, V., GLAGOV, S., INSULL JR., W., ROSENFELD, M.E., SCHWARTZ, C.J., WAGNER, W.D. and WISSLER, R.W., 1995. A definition of advanced types of atherosclerotic lesions and a histological classification of atherosclerosis: A report from the committee on vascular lesions of the council on arteriosclerosis, American Heart Association. *Circulation*, **92**(5), pp. 1355-1374.

STARY, H.C., 2000. Natural history and histological classification of atherosclerotic lesions: An update. *Arteriosclerosis, Thrombosis, and Vascular Biology*, **20**(5), pp. 1177-1178.

STOECKEL, D., BONGIGNORE, C. and DUDA, S., 2002. A survey of stent designs. *Minimally Invasive Therapy and Allied Technologies,* **11**(4), pp. 137-147.

STOECKEL, D., PELTON, A. and DUERIG, T., 2004. Self-expanding Nitinol stents: Material and design considerations. *European Radiology,* **14**(2), pp. 292-301.

TAMBACA, J., CANIC, S., KOSOR, M., FISH, R.D. and PANIAGUA, D., 2011. Mechanical behavior of fully expanded commercially available endovascular coronary stents. *Texas Heart Institute Journal*, **38**(5), pp. 491-501.

THIERRY, B., BILODEAU, L. and TABRIZIAN, M., 2004. Stents. In: G.E. WNEK and G.L. BOWLIN, eds, *Encyclopedia of Biomaterials and Biomedical Engineering.* New York: Marcel Dekker, pp. 1403-1411.

TREPANIER, C., VENUGOPALAN, R. and PELTON, A.R., 2000. Corrosion Resistance and Biocompatibility of Passivated NiTi. In: L. YAHIA, (ed), *Shape Memory Implants*. Springer London, Limited, pp. 35-45.

VERESS, A.I., VINCE, D.G., ANDERSON, P.M., CORNHILL, J.F., HERDERICK, E.E., KLINGENSMITH, J.D., KUBAN, B.D., GREENBERG, N.L., THOMAS, J.D., VERESS, A.I., 2000. Vascular mechanics of the coronary artery. *Zeitschrift fur Kardiologie*, **89**(SUPPL. 2), pp. II92-II100.

WAKSMAN, R. and BONELLO, L., 2008. The 5 Ts of Bifurcation Intervention: Type, Technique, Two Stents, T-Stenting, Trials**Editorials published in JACC: Cardiovascular Interventions reflect the views of the authors and do not necessarily represent the views of JACC: Cardiovascular Interventions or the American College of Cardiology. *JACC: Cardiovascular Interventions,* **1**(4), pp. 366-368.

WEINHAUS A.J., 2015. Anatomy of the Human Heart. In: IAIZZO P., eds, *Handbook of Cardiac Anatomy, Physiology, and Devices.* Springer, Cham. https://doi.org/10.1007/978-3-319-19464-6_5, pp. 59-85.

WILLIAMS, J.A. and DWYER-JOYCE, R.S., 2000. Contact between solid surfaces. In Bhushan, B. (e.d.) *Modern Tribology Handbook Volume One.* Boca Raton: CRC Press, pp. 121-163.

YAMASHITA, T., NISHIDA, T., ADAMIAN, M.G., BRIGUORI, C., VAGHETTI, M., CORVAJA, N., ALBIERO, R., FINCI, L., DI MARIO, C., TOBIS, J.M. and COLOMBO, A., 2000. Bifurcation lesions: two stents versus one stent—immediate and follow-up results. *Journal of the American College of Cardiology,* **35**(5), pp. 1145-1151.

ZAHEDMANESH, H., LALLY, C., 2009. Determination of the influence of stent strut thickness using the finite element method: Implications for vascular injury and in-stent restenosis. Medical and Biological Engineering and Computing, 47(4), pp. 385-393.

Appendix

A Effective Modulus Calculation

In order to validate the idealised stent model, an effective modulus was first calculated using the bending stiffness of the device. A 3-point bend test was carried out as outlined in chapter 5 The results were then used to inform the calculation of an 'effective' modulus for the tubular device for use in FE analysis.

The equation describing beam deflection can be approximated as (Equation A-1);

$$\frac{d^2y}{dx^2} = \frac{M(x)}{EI}$$
Equation A-1

Where y is the vertical displacement, x is the distance along the beam, M is the bending moment, E is the Young's modulus of the material and I is the second moment of area of the beam. Flexural rigidity is defined as the product EI, which is assumed to be constant in the case of a prismatic beam. In this case, the stent is being approximated to a cylindrical tube, thus is assumed to be prismatic. The equation can then be integrated to obtain Equation A-2:

$$EI\frac{dy}{dx} = \int_0^x M(x)dx + C_1$$
Equation A-2

The tangent of the elastic curve forms a very small angle with the horizontal (Figure A-1), therefore we can approximate the tangent to be equal to the angle as in Equation A-3.
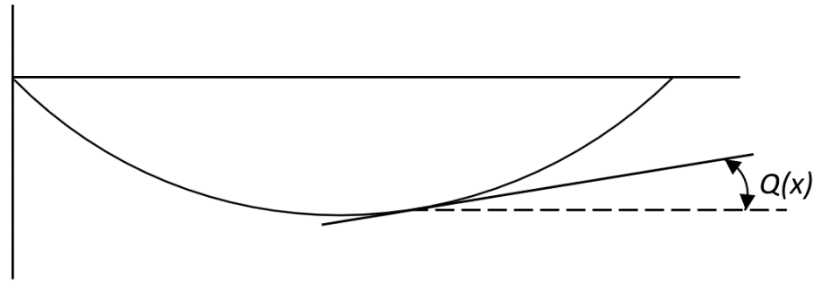
Figure A-1: deflection of the beam showing angle of tangent relative to the horizontal.

$$\frac{dy}{dx} = tan\theta \cong \theta(x)$$
Equation A-3

Thus we can say;

$$EI\ \theta(x) = \int_0^x M(x)dx + C_1$$
Equation A-4

Integrating through, we have:

$$EI\ y = \int_0^x \left[\int_0^x M(x)dx + C_1\right] dx + C_2$$
Equation A-5

$$EI\ y = \int_0^x dx \int_0^x M(x)dx + C_1 + C_2$$
Equation A-6

For a simply supported prismatic beam with a midpoint load, *P*, as in the case of the

stent (Figure A-2);
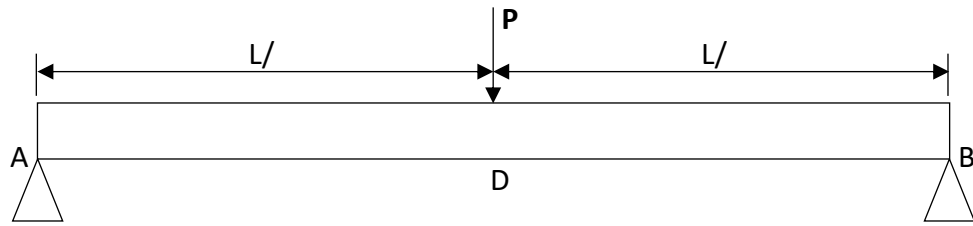
Figure A-2: Free body diagram of three-point bend of the stent

The beam was split into two portions, AD and DB, and bending moment calculations were carried out. Looking at the beam section by section (Figure A-3):

1.   From A to D
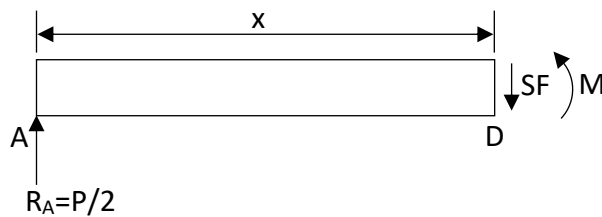
Figure A-3: Free body diagram for section 1

$$\sum fy_1 = 0 = R_A - P + R_B \qquad \text{Equation A-7}$$

$$R_A + R_B = P \qquad \text{Equation A-8}$$

$$R_A = R_B \qquad \text{Equation A-9}$$

Therefore, from Equations A-8 and A-9, the reaction forces could be defined (Equation A-10);

$$\therefore R_A = R_B = \frac{P}{2} \qquad \text{Equation A-10}$$

By carrying out bending moment calculations we get;

$$M = \frac{P}{2}x \qquad \Rightarrow \qquad EI\,\frac{d^2y_1}{dx^2} = \frac{P}{2}x \qquad \text{Equation A-11}$$

$$EI\,\frac{dy_1}{dx} = \frac{P}{4}x^2 + C_1 \qquad \text{Equation A-12}$$

$$EI\,y_1 = \frac{P}{12}x^3 + C_1x + C_2 \qquad \text{Equation A-13}$$

From D to B (Figure A-4);
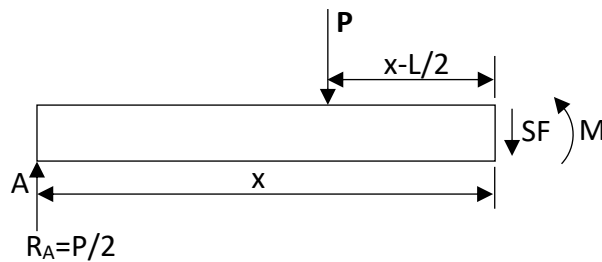
Figure A-4: Free body diagram for section 2

$$M = \frac{P}{2}x - P\left(x - \frac{L}{2}\right) = -\frac{P}{2}x + \frac{PL}{2} \qquad \Rightarrow \qquad EI\,\frac{d^2y_2}{dx^2} = \frac{PL}{2} - \frac{P}{2}x$$

$$EI\,\frac{dy_2}{dx} = -\frac{P}{4}x^2 + \frac{PL}{2}x + C_3$$

$$EI\,y_2 = -\frac{P}{12}x^3 + \frac{PL}{4}x^2 + C_3x + C_4$$

Determining the constants of integration:

Section 1; at A $x = 0, y_1 = 0 \qquad \Rightarrow \qquad C_2 = 0$

Section 2; at B $\qquad x = L, y_2 = 0 \qquad \Rightarrow \qquad 0 = -\frac{PL^3}{12} + \frac{PL^3}{4} + C_3L + C_4$

$$\Rightarrow \quad 0 = \frac{PL^3}{6} + C_3L + C_4$$

At $\qquad x = \frac{L}{2}, y_1 = y_2 \qquad \Rightarrow \qquad \frac{P}{12}x^3 + C_1x + C_2 = -\frac{P}{12}x^3 + \frac{PL}{4}x^2 + C_3x + C_4$

141

$$\Rightarrow \quad \frac{PL^3}{96} + C_1\frac{L}{2} + C_2 = -\frac{PL^3}{96} + \frac{PL^3}{16} + C_3\frac{L}{2} + C_4$$

At $\quad x = \frac{L}{2}, \frac{dy_1}{dx} = \frac{dy_2}{dx} \quad \Rightarrow \quad \frac{P}{4}x^2 + C_1 = -\frac{P}{4}x^2 + \frac{PL}{2}x + C_3$

$$\Rightarrow \quad \frac{PL^2}{16} + C_1 = -\frac{PL^2}{16} + \frac{PL^2}{4} + C_3$$

Solving simultaneously:

$$C_4 = -\frac{PL^3}{6} - C_3L$$

$$C_2 = 0$$

$$C_1 = -\frac{PL^2}{16} - \frac{PL^2}{16} + \frac{PL^2}{4} + C_3 = \frac{PL^2}{8} + C_3$$

$$C_3 = \frac{-PL^2}{12} + C_1 - \frac{2C_4}{L}$$

$$C_3 = \frac{-PL^2}{12} + \frac{PL^2}{8} + C_3 - \frac{2}{L}\left(-\frac{PL^3}{6} - C_3L\right)$$

$$C_3 = \frac{PL^2}{24} - C_3 + \frac{PL}{3} + 2C_3$$

$$\therefore \quad -2C_3 = \frac{3}{8}PL^2$$

$$C_3 = -\frac{3}{16}PL^2$$

$$\Rightarrow C_1 = \frac{PL^2}{8} + C_3 = \frac{PL^2}{8} + \left(-\frac{3}{16}PL^2\right) = -\frac{PL^2}{16}$$

$$\Rightarrow C_4 = -\frac{PL^3}{6} + \frac{3}{16}PL^3 = -\frac{5}{48}PL^3$$

Substituting calculated constants into Equations A-12 and A-13;

$$EI \frac{dy_1}{dx} = \frac{P}{4}x^2 + C_1$$

and $EI \ y_1 = \frac{P}{12}x^3 + C_1 x + C_2$

For $x = \frac{L}{2}$

$$\Rightarrow \frac{dy}{dx} = \left(\frac{PL^2}{16} - \frac{PL^2}{16}\right)\frac{1}{EI} = 0$$

and $\Rightarrow y_1 = \left(\frac{PL^3}{96} - \frac{PL^3}{32}\right)\frac{1}{EI} = -\frac{PL^3}{48}\left(\frac{1}{EI}\right)$

Thus the maximum deflection is at D with $\frac{dy}{dx} = 0$ and the deflection is y_1.

As $y_1 = -\frac{PL^3}{48EI}$

$$\therefore E_{stent} = -\frac{PL^3}{48y_1 I}$$

B ANSYS Element Descriptions

SHELL281

The element used for the mesh of the idealised tubular stent was SHELL281. The description taken from the ANSYS help file is shown below, with an image of the 3D structure of the element (Figure B-1).

SHELL218 Element Description

SHELL218 is suitable for analyzing thin to moderately-thick shell structures. The element has eight nodes with six degrees of freedom at each node: translations in the x, y, and z axes, and rotations about the x, y, and z-axes. (When using the membrane option, the element has translational degrees of freedom only.)

SHELL281 is well-suited for linear, large rotation, and/or large strain nonlinear applications. Change in shell thickness is accounted for in nonlinear analyses. The element accounts for follower (load stiffness) effects of distributed pressures.

SHELL281 may be used for layered applications for modeling composite shells or sandwich construction. The accuracy in modeling composite shells is governed by the first-order shear-deformation theory (usually referred to as Mindlin-Reissner shell theory).

The element formulation is based on logarithmic strain and true stress measures. The element kinematics allow for finite membrane strains (stretching). However, the curvature changes within a time increment are assumed to be small.
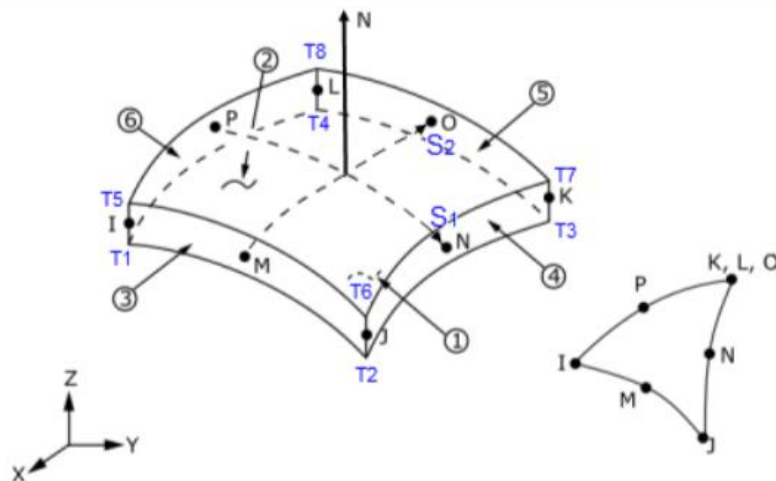
Figure B-1: SHELL281 Geometry

144

SOLID187

The element used for the mesh of the artery in the idealised tubular stent model was SOLID187. The description taken from the ANSYS help file is shown below, with an image of the 3D structure of the element (Figure B-2).

SOLID187 Element Description

SOLID187 element is a high-order 3-D, 10-node element. The element has a quadratic displacement behavior and is well suited to modeling irregular meshes (such as those produced from various CAD/CAM systems).

The element is defined by 10 nodes having three degrees of freedom at each node: translations in the nodal x, y, and z directions. The element has plasticity, hyperelasticity, creep, stress stiffening, large deflection, and large strain capabilities. It also has mixed formulation capability for simulating deformations of nearly incompressible elastoplastic materials, and fully incompressible hyperelastic materials. (ANSYS Inc., 2020)
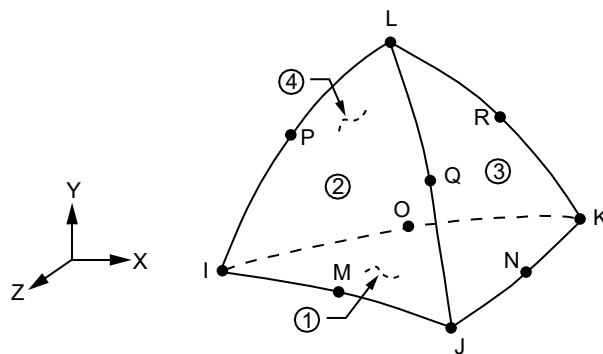
Figure B-2: SOLID187 Geometry

MPC184

The element used to represent the supports in the FEA representation of the 3-point-bend testing was MPC184. The description taken from the ANSYS help file is shown below, with an image of the 3D structure of the element (Figure B-2).

MPC184 Element Description

The MPC184 rigid link/beam element can be used to model a rigid constraint between two deformable bodies or as a rigid component used to transmit forces and moments in engineering applications. This element is well suited for linear, large rotation, and/or large strain nonlinear applications.

The kinematic constraints are imposed using one of the following two methods:

The direct elimination method, wherein the kinematic constraints are imposed by internally generated MPC (multipoint constraint) equations. The degrees of freedom of a dependent node in the MPC equations are eliminated in favor of an independent node.

The Lagrange multiplier method, wherein the kinematic constraints are imposed using Lagrange multipliers. In this case, all the participating degrees of freedom are retained.
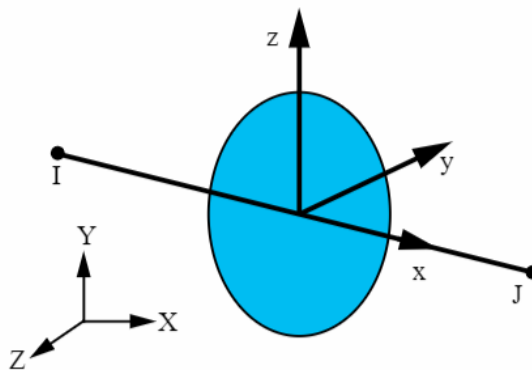
Figure B-3: Rigid Link/Beam Geometry

C DMA Raw Data

The raw data obtained from the 3-point-bend tests for stents 1, 2 and 3 is shown in Table

C-1, Table C-2 and Table C-3 respectively below.

Table C-1: Raw data from Stent 1 3-point-bend test

Time (min)	Temp (degC)	Displacement (µm)	Static force (N)	Position (mm)	Length (mm)	Stress (MPa)	Strain	Stiffness	Relaxation modulus (MPa)	Creep compliance (µm^2/N)	GCA Pressure (kPa gauge)
0.01134167	24.177	2.580261	0.001043392	16.32969	20	0.281463	0.008557	404.3747	3289.275	304.0184	0
0.04416666	24.25133	100.7324	0.002210245	16.42784	20	0.596231	0.334062	21.94176	178.4792	5602.894	0
0.0775	24.15629	286.7461	0.00387682	16.61386	20	1.045802	0.950944	13.52005	109.9751	9092.969	0
0.1108334	24.03152	482.8832	0.005543146	16.81	20	1.495306	1.601399	11.47927	93.37494	10709.51	0
0.1441666	24.02718	665.1365	0.00721042	16.99225	20	1.945065	2.205811	10.84051	88.17914	11340.55	0
0.1775	24.04514	837.9636	0.008876905	17.16508	20	2.394612	2.778962	10.59343	86.16931	11605.06	0
0.2108334	24.04738	1010.646	0.01054348	17.33776	20	2.844182	3.351632	10.43242	84.85962	11784.16	0
0.2441666	23.94887	1168.319	0.01221014	17.49544	20	3.293778	3.87453	10.45104	85.01106	11763.18	0
0.2775	23.97162	1316.454	0.01387682	17.64357	20	3.743378	4.365794	10.54106	85.74334	11662.71	0
0.3108334	24.01329	1458.906	0.01554314	17.78602	20	4.192879	4.838211	10.65397	86.66176	11539.11	0
0.3441666	23.97741	1592.476	0.01720982	17.91959	20	4.64248	5.281171	10.80696	87.90626	11375.76	0
0.3775	23.90089	1731.655	0.01887687	18.05878	20	5.092179	5.742737	10.90106	88.67166	11277.56	0
0.4108333	23.8946	1887.908	0.02054304	18.21503	20	5.54164	6.260922	10.88138	88.51155	11297.96	0
0.4441666	24.0266	2094.95	0.02220982	18.42208	20	5.991268	6.947543	10.6016	86.23578	11596.11	0
0.4775	23.9431	2257.175	0.02387662	18.5843	20	6.440899	7.485534	10.5781	86.04462	11621.88	0
0.5108333	23.92776	2433.52	0.02554331	18.76065	20	6.8905	8.070354	10.49644	85.38042	11712.29	0
0.5441666	23.9344	2642.785	0.02720985	18.96991	20	7.340064	8.764343	10.2959	83.74918	11940.42	0
0.5775	24.06215	2865.488	0.02887685	19.19262	20	7.789749	9.502899	10.07746	81.97234	12199.24	0
0.6108334	24.0345	3068.866	0.03054382	19.39599	20	8.239428	10.17737	9.952805	80.95835	12352.03	0
0.6441666	24.11058	3196.67	0.03221	19.5238	20	8.688891	10.6012	10.07611	81.96136	12200.87	0
0.6775	23.93276	3334.36	0.03387672	19.66149	20	9.1385	11.05783	10.15988	82.64278	12100.27	0
0.7108332	23.9951	3515.403	0.0355437	19.84254	20	9.588181	11.65823	10.11085	82.2439	12158.96	0
0.7441666	24.06261	3729.19	0.03720974	20.05632	20	10.03761	12.36722	9.977968	81.16303	12320.88	0
0.7775	23.95878	3993.262	0.03887722	20.3204	20	10.48742	13.24297	9.735702	79.19238	12627.48	0
0.8108334	23.87255	4338.888	0.04054361	20.66602	20	10.93694	14.38918	9.344239	76.00815	13156.48	0
0.8441666	23.95403	4689.297	0.04220996	21.01644	20	11.38646	15.55125	9.001339	73.2189	13657.67	0
0.8775	23.9337	5004.01	0.04387705	21.33115	20	11.83617	16.59494	8.76838	71.32398	14020.53	0
0.9108334	23.8225	5075.25	0.0455436	21.40239	20	12.28573	16.8312	8.973663	72.99379	13699.8	0

0.9441666	23.78248	5079.112	0.04721028	21.40625	20	12.73533	16.844	9.294986	75.6075	13226.2	0
0.9775001	23.80324	5082.674	0.04887659	21.40981	20	13.18483	16.85582	9.616313	78.22125	12784.25	0
1.010917	23.82838	5086.03	0.05054388	21.41317	20	13.6346	16.86694	9.937788	80.83619	12370.7	0
1.044333	23.81774	5089.515	0.05221074	21.41666	20	14.08424	16.8785	10.25849	83.44488	11983.96	0
1.077666	23.85913	5092.872	0.05387695	21.42002	20	14.53371	16.88964	10.57889	86.05109	11621	0
1.111	23.94805	5096.07	0.0555437	21.42322	20	14.98333	16.90024	10.89932	88.6575	11279.36	0
1.144334	23.9353	5099.267	0.05721044	21.42641	20	15.43295	16.91084	11.21934	91.26066	10957.62	0
1.177666	23.95142	5102.383	0.05887708	21.42953	20	15.88254	16.92118	11.53914	93.86191	10653.95	0
1.211	23.94008	5105.388	0.06054438	21.43254	20	16.33231	16.93114	11.85892	96.46312	10366.66	0

Table C-2: Raw data from Stent 2 3-point-bend test

Time (min)	Temp (degC)	Displacement (µm)	Static force (N)	Position (mm)	Length (mm)	Stress (MPa)	Strain	Stiffness	Relaxation modulus (MPa)	Creep compliance (µm^2/N)	GCA Pressure (kPa gauge)
0.0021	24.31581	-1.151551	0.001001971	15.72514	20	0.265866	-0.00385	870.1056	6914.653	144.6204	0
0.0285	24.29986	35.90954	0.001501637	15.7622	20	0.398448	0.1199	41.81721	332.3176	3009.169	0
0.06183334	24.29538	216.243	0.003126536	15.94254	20	0.829603	0.722022	14.45844	114.9	8703.222	0
0.09516668	24.28298	376.1913	0.004793496	16.10249	20	1.271918	1.25608	12.74218	101.2609	9875.476	0
0.1285	24.3043	546.5151	0.00646017	16.27281	20	1.714158	1.82478	11.82066	93.93774	10645.35	0
0.1618334	24.36348	712.0822	0.008126594	16.43838	20	2.156331	2.377599	11.41244	90.69366	11026.13	0
0.1951666	24.36918	865.7535	0.009793151	16.59205	20	2.598539	2.890698	11.31171	89.89314	11124.32	0
0.2285	24.38433	1002.667	0.01146011	16.72897	20	3.040855	3.347845	11.42962	90.83022	11009.55	0
0.2618334	24.33724	1149.632	0.01312657	16.87594	20	3.483037	3.838552	11.41806	90.73831	11020.7	0
0.2951667	24.2694	1303.372	0.01479356	17.02967	20	3.92536	4.35188	11.35022	90.19916	11086.58	0
0.3285	24.32447	1468.309	0.01646038	17.19461	20	4.367638	4.902594	11.21043	89.08832	11224.82	0
0.3618334	24.35504	1643.316	0.01812682	17.36962	20	4.809814	5.48693	11.03064	87.65949	11407.78	0
0.3951666	24.26674	1812.047	0.01979338	17.53835	20	5.252026	6.050314	10.92322	86.80584	11519.96	0
0.4285	24.32122	1989.261	0.02146022	17.71556	20	5.694308	6.64202	10.78804	85.73158	11664.31	0
0.4618334	24.38432	2170.162	0.02312706	17.89647	20	6.136591	7.246039	10.65684	84.68891	11807.92	0
0.4951667	24.43344	2357.025	0.02479367	18.08333	20	6.578814	7.869963	10.51905	83.59399	11962.58	0
0.5285	24.45334	2529.569	0.02645964	18.25588	20	7.020868	8.446076	10.46014	83.12579	12029.96	0
0.5618334	24.34835	2695.42	0.02812659	18.42173	20	7.46318	8.999844	10.43496	82.92569	12058.99	0
0.5951668	24.40883	2866.465	0.02979356	18.59277	20	7.905499	9.570953	10.39383	82.59887	12106.7	0
0.6285	24.50828	3083.47	0.03145987	18.80978	20	8.34764	10.29552	10.20275	81.08032	12333.45	0
0.6618334	24.57703	3216.372	0.03312639	18.94268	20	8.78984	10.73927	10.29931	81.84766	12217.82	0
0.6951666	24.55942	3334.264	0.03479318	19.06058	20	9.23211	11.1329	10.43504	82.92636	12058.89	0
0.7285	24.49795	3461.862	0.03646066	19.18818	20	9.674562	11.55895	10.53209	83.69762	11947.77	0
0.7618332	24.54466	3606.739	0.03812652	19.33306	20	10.11658	12.04268	10.57091	84.00609	11903.9	0
0.7951668	24.51388	3768.526	0.03979336	19.49484	20	10.55887	12.58288	10.5594	83.91458	11916.88	0
0.8285	24.54303	3932.688	0.04146044	19.659	20	11.00122	13.13101	10.54252	83.78047	11935.96	0
0.86185	24.51768	4114.392	0.04312694	19.84071	20	11.44341	13.7377	10.48197	83.29928	12004.91	0
0.8953334	24.60562	4329.628	0.04479336	20.05594	20	11.88558	14.45636	10.34577	82.21695	12162.94	0

0.9286668	24.60406	4637.702	0.04645976	20.36402	20	12.32775	15.485	10.01784	79.61089	12561.1	0
0.962	24.50332	5154.481	0.04812709	20.8808	20	12.77016	17.2105	9.336944	74.19986	13477.12	0
0.9953332	24.41014	5735.298	0.0497937	21.46162	20	13.21238	19.14981	8.681975	68.99488	14493.83	0
1.028667	24.3939	5791.093	0.0514606	21.51742	20	13.65468	19.33611	8.886163	70.61755	14160.79	0
1.062	24.42574	5795.959	0.05312702	21.52228	20	14.09686	19.35235	9.166219	72.84314	13728.13	0
1.095333	24.42882	5800.371	0.05479407	21.5267	20	14.5392	19.36708	9.446649	75.07169	13320.6	0
1.128667	24.3703	5804.424	0.0564607	21.53075	20	14.98142	19.38062	9.727187	77.30109	12936.43	0
1.162	24.33486	5808.416	0.05812731	21.53474	20	15.42365	19.39394	10.00743	79.52816	12574.16	0
1.195334	24.26563	5812.446	0.0597939	21.53877	20	15.86586	19.4074	10.28722	81.75162	12232.17	0
1.228667	24.20679	5816.394	0.06146051	21.54272	20	16.30809	19.42058	10.56677	83.97321	11908.56	0

Table C-1

Table C-3: Raw data from Stent 3 3-point-bend test

Time (min)	Temp (degC)	Displacement (µm)	Static force (N)	Position (mm)	Length (mm)	Stress (MPa)	Strain	Stiffness	Relaxation modulus (MPa)	Creep compliance (µm^2/N)	GCA Pressure (kPa gauge)
0	24.33061	-1.345594	0.001001977	16.09227	20	0.263696	-0.00451	744.6356	5849.489	170.9551	0
0.01551667	24.3843	3.221508	0.001151555	16.09684	20	0.303061	0.010793	357.4584	2808.016	356.1233	0
0.04883333	24.431	122.8178	0.002543683	16.21644	20	0.669435	0.411465	20.71103	162.6956	6146.449	0
0.08216666	24.44098	312.0275	0.004210071	16.40565	20	1.107988	1.045356	13.49263	105.9914	9434.725	0
0.1155	24.37134	509.7473	0.005877146	16.60337	20	1.546721	1.707758	11.52953	90.57028	11041.15	0
0.1488333	24.30242	672.997	0.007543303	16.76662	20	1.985212	2.254678	11.20852	88.04861	11357.36	0
0.1821667	24.29004	801.5018	0.009210535	16.89512	20	2.423987	2.685195	11.4916	90.27231	11077.6	0
0.2155	24.31947	935.4106	0.01087671	17.02904	20	2.862485	3.133817	11.62774	91.34181	10947.89	0
0.2488333	24.28616	1070.596	0.01254342	17.16422	20	3.301121	3.586718	11.71629	92.03738	10865.15	0
0.2821667	24.2257	1208.939	0.01421038	17.30256	20	3.739825	4.050192	11.75443	92.33697	10829.9	0
0.3155	24.19308	1344.558	0.01587642	17.43819	20	4.178284	4.504546	11.80791	92.75708	10780.85	0
0.3488333	24.22575	1478.062	0.01754338	17.57169	20	4.616989	4.95181	11.86918	93.23841	10725.19	0
0.3821666	24.20805	1622.578	0.0192101	17.7162	20	5.055626	5.435968	11.83924	93.00324	10752.31	0
0.4155	24.15387	1777.089	0.02087687	17.87072	20	5.494281	5.953613	11.74779	92.28482	10836.02	0
0.4488334	24.17758	1948.886	0.02254342	18.04252	20	5.932876	6.529166	11.56734	90.8673	11005.06	0
0.4821667	24.14485	2138.568	0.02421016	18.2322	20	6.37152	7.164641	11.32073	88.93008	11244.79	0
0.5155	24.173	2349.355	0.02587686	18.44299	20	6.810156	7.87082	11.01445	86.52408	11557.48	0
0.5488332	24.19149	2572.586	0.02754326	18.66622	20	7.248713	8.618689	10.70645	84.10459	11889.96	0
0.5821668	24.26345	2820.581	0.02921011	18.91422	20	7.687384	9.449524	10.35606	81.3521	12292.25	0
0.6155	24.19284	3086.817	0.03087682	19.18045	20	8.126024	10.34147	10.0028	78.57708	12726.36	0
0.6488332	24.17758	3278.814	0.03254311	19.37245	20	8.56455	10.9847	9.925269	77.968	12825.78	0
0.6821668	24.19902	3455.013	0.03420996	19.54865	20	9.003226	11.575	9.901547	77.78165	12856.5	0
0.7155	24.18113	3588.644	0.03587705	19.68228	20	9.441961	12.02269	9.997384	78.5345	12733.26	0
0.7488334	24.20302	3700.915	0.03754356	19.79456	20	9.880548	12.39882	10.1444	79.6894	12548.72	0
0.7821668	24.16511	3824.232	0.0392104	19.91787	20	10.31922	12.81196	10.25314	80.54363	12415.63	0
0.8155	24.15787	3988.56	0.04087719	20.0822	20	10.75788	13.36249	10.24861	80.508	12421.13	0
0.8488332	24.17549	4120.558	0.04254352	20.2142	20	11.19641	13.80472	10.3247	81.10572	12329.59	0
0.882225	24.1739	4337.532	0.04421012	20.43118	20	11.63502	14.53162	10.19246	80.06692	12489.55	0

0.9156666	24.21228	4663.078	0.04587667	20.75672	20	12.07362	15.62226	9.838282	77.28468	12939.18	0
0.9489999	24.23902	5010.59	0.0475442	21.10424	20	12.51247	16.78651	9.488741	74.53886	13415.82	0
0.9823334	24.3254	5260.655	0.0492105	21.3543	20	12.951	17.62427	9.354442	73.48388	13608.43	0
1.015667	24.27652	5266.28	0.05087715	21.35992	20	13.38962	17.64312	9.660926	75.89145	13176.72	0
1.049	24.24165	5270.898	0.05254355	21.36455	20	13.82818	17.65859	9.968614	78.3085	12770.01	0
1.082334	24.33523	5275.232	0.05421055	21.36888	20	14.26689	17.67311	10.27643	80.72652	12387.5	0
1.115666	24.35038	5279.31	0.05587735	21.37296	20	14.70555	17.68677	10.58422	83.14436	12027.27	0
1.149	24.21041	5283.19	0.0575436	21.37684	20	15.14406	17.69977	10.89183	85.5608	11687.6	0
1.182334	24.131	5287.06	0.05921066	21.38071	20	15.5828	17.71274	11.19917	87.97512	11366.85	0